FLORIDA INTERNATIONAL UNIVERSITY

Miami, Florida

# FULL-SCALE EXPERIMENTATION MODELING TO STUDY WIND-INDUCED VIBRATIONS, WIND DRIVEN RAIN AND THEIR EFFECTS ON CURTAINWALL WINDOW SYSTEMS

A dissertation submitted in partial fulfillment of

the requirements for the degree of

DOCTOR OF PHILOSOPHY

in

CIVIL ENGINEERING

by

Krishna Sai Vutukuru

2021

To: Dean John L. Volakis
College of Engineering and Computing

This dissertation, written by Krishna Sai Vutukuru and entitled, Full-Scale Experimental Modeling to Study Wind-Induced Vibrations, Wind Driven Rain, and Their Effects on Curtainwall Window Systems, has been approved regarding style and intellectual content, is referred to you for judgment.

We have read this dissertation and recommend that it be approved.

Peter Irwin

Ioannis Zisis

Seung Jae Lee

Nipesh Pradhananga

Arindam Gan Chowdhury, Major Professor

Date of Defense: November 5, 2021

The dissertation of Krishna Sai Vutukuru is approved.

Dean John L. Volakis
College of Engineering and Computing

Andr'es G. Gil
Vice President for Research and Economic Development
and Dean of the University Graduate School

Florida International University, 2021

DEDICATION

To my parents, Jaya and Hari for their support.

# ACKNOWLEDGMENTS

It is a genuine pleasure to express my deep sense of gratitude to my major professor, Dr. Arindam Gan Chowdhury. His unreserved sharing of wind engineering knowledge and availability for meetings greatly helped the accomplishment of this herculean task. Apart from wind engineering, I learned a great deal about professionalism, work ethic, and teamwork from him. I would like to thank my committee members, Dr. Peter Irwin, Dr. Ioannis Zisis, Dr. Seung Jae Lee, and Dr. Nipesh Pradhananga for their constant support and motivation. Their timely advice, meticulous scrutiny, scholarly advice, and scientific approach have helped me to a great extent. In addition, I would like to express my sincere gratitude to industry partner on the project, Permasteelisa group, especially to Dr. Guido Lori for his extraordinary scholarly advice and knowledge sharing about the façade industry. My special thanks also go to Dr. Emil Simiu for his review and constructive comments on this dissertation.

It is a great privilege to work in the esteemed Wall of Wind facility during my graduate studies. I would like to express my thanks to Dr. Amal Elawady for her guidance during my graduate studies on various other projects which helped enhance my wind engineering knowledge. I would also like to thank Mr. Erik Salna and meteorologists at the National Hurricane Center for suggestions about rain rates and field measurements during hurricanes. Thanks, are also due to all the laboratory staff, Walter Conklin, James Erwin, Roy-Liu Marques, Manuel Matus, Dejiang Chen, and Steven Diaz for their help in accomplishing this project on time. I would also like to thank my fellow doctoral students at WOW for their help and support. Finally, I would like to acknowledge the financial

support provided by Florida Sea Grant College Program and Florida Department of Emergency Management through funding. The financial aid provided by FIU University Graduate School through Dissertation Year Fellowship is also greatly appreciated.

ABSTRACT OF THE DISSERTATION

FULL-SCALE EXPERIMENTAL MODELING TO STUDY WIND-INDUCED VIBRATIONS, WIND DRIVEN RAIN, AND THEIR EFFECTS ON CURTAINWALL WINDOW SYSTEMS

by

Krishna Sai Vutukuru

Florida International University, 2021

Miami, Florida

Professor Arindam Gan Chowdhury, Major Professor

Lewis Fry Richardson famously summarized turbulence as big whirls have little whirls, that feed on their velocity and little whirls have lesser whirls, and so on to viscosity. Big whirls/eddies typically affect the whole building structure whereas small eddies cause local area pressures causing damage to building components. Oncoming wind may carry high energy content due to these small eddies in the high-frequency range and sometimes these frequencies fall in the range of natural frequency of building components. These small eddies may cause response amplification due to this resonance, which is currently not considered in design codes such as ASCE 7-16. This dissertation, through full-scale experimental testing, addressed the possible resonance due to the matching of frequencies of an operable window with oncoming wind.

Curtainwalls have become a part of modern infrastructure specially to preserve architectural freedom. Operable windows are usually attached to these glazing units for

ventilation. However, in high-rise buildings and/or extreme wind events these window frames are susceptible to vibrations. To evaluate wind-induced stresses, code guidelines focus on simplified uniform pressure-based static/cyclic load test procedures. These do not address the realistic dynamic wind loading which failed several engineered curtain-wall window systems due to vibrations, such as the 2020 Hurricane Laura damage to the Capital One building in Louisiana. To address this knowledge deficit and provide the curtain wall industry with realistic dynamic test data, full-scale curtain wall units with operable windows are tested in the Wall of Wind Facility.

These local vibration failures also lead to water intrusion into buildings causing interior content damage. To quantify and detect the vulnerable window system components a full-scale Rain Size Distribution (RSD) is developed at the Wall of Wind facility with the help of 3-D printed nozzles. The window sample is exposed to horizontal wind-driven rain and the results are quantified as rain rate entering through the window area. These results helped to understand the risks inherent in current window design by exposing weak locations under extreme wind loading and showed the inadequacy of code guidelines for wind-driven rain testing. The current study provided Dynamic Amplification Factor values that can be incorporated into the current quasi-static design approach to include dynamic effects. Two approaches were introduced based on the Gust Effect Factor to incorporate dynamic effects into existing design guidelines. Possible code changes to ASCE 7 were suggested to achieve a resilient design of dynamically sensitive components.

TABLE OF CONTENTS

CHAPTER PAGE

1. INTRODUCTION ..... 1
1.1 Building vulnerabilities under wind loads ..... 1
1.2 Risk models – a brief review ..... 2
1.3 Flow fluctuation effects and wind-driven rain ..... 6
1.4 Research hypothesis, significance and objectives ..... 7
1.5 Dissertation organization ..... 10
1.6 Chapter 1 references ..... 11

2. EXPERIMENTAL SETUP AND INSTRUMENTATION ..... 15
2.1 Wall of Wind experimental facility ..... 15
2.2 Modelling, Construction, Mechanical Properties, and Product Approvals ..... 16
2.3 Instrumentation and testing protocol ..... 26
2.4 Chapter 2 references ..... 35

3. HOLISTIC FULL-SCALE TESTING TO DETERMINE WINDOW SYSTEM VULNERABILITY TO WIND FLUCTUATIONS ..... 37
3.1 Wind Speed and Pressure results ..... 37
3.2 Window glass vibration ..... 47
3.3 Analytical model and window resistance ..... 57
3.4 Destructive Testing and hardware vulnerability ..... 63
3.5 Towards codification and Design suggestions ..... 68
3.6 Chapter 3 references ..... 72

4. SIMULATION OF FULL-SCALE RAINDROP SIZE DISTRIBUTION AND TESTS TO QUANTIFY WATER INTRUSION INTO THE OPERABLE WINDOW ..... 74
4.1 Rain intrusion into the built environment ..... 74
4.2 Literature Review and Target RSD parameters ..... 76
4.3 Full-Scale RSD distribution at WOW ..... 87
4.4 Operable window WDR tests ..... 96
4.5 Chapter 4 references ..... 102

5. CONCLUSIONS AND FUTURE WORK ..... 108
5.1 Conclusions ..... 108

5.2 Recommendations for future study .....110

VITA .....112

LIST OF TABLES

TABLE PAGE

Table 1: Curtainwall window codes and standards..... 23

Table 2: Testing protocol..... 33

Table 3: Acceleration DAF values for window glass..... 56

Table 4: Full-scale WDR testing protocol..... 88

Table 5: Tee Jet agricultural nozzle configuration..... 88

Table 6: Flow rates for the best of tested configurations..... 90

LIST OF FIGURES

FIGURE PAGE

Figure 1.1: Damage Caused to Windows of Lake Charles Tower due to Hurricane Laura (ENR #50130)..... 2

Figure 1.2: FEMA-HAZUS model (FEMA manual 2.1)..... 4

Figure 1.3: FPHLM methodology (FPHLM, 2015)..... 5

Figure 1.4: Flow around an airplane wing vs flow around a building (Holmes, 2001)..... 6

Figure 1.5: Research Hypothesis for vibration effects..... 8

Figure 1.6: Research hypothesis for wind driven rain Effects..... 8

Figure 2.1: Inside flow management box showing roughness elements and spires ..... 15

Figure 2.2: Extender type hinge..... 16

Figure 2.3: Traditional type hinge ..... 16

Figure 2.4: Plan of unitized curtainwall..... 18

Figure 2.5: Elevation of unitized curtainwall ..... 18

Figure 2.6: Section along Joint J3..... 19

Figure 2.7: Glazing compositions..... 19

Figure 2.8: Framing profile cross-sections ..... 20

Figure 2.9: Frame mechanical properties..... 20

Figure 2.10: Curtainwall specimen on Turntable ..... 21

Figure 2.11: External pressure tap layout ..... 27

Figure 2.12: Internal pressure tap layout ..... 28

Figure 2.13: Strain gauges on the Window frame, Phase I..... 28

Figure 2.14: Strain gauges and accelerometers on Window glass, Phase II..... 29

Figure 2.15*:* Strain gauges on the Window frame, Phase II ..... 29

Figure 2.16: Strain gauges and accelerometers on Window glass, Phase II ..... 30
Figure 2.17: Strain gauges on connection hardware, Phase II ..... 31
Figure 2.18: Accelerometers on connection hardware, Phase II ..... 32
Figure 2.19: Rain collection system with a tap-drain mechanism ..... 32
Figure 2.20: Test protocol wind directions ..... 34
Figure 3.1: Wind gust spectrum ..... 38
Figure 3.2: Wind Velocity and turbulence intensity profile comparison with ESDU ..... 38
Figure 3.3: Phase I, $Cp_{,mean}$ for first quadrant wind directions ..... 40
Figure 3.4: Phase I, $Cp_{,mean}$ for second and third quadrant wind directions ..... 40
Figure 3.5: Phase I, $Cp_{,mean}$ for fourth quadrant wind directions ..... 41
Figure 3.6: Phase I, $Cp_{,peak}$ for first quadrant wind directions ..... 42
Figure 3.7: Phase I, $Cp_{,peak}$ for second and third quadrant wind directions ..... 42
Figure 3.8: Phase I, $Cp_{,peak}$ for fourth quadrant wind directions ..... 43
Figure 3.9: Phase II, $Cp_{,mean}$ for first quadrant wind directions ..... 44
Figure 3.10: Phase II, $Cp_{,mean}$ for second and third quadrants ..... 44
Figure 3.11: Phase II, $Cp_{,mean}$ for fourth quadrant wind directions ..... 45
Figure 3.12: Phase II, $Cp_{,peak}$ for first quadrant wind directions ..... 45
Figure 3.13: Phase II, $Cp_{,peak}$ for second and third quadrant wind directions ..... 46
Figure 3.14: Phase II, $Cp_{,peak}$ for fourth quadrant wind directions ..... 46
Figure 3.15: Identification of positive peaks for damping estimation ..... 49
Figure 3.16: Frequency Response Function to obtain natural frequency ..... 49
Figure 3.17: Displacement time-history ..... 50
Figure 3.18: Exponential fit of positive peaks ..... 51
Figure 3.19: Acceleration time-history comparison between corner and center of the glass ..... 53

Figure 3.20: Effect of wind direction on RMS ..... 53

Figure 3.21: Stabilization diagram to obtain stable and unstable frequencies..... 54

Figure 3.22: Power Spectral Density plots using pwelch ..... 54

Figure 3.23: Typical background (wind spectrum) and resonant response (due to resonance) ..... 55

Figure 3.24: Full structure FEM and first mode ..... 55

Figure 3.25: Experimental Non-dimensional (only frequency) PSD showing the effect of wind speed ..... 58

Figure 3.26: Time and frequency domain of typical data (Holmes, 2015)..... 59

Figure 3.27: Transfer function to account for missing low frequency in response spectrum..... 60

Figure 3.28: MAF showing resonance component for first two modes, 13.3 Hz and 16.1 Hz..... 60

Figure 3.29: Analytical model with compensated low frequency and predicted dynamic response match at 44.7 m/s ..... 61

Figure 3.30: Yielded connection hinge..... 64

Figure 3.31: Accelerometers on the hardware showing cyclic accelerations ..... 64

Figure 3.32: PSD of accelerations on the hinges ..... 65

Figure 3.33: Strain on the failed hinge..... 65

Figure 3.34: Typical pdf example of damage function..... 66

Figure 3.35: Methodology to calculate vulnerability curve encompassing various wind speeds..... 66

Figure 3.36: Hardware failure probability curve ..... 67

Figure 3.37: Comparison of Gust Effect Factors from various approaches ..... 70

Figure 3.38: Flow chart showing two suggested design approaches for industry ..... 71

Figure 4.1:Attribute classification for rain intrusion into the building..... 75

Figure 4.2: Full-scale RSD calculations (Baheru, 2014) ..... 79

Figure 4.3: Statistical Maximum 10-min rainfall intensity for 500 yr. MRI ..... 80

Figure 4.4: Gamma models comparison for different rain rates ..... 81

Figure 4.5: PIP at 0.91m. (6ft.) height located at turntable center ..... 88

Figure 4.6: Flow free measurements of UC nozzle ..... 89

Figure 4.7: Figures showing nozzle dimensions and actual 3-D printed nozzle ..... 90

Figure 4.8 (a): Nozzle configuration to achieve Rain rate of 56.6 cm/hr ..... 91

Figure 4.8 (b): Nozzle configuration to achieve Rain rate of 44.4 cm/hr ..... 90

Figure 4.8 (c): Nozzle configuration to achieve Rain rate of 38.1 cm/hr ..... 90

Figure 4.8 (d): Nozzle configuration to achieve Rain rate of 22.4 cm/hr ..... 91

Figure 4.8 (e): Nozzle configuration to achieve Rain rate of 23.6 cm/hr ..... 91

Figure 4.9 (a): RSD comparison at 1.83 m. (6ft.) height, test #1 ..... 92

Figure 4.9 (b): RSD comparison at 1.83 m. (6ft.) height, test #5 ..... 92

Figure 4.9 (c): RSD comparison at 1.83 m. (6ft.) height, test #6 ..... 93

Figure 4.9 (d): RSD comparison at 1.83 m. (6ft.) height, test #7 ..... 93

Figure 4.9 (e): RSD comparison at 1.83 m. (6ft.) height, test #8 ..... 94

Figure 4.10: Installed plexiglass water collection system ..... 100

Figure 4.11: Effective Area for Surface Run-off and Direct Impingement ..... 100

Figure 4.12: Total rain intrusion expressed as rain rate ..... 101

Figure 4.13: Formation of water bubble and deposition of water on the windowsill at 100mph ..... 103

# 1. INTRODUCTION

## 1.1 Building vulnerabilities under wind loads

As noted by Baker (2007), there is a continued need for wind engineering input into the design of new infrastructure and buildings. The design of tall buildings for wind has improved significantly in the last few decades, especially for the Main Wind Force Resistance System (MWFRS). This is reflected, for example, in changes of relevant ASCE 7-16 Standard provisions. However, components and cladding (C&C) remain vulnerable (Strobel and Banks (2014), Habte et al. (2015), Cain et al. (2015), Azzi et al. (2020), Vutukuru et al. (2021)). Small turbulence eddies strongly contribute to C&C damage. They occur due to shear in the Atmospheric Boundary Layer (ABL) flow, turbulence in the flow around the building, and turbulence generated by the flow around neighboring buildings. The fact that the high frequencies of the small eddies may coincide with the natural frequencies of C&Cs can be a contributing factor to the latter's vulnerability.

According to the National Academy of Science (1999), more than 50% of the US population lives within 80 km of coastline, and based on the US census (2012) in Florida the coastline population has increased by 270 % between 1960 to 2010. Several hurricane reconnaissance reports such as FEMA (1992), FEMA (2006), Kijewski-Correa et al. (2021) showed that the main damage to buildings was to the envelope (see. e.g., Figure 1.1). It has also been noted that such failures are progressive; for example, the failure of one component can lead to the failure of a neighboring component, or in some cases, by increasing internal pressures, the failure of the whole building. C&C failures typically

cause interior content damage. In addition, component failures pose threat to surrounding buildings due to flying debris.

Figure 1.1: Damage Caused to Windows of Lake Charles Tower due to Hurricane Laura (ENR #50130)

Davenport developed the first Boundary Layer Wind Tunnel in which the flow around buildings and other structures was modeled to reproduce the turbulent Atmospheric Boundary Layer flow. Among the first buildings tested in that wind tunnel were the twin towers of the World Trade Center in New York City.

**1.2 Risk models – a brief review**

Before the catastrophic occurrence of Hurricane Andrew in 1992 risk models were largely based on regression analyses used to calculate hurricane-induced losses (Pan (2014)). More elaborate models were subsequently developed that accounted explicitly for the physical parameters characterizing hurricane features, for building structural

properties, and for actuarial principles and methods (American Academy of Actuaries (2008), Insurance Information Institute (2020). Hurricane physical features include translation speed and direction, central pressure deficit, hurricane track, the radius of maximum wind speeds, and the dependence of rotational speeds on the radius, characterized for a particular type of model by the Holland B parameter. Building structural properties and the type of failure being considered are used to calculate the damage percentage (typically in the form of a damage matrix) to develop fragility and vulnerability curves. The damage matrix is converted into actual dollar loss values based on actuarial principles. Risk modeling is a multi-disciplinary field and includes meteorological input, structural engineering input informed by vulnerability considerations, and probabilistic and statistical input. Currently, public risk models include the Florida Public Hurricane Loss Model(FPHLM) (Chen et al. (2009)) and the Federal Emergency Management Agency-Hazard U.S. (FEMA-HAZUS) (HAZUS hurricane manual (2021)). These risk models categorize building components into super elements and C&C elements (Cope (2004)).

FEMA-HAZUS uses the simplifying assumption that all buildings as rectangular bluff bodies. and classifies them based on the material used, number of stories, and importance. This classification led to 39 different building types. The damage criteria include six C&C failure types (to windows, doors, wall cladding, roof cladding, roof cover, and glazing), two super element failures (wall failures and roof to wall connection failures). For the structural system, foundation sliding, overturning, and uplift failures are considered. Wind loads are estimated by taking into account directional effects based on various wind tunnel

studies (e.g., Surry and Stathopoulos (1978), Meecham (1988), Lin and Surry (1997)). The information available in the National Building Code of Canada (1995), and the ASCE 7 Standard is also used. Failure predictions are performed using fifteen-minute intervals over the entire storm duration and structural engineering principles. Figure 1.2 summarizes the procedure of FEMA-HAZUS.

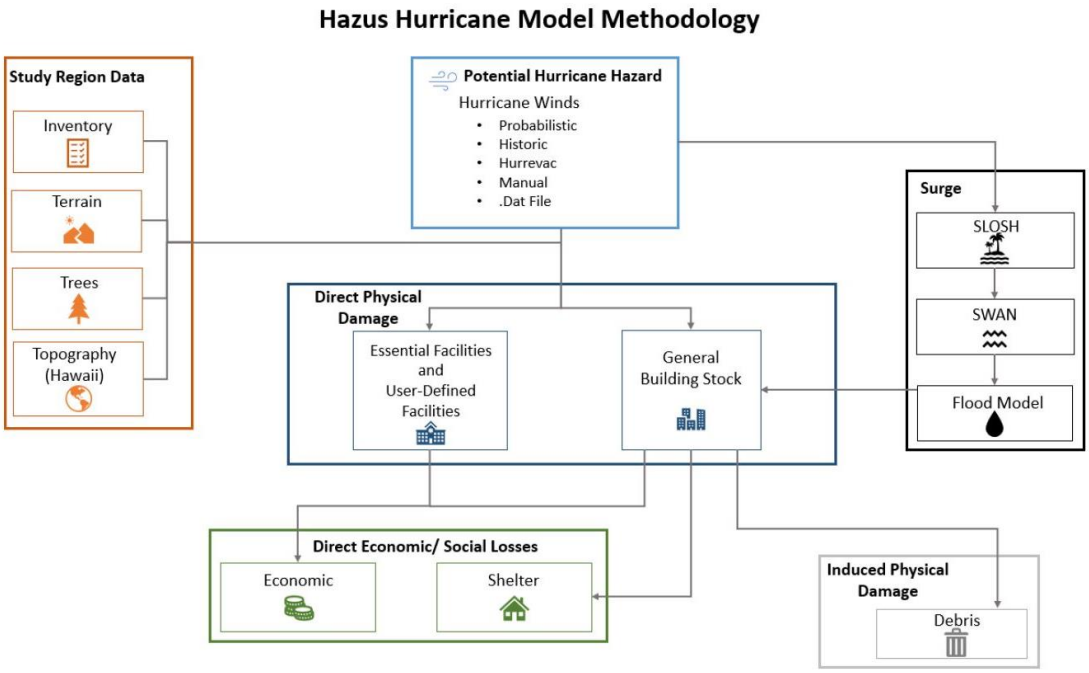


Figure 1.2: FEMA-HAZUS model (FEMA manual 2.1)

FPHLM, primarily developed for the State of Florida, estimates exterior damage by using engineering principles and a probabilistic approach, while interior damage is estimated by an analytical model based on engineering judgment (Pinelli et al. (2008), Pita et al. (2013)). Four common building types are identified based on construction material and roof shape and the vulnerability component of FPHLM targets six C&C and four super element failures (Cope (2004). FPHLM utilizes modified ASCE 7-98 guidelines to calculate wind pressure and Monte-Carlo simulation using a loop of 1000 simulations are

utilized to calculate vulnerability of building components. Figure 1.3 summarizes the methodology of FPHLM.

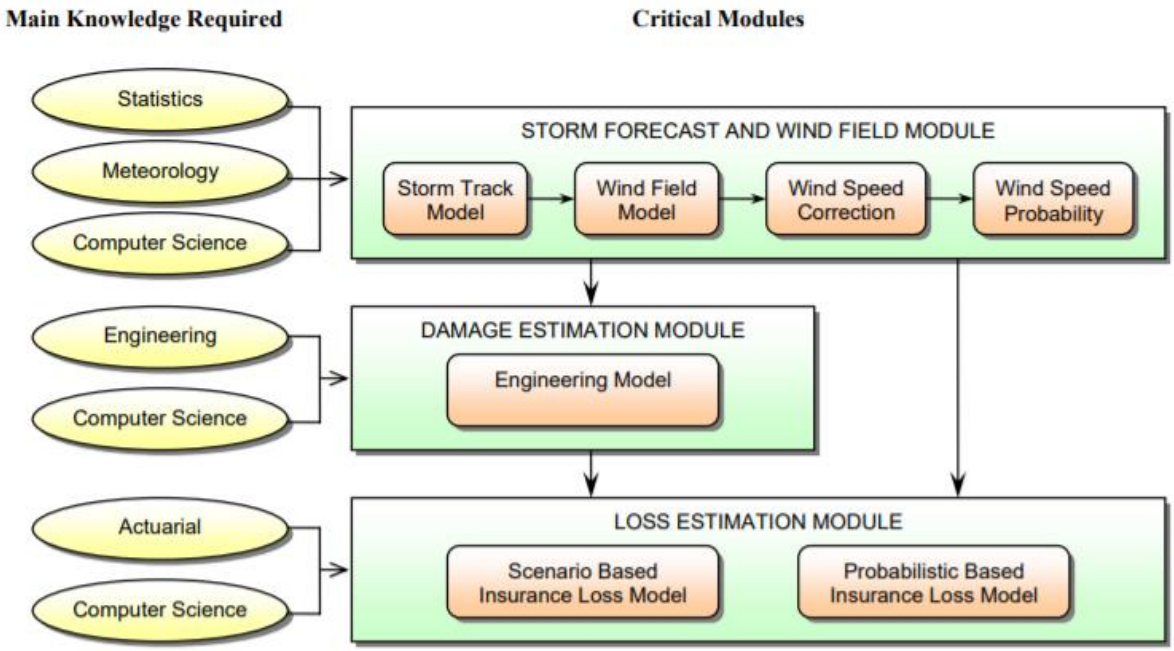


Figure 1.3: FPHLM methodology (FPHLM, 2015)

Proprietary models were developed by various firms, including AIR, ARA, CoreLogic, EQECAT, Impact Forecasting, KCC, and RMS. Generally, these models group buildings with similar performance, and the respective damage functions are developed. For example, AIR considers storm duration as an important parameter (AIR, 2012) used in fatigue analyses. As noted in Section 1.1, due to the progressive nature of wind failures, some localized failures (for example a broken window) can lead to global failures (e.g., due to internal pressurization leading to roof failure).

### 1.3 Flow fluctuation effects and wind-driven rain

According to NOAA (2021) report, extreme wind events caused an estimated 1.875 trillion dollars in damages between 1980 and 2020; and in 2017 alone, the losses exceeded 306 billion dollars. Hurricane Harvey alone was estimated to cost $125 billion. Figure 1.4 describes the basic difference between flow around a bluff body and a streamlined body. Flows around bluff bodies undergo separation, with possible reattachment. Civil structures are mainly bluff bodies with sharp edges (such as buildings, bridges, etc.).

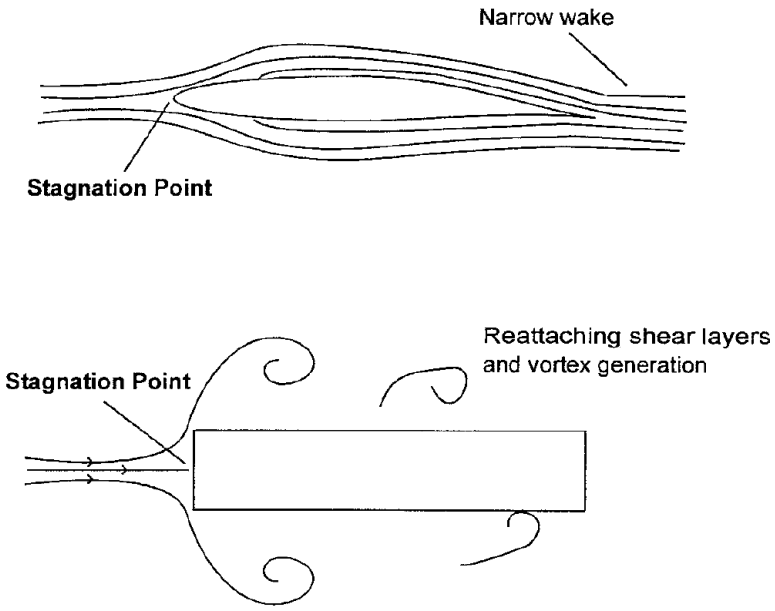


Figure 1.4: Flow around an airplane wing vs flow around a building (Holmes, 2001)

Flow fluctuations in the oncoming wind and the wake of the body produce fluctuating wind loads, which cause flexible buildings, defined by the ASCE 7 Standard to have natural frequencies lower than 1 Hz, to respond dynamically, i.e., to exhibit resonant responses. However, significant damage can occur to, e.g., roofing, windows, and curtain wall systems owing fully or in part to flow fluctuations with frequencies higher

than 1 Hz (FEMA (1992), FEMA (2006), Kijewski-Correa et al. (2021), Strobel and Banks (2014), Habte et al. (2015), Cain et al. (2015), Azzi et al. (2020), Vutukuru et al. (2021)).

Tropical storms and hurricanes are typically associated with heavy rainfall. Hence the need to improve building performance under wind-driven rain (WDR). Surveys by, e.g., FEMA (1992), Pinelli et al. (2018), T. Kijewski-Correa et al., (2021) showed that water intrusion is the main cause of damage to interior contents, and can also cause serviceability disruption and possible mold and mildew growth. This can be the case even for structurally sound buildings. Despite improvements to building codes and standards such as the Florida Building Code Testing and Standards (TAS 202), water intrusion remains a problem as shown in the literature (Choi (1999a), Straube and Burnett (2000), Blocken and Carmeliet (2004a), Salzano et al. (2010a), Kubilay et al. (2014a), and Vutukuru et al., (2020)).

### 1.4 Research hypothesis, significance and objectives

The roof and window systems clearly remain vulnerable components during extreme wind events such as hurricanes. Although there have been extensive studies, based on field and wind tunnel measurements, on the performance and mitigation of various roof systems (e.g. Hazelwood (1981), Bienkiewicz and Sun (1997), Kawair and Nishimura (2003), Li et al. (2014)), the main focus of wind resistance of window systems had been primarily on debris impact. The current dissertation is a part of the project to address this knowledge gap by the study of wind-induced vibrations and wind-driven rain vulnerability of curtainwall window systems through full-scale experimental testing. The

results from these would be utilized to develop a dynamic structural analysis Finite Element Model by another research team.

The hypothesis for this research can be summarized as shown in Figure 1.5 and Figure 1.6.

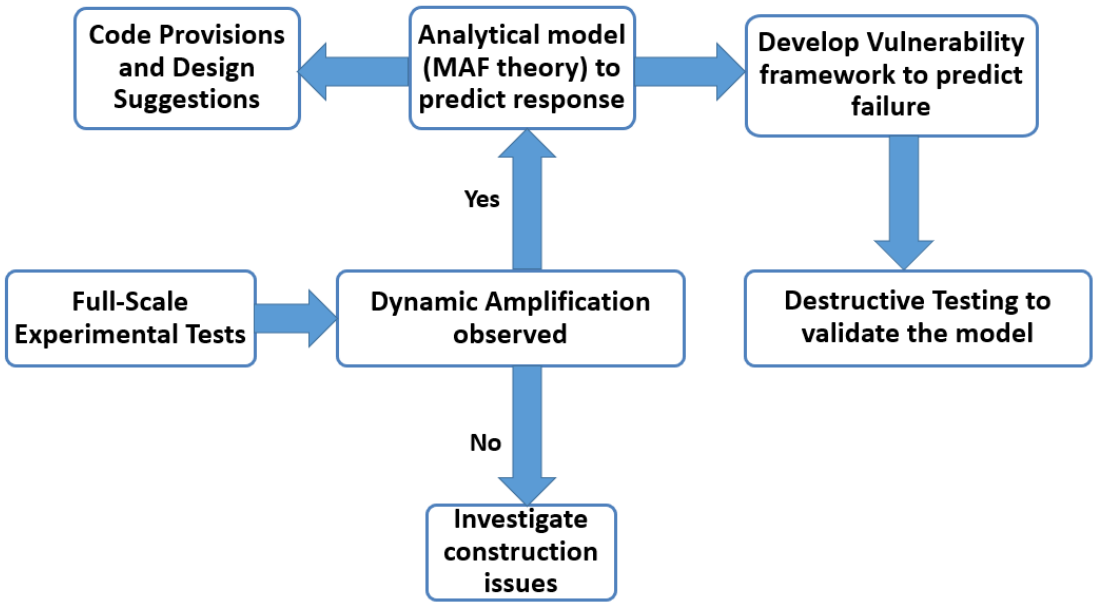


Figure 1.5: Research Hypothesis for vibration effects

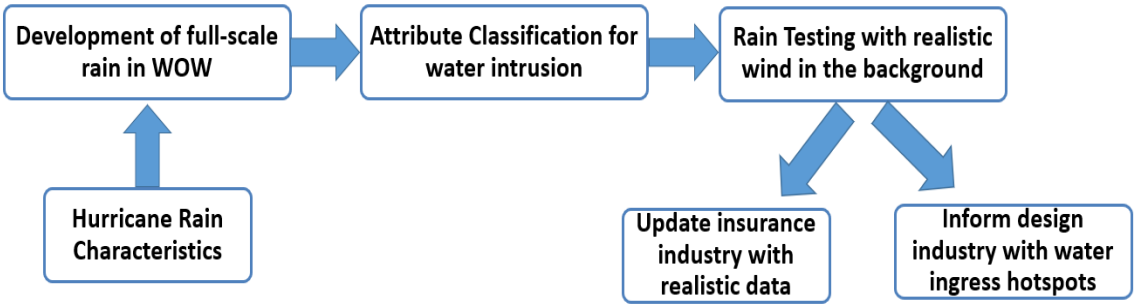


Figure 1.6: Research hypothesis for wind driven rain effects

The primary goal of this dissertation is to fill the knowledge gap about wind-induced resonant vibrations and to develop criteria for incorporating these dynamic effects into the design of operable windows and the secondary goal of this dissertation is to understand the wind-driven rain proneness of the built environment.

To accomplish these goals, the research methods followed for this dissertation were:

- Full-scale testing of operable window systems in open and closed conditions (to comprehend hardware components vibration and glass vibration respectively) subjected to high-frequency eddies to test the hypothesis that ASCE 7-16's, 1 Hz. (structures with natural frequency less than 1Hz. are dynamically sensitive) criterion is not appropriate for components and cladding design.
- To simulate an adequate rain size distribution (based on data from previous hurricanes) to test the window under "realistic" wind and rain conditions experienced during hurricanes.
- To study the resilience of operable windows under realistic wind-driven rain effects and identify the potential hotspots for rain intrusion and compare the results to TAS (Testing and Standards) protocols to understand the adequacy of these standards.

## 1.5 Dissertation organization

This dissertation is organized into five chapters.

An introduction to the Wall of Wind facility and a brief discussion about existing product approvals for window testing is provided in Chapter 2. It also deals with the construction of a full-scale model with the window specimen attached to the curtainwall. Several cases tested to study the window susceptibility were listed and the layout of sensors installed on the model was shown.

Chapter 3 describes aerodynamic and vibration results obtained from the experimental testing. The data analysis includes the estimation of structural damping of the window system from free vibration tests; dynamic amplification of glass using accelerometer results; development of a validated analytical model by considering the background and resonant response components using Mechanical Admittance Function. A brief discussion about destructive testing to identify the hardware vulnerability in open window condition was also included.

Chapter 4 starts with the description of the inadequacy of test protocols for rain testing concerning realistic wind experienced during extreme winds, followed by a literature review showing different types of experimental, numerical, and empirical methodologies adapted for structural testing. Typical full-scale rain parameters observed in hurricanes and existing Rain Size Distribution, RSD (concentration of a particular diameter of a raindrop) models were reviewed. Simulation efforts to obtain full-scale RSD

for varying rain rates were discussed, followed by the results obtained for the operable window systems subjected to simulated wind-driven rain.

The closing chapter summarizes key conclusions based on the experimental testing and provides a brief outlook for future studies.

## 1.6 Chapter 1 references


AAA, 2008. Current Issues in Insurance rate making for catastrophic events, American Academy of Actuaries, December 2008.

AIR, 2021. AIR hurricane model for the US v1.0.0 as implemented in the Touchstone 2020, submitted to Florida Commission on Hurricane Loss Projection Methodology.

ASCE 7-16, American Society of Civil Engineers, 2016. Minimum design loads and associated criteria for buildings and other structures. American Society of Civil Engineers.

ASCE 7-98, American Society of Civil Engineers, 1998. Minimum design loads and associated criteria for buildings and other structures. American Society of Civil Engineers.

ASCE/SEI 49, American Society of Civil Engineers, 2012. Wind Tunnel Testing for Buildings and other Structures. American Society of Civil Engineers.

Azzi, Z., Habte, F., Vutukuru, K.S., Chowdhury, A.G., Moravej, M., 2020. Effects of roof geometric details on aerodynamic performance of standing seam metal roofs. Engineering Structures 225, 111303.

Baker, C.J., 2007. Wind engineering—Past, present and future. Journal of Wind Engineering and Industrial Aerodynamics 95, 843–870. https://doi.org/10.1016/j.jweia.2007.01.011

Bienkiewicz, B., Sun, Y., 1997. Wind loading and resistance of loose-laid roof paver systems. Journal of wind engineering and industrial aerodynamics 72, 401–410.

Blocken, B., Carmeliet, J., 2004. A review of wind-driven rain research in building science. Journal of wind engineering and industrial aerodynamics 92, 1079–1130.

Cain, J.H., Banks, D. and Petersen, C., 2015. Wind loads on utility scale solar PV power plants. In Proc. SEAOC Annual Convention, Seattle.

Chanetz, B., 2017. A century of wind tunnels since Eiffel. Comptes Rendus Mécanique, A century of fluid mechanics: 1870–1970 345, 581–594. https://doi.org/10.1016/j.crme.2017.05.012

Choi, E.C., 1999. Wind-driven rain on building faces and the driving-rain index. Journal of Wind Engineering and Industrial Aerodynamics 79, 105–122.

FEMA, 2009. Multi-hazard Loss Estimation Methodology Hurricane Model, HAZUS-MH MR3 Technical Manual; Department of Homeland Security, Federal Emergency Management Agency, Hardening Division: Washington, DC.

FEMA, 2006. Mitigation Assessment Team Report on Hurricane Katrina in the Gulf Coast: Building Performance Observations, Recommendations, and Technical Guidance [Full Report], in: Homeland Security Digital Library. Presented at the United States. Federal Emergency Management Agency, United States. Federal Emergency Management Agency.

FEMA, 1992. Building Performance: Hurricane Andrew in Florida. Observations, recommendations and technical guidance, Federal Insurance Administration-22.

FPHLM, 2015. Florida public hurricane loss model: Research in multi-disciplinary system integration assisting government policy making. State of Florida

International Code Council, Inc. (2017). Testing Application Standard (TAS) 202-94 Criteria for Testing Impact and Nonimpact Resistant Building Envelope Components Using Uniform Static Air Pressure. 2017 Florida Building Code—Test Protocols for High Velocity Hurricane Zone, 978-1-60983-688-7.

Habte, F., Asghari Mooneghi, M., Gan Chowdhury, A., Irwin, P., 2015. Full-scale testing to evaluate the performance of standing seam metal roofs under simulated wind loading. Engineering Structures 105, 231–248. https://doi.org/10.1016/j.engstruct.2015.10.006

Hazelwood, R.A., 1981. The interaction of the two principal wind forces on roof tiles. Journal of wind engineering and industrial aerodynamics 8, 39–48.

Holmes, J.D., 2001. Wind Loading of Structures. CRC Press, London. https://doi.org/10.4324/9780203301647

Kawair, H., Nishimura, H., 2003. Field measurement on wind force on roof tiles, in: Proc., 11th Int. Conf. on Wind Engineering. International Association for Wind Engineering and American Association for Wind Engineering, pp. 599–606.

Kijewski-Correa, T., Roueche, D.B., Mosalam, K.M., Prevatt, D.O., Robertson, I., 2021. StEER: A Community-Centered Approach to Assessing the Performance of the Built Environment after Natural Hazard Events. Frontiers in Built Environment 7, 79. https://doi.org/10.3389/fbuil.2021.636197

Kubilay, A., Derome, D., Blocken, B., Carmeliet, J., 2014. High-resolution field measurements of wind-driven rain on an array of low-rise cubic buildings. Building and environment 78, 1–13.

Li, R., Chowdhury, A.G., Bitsuamlak, G., Gurley, K.R., 2014. Wind Effects on Roofs with High-Profile Tiles: Experimental Study. J. Archit. Eng. 20. https://doi.org/10.1061/(ASCE)AE.1943-5568.0000156

Lin, J., Surry, D., 1997. Simultaneous time series of pressures on the envelope of two large low-rise buildings. University of Western Ontario, Boundary Layer Wind Tunnel Laboratory Report, BLWTL-SS7-1997, for Dr. E. Simiu, National Institute of Standards and Technology, March.

Meecham, D., 1988. Wind action on hip and gable roofs. Faculty of Graduate Studies, University of Western Ontario.

Meeting Research and Education Needs in Coastal Engineering, 1999. The National Academies Press, Washington, DC. https://doi.org/10.17226/9613

NBCC, 2015. National Building Code of Canada, User's Guide- Structural Commentaries (Part 4). Issued by the Canadian Commission on Buildings and Fire Codes, National Research Council of Canada.

Office of Coastal Management, 2021. National Oceanic and Atmospheric Administration, Hurricane Costs. https://coast.noaa.gov/states/fast-facts/hurricane-costs.html

Pan, F., 2014. Damage prediction of low-rise buildings under hurricane winds. LSU Doctoral Dissertations.

Pinelli, J.P., Roueche, D., Kijewski-Correa, T., Plaz, F., Prevatt, D., Zisis, I., Elawady, A., Haan, F., Pei, S., Gurley, K. and Rasouli, A., 2018. Overview of damage observed in regional construction during the passage of Hurricane Irma over the State of Florida. In Forensic Engineering 2018: Forging Forensic Frontiers (pp. 1028-1038). Reston, VA: American Society of Civil Engineers.

Pinelli, J.-P., Gurley, K.R., Subramanian, C.S., Hamid, S.S., Pita, G.L., 2008. Validation of a probabilistic model for hurricane insurance loss projections in Florida. Reliability Engineering & System Safety, 17th European Safety and Reliability Conference 93, 1896–1905. https://doi.org/10.1016/j.ress.2008.03.017

Pita, G.L., Pinelli, J.-P., Gurley, K.R., Hamid, S., 2013. Hurricane vulnerability modeling: Development and future trends. Journal of Wind Engineering and Industrial Aerodynamics 114, 96–105. https://doi.org/10.1016/j.jweia.2012.12.004

Cope, A.D., 2004. Predicting the vulnerability of typical residential buildings to hurricane damage. University of Florida.

Salzano, C.T., Masters, F.J., Katsaros, J.D., 2010. Water penetration resistance of residential window installation options for hurricane-prone areas. Building and Environment 45, 1373–1388.

Spotlight on: Catastrophes - Insurance issues | III, 2020. URL https://www.iii.org/article/spotlight-on-catastrophes-insurance-issues.

Straube, J.E., Burnett, E.F., 2000. Simplified prediction of driving rain deposition. Proceeding of International Building Physics Conference. Eindhoven 375–382.

Strobel, K. and Banks, D., 2014. Effects of vortex shedding in arrays of long inclined flat plates and ramifications for ground-mounted photovoltaic arrays. Journal of Wind Engineering and Industrial Aerodynamics, 133, pp.146-149.

Surry, D., Stathopoulos, T., 1978. An experimental approach to the economical measurement of spatially averaged wind loads. Journal of Wind Engineering and Industrial Aerodynamics 2, 385–397. https://doi.org/10.1016/0167-6105(78)90021-1

United States Census, 2012. Coastline County Population trend. https://www.census.gov/dataviz/visualizations/039/508.php.

Vutukuru, K.S., Alawode, K.J., Bakhtiari, A., Elawady, A., Lee, S.J., Chowdhury, A.G., Lori, G., 2021. Full-scale experimental testing to investigate wind-induced vibrations on curtain wall systems. Proceedings of International Structural Engineering and Construction 8, 1.

Vutukuru, K.S., Moravej, M., Elawady, A., Chowdhury, A.G., 2020. Holistic testing to determine quantitative wind-driven rain intrusion for shuttered and impact resistant windows. Journal of Wind Engineering and Industrial Aerodynamics 206, 104359.

Roberts, S., 2012. Wind wizard: Alan G. Davenport and the art of wind engineering. Princeton University Press.

## 2. EXPERIMENTAL SETUP AND INSTRUMENTATION

### 2.1 Wall of Wind experimental facility

This section briefly describes the Wall of Wind (WOW) experimental facility where the specimen used in this project was constructed, instrumented, and tested. The WOW is an open jet Atmospheric Boundary Layer (ABL) wind tunnel with a 2 x 6 array of fans arranged in arc-focal arrangement with a contraction zone. The facility is capable of testing large-scale models at up to Category 5 hurricane wind speeds of 70m/s (156 mph) (Chowdhury et al. (2017); Chowdhury et al. (2018)) which is the lower limit of Category-5 hurricane on the Saffir Simpson scale. Hence this facility is capable of testing at high Reynolds numbers. The ABL profile is generated by using triangular spires near the fans and the turbulence characteristics (turbulence intensity, and roughness length) are generated using square-shaped automated roughness elements (with different angles for different roughness lengths and scales) downwind of the fans as shown in Figure 2.1.

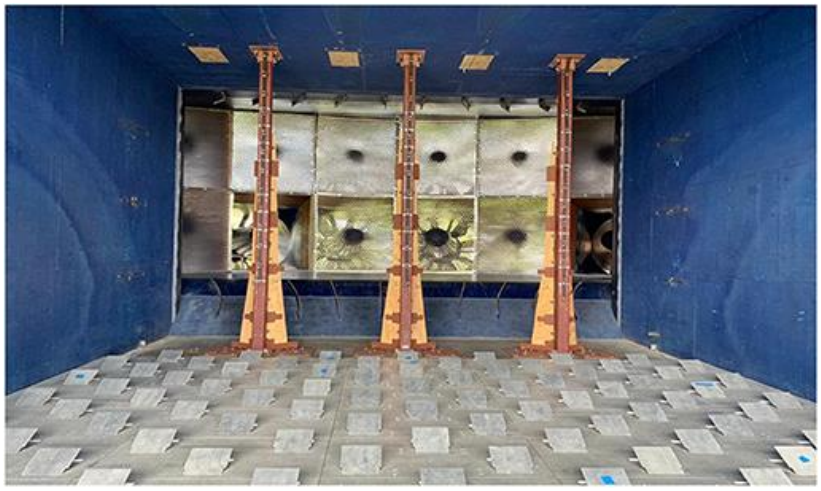

Figure 2.1: Inside flow management box showing roughness elements and spires

The test section is located 4.3 m downwind of the flow management box with a 4.9 m diameter turntable. The turntable, as the name suggests, facilitates testing the structures for different wind directions by rotation of any structure.

## 2.2 Modelling, Construction, Mechanical Properties, and Product Approvals

Most window configurations used in the curtain wall industry in the U.S. are of the Top Hung type (with vertically opening or awning type). Side Hung (with horizontally opening or casement type) is a distant second and Project Out is very rarely used. For awning type windows, current designs are mostly of the extender type (Figure 2.2*: Extender type hinge*), owing to its allowed tolerances in installation and use compared to the more traditional hinge type (Figure 2.3). However, the extender type, in which the vent primarily floats outside and is connected only by thin flexible hinges, is more prone to wind vibrations in the open condition.

Figure 2.2: Extender type hinge

Figure 2.3: Traditional type hinge

The objective of the current research is to study vibrations of operable windows only, however, the interlocking mullion joints (vertical joints in curtainwalls) play a critical role in the performance of the system from a rain intrusion viewpoint. The interlocking action is also expected to contribute to the dynamic behavior of the window system, especially in the open condition. The curtain wall model constructed for this study comprised of 3-façade (double-glazing) units with overall dimensions of 3.65 m (width) x 3.18 m (height). These are mounted on a 3.65 m (width) x 1.83 m (breadth) rectangular plan building with a 3.18 m height and a flat wooden roof with 0.41 m overhang. To facilitate economical testing, all the obtained parameters (pressures, accelerations, and strains) are considered simultaneously on the same building. To achieve this, on the long wall on one side, a polycarbonate window (of the same geometry) with drilled holes for pressure testing was used, keeping the other long wall with a glass operable window. This setup correctly assumes that the wind pressures do not change with the rigidity of the test surface and the important geometric similarity was maintained for both the windows. The other two walls on the 1.83 m length of the building are made of wood, with a door structure at one of the walls. This door provided access to the inside of the model to allow the placing of instrumentation. During tests, this door was sealed. All the walls were fixed to a steel frame and bolted to the wind tunnel turntable.

The steel frame provides high rigidity. Figure 2.4, Figure 2.5, and Figure 2.6 show the plan, elevation, and mullion cross-section of the designed curtainwall unit respectively. Figure 2.7 shows the composition in terms of outer, inner, and air gap thickness for the whole curtain wall as well as the operable window. Figure 2.8, and Figure 2.9 show,

respectively, the framing profile cross-sections and their inertial properties. Figure 2.10 shows a photo of the specimen on the WOW EF turntable, with an operable window component.

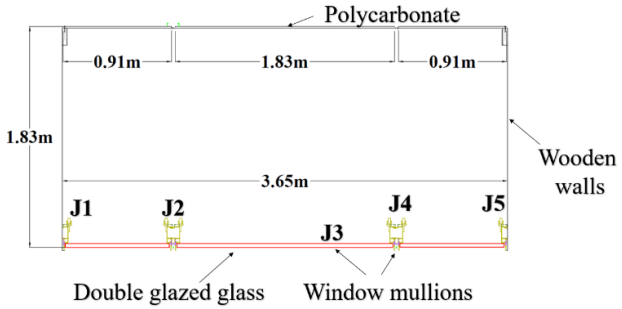


Figure 2.4: Plan of unitized curtainwall

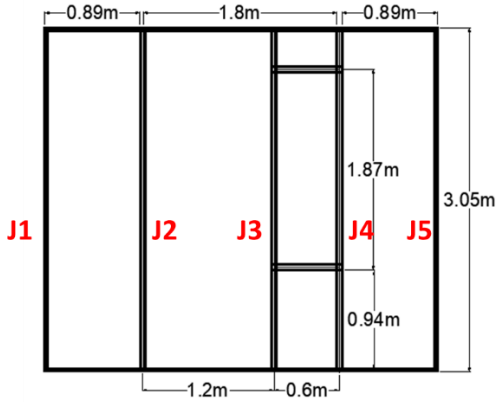


Figure 2.5: Elevation of unitized curtainwall

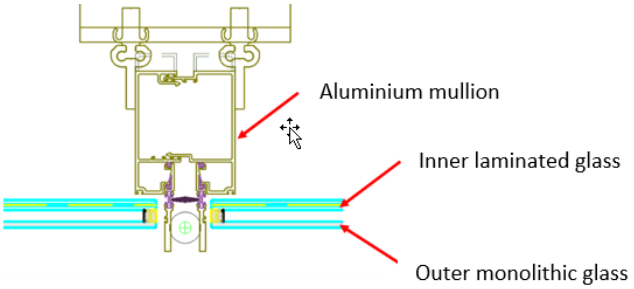


Figure 2.6: Section along Joint J3

| | Outer | Inner | Gap |
|---|---|---|---|
| | 6mm | 5mm+ 0.76m+ 5mm | 12mm |
| | 6mm | 6mm | 16mm |
| | 6mm | 5mm+ 0.76m+ 5mm | 12mm |
| | 6mm | 5mm+ 0.76m+ 5mm | 12mm |
| | 10mm | 6mm | 12mm |

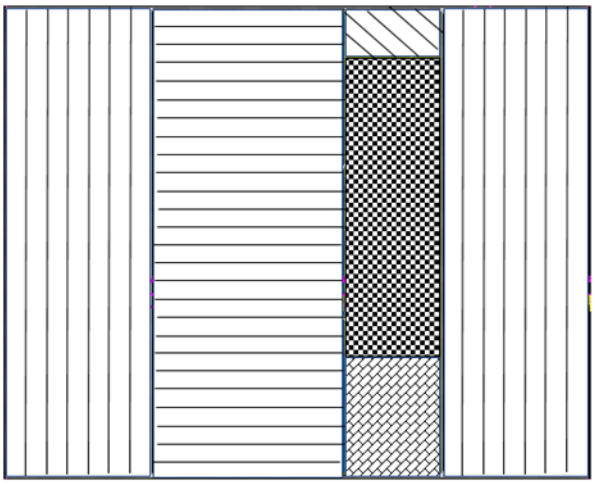

Figure 2.7: Glazing compositions

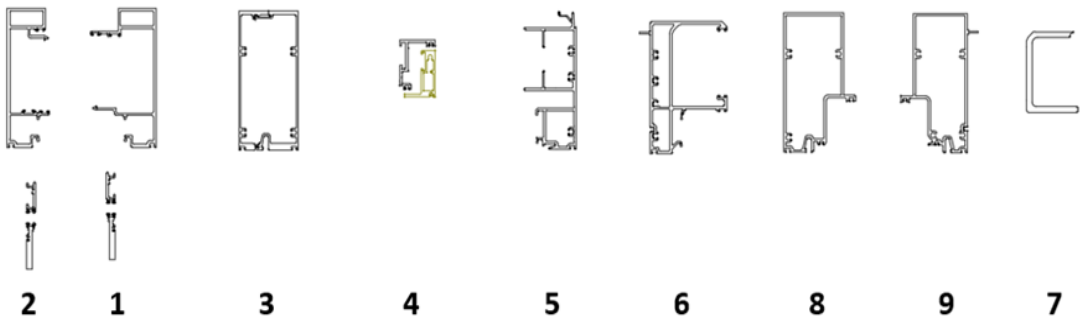


Figure 2.8: Framing profile cross-sections

| N | Member | Area [mm²] | IXX [in⁴] | IYY [in⁴] | IXY [in⁴] | ZX [in³] | ZY [in³] |
|---|---|---|---|---|---|---|---|
| 1 | Left Mullion | 1652 | 3.77e6 | 5.53e5 | -1.93e5 | 4.58e4 | 9.01e3 |
| 2 | Right Mullion | 1587 | 3.64e6 | 2.84e5 | 1.74e5 | 4.78e4 | 1.03e4 |
| 3 | Intermediate Mullion | 1619 | 5.39e6 | 2.59e5 | 2.36e5 | 6.41e4 | 7.54e3 |
| 4 | Operable | 445 | 1.42e5 | 3.04e4 | 2.78e4 | 5.08e3 | 1.15e3 |
| 5 | Bottom Transom | 1329 | 2.76e6 | 4e5 | 4.49e4 | 3.31e4 | 9.67e3 |
| 6 | Top Transom | 1729 | 3.77e6 | 1.21e6 | 3.1e5 | 4.87e4 | 1.95e4 |
| 7 | C Shape Profile | 1187 | 1.4e6 | 3.66e5 | 5.54e4 | 2.98e4 | 0.54 |
| 8 | Intermediate Bottom Transom | 1355 | 3.53e6 | 1.05e6 | 2.56e5 | 4.49e4 | 1.26 |
| 9 | Intermediate Top Transom | 1355 | 3.54e6 | 8.95e5 | -1.91e5 | 4.52e4 | 1.12 |


Figure 2.9: Frame mechanical properties

Figure 2.10: Curtainwall specimen on Turntable

A summary of product approvals/performance standards obtained for the tested curtainwall specimen, including rain ingress tests and standards, is presented below. ASTM E283 requires that air leakage across a glazing area in a laboratory should be less than 0.06 CFM/ft$^2$, for a minimum static air differential pressure of 6.24 psf; for a projected window with the same windward pressure, the air leakage limit should be 0.09 CFM/ft. For wind serviceability, ASTM E330 suggests that the deflection resulting from the application of a uniform pressure shall not exceed the specified deflection ratio or limit produced by the specified design wind pressures and suctions for edge zones. These wind pressures are typically applied for 10 seconds. For inter-story drift, AAMA 501.4 recommends studying inter-story drift by applying a load and releasing it through three cycles, and visually inspect for any damage. The structure is said to fail against this criterion if there is gross distortion or deformation of anchors, frames, glass, or panels, as well as no gasket disengagement or structural sealant failures or loss of performance. For static-air pressure water penetration tests, ASTM E331 suggests a test with 20% positive design pressure (or 15 psf, whichever is larger) differential across the specimen with rain

for fifteen minutes. No evidence of water penetration is to be observed for this test. AAMA 501.1 requires that dynamic pressure be applied for the same duration and with the same pressure as specified in ASTM E331 (as discussed in Williams and Kistler (2014), and that any signs of water penetration are observed would be considered a fail. For water penetration tests condensation is acceptable under three conditions: 1) water is contained and drained to the exterior, 2) there is no wetting of a surface that would be visible to building occupants, and 3) there would be no staining or other damages to the completed building and its furnishings. In addition, several standards, including AAMA 501.5, require confirmation of thermal performance, thermal resistance, and structural resistance. Once the standard requirements are met, typically a load of 600 lbs. is applied parallel and perpendicular to the glass for 10 seconds and any deformation to the anchor is observed. The frames are designed in accordance with an Aluminum design manual (EN 1991-1:2007). The hardware and the brackets must comply with the requirements of the AISC steel construction manual and AAMA TIR A9-14. Table 1 below summarizes the testing protocols with brief notes to perform these tests.

Table 1: Curtainwall window codes and standards

| **Standard Test** | **Type of Load** | **Specified Load** | **Specified Number of Cycles** | **Notes** |
|---|---|---|---|---|
| ASTM E283 | Static | 299 Pa (6.24 psf) | N/A | Lab test<br>Infiltration must be less than 0.06CFM per sq. ft of glazing and 0.09 CFM/ft per feet of projected window |
| ASTM E330 | Static | Design wind pressure | N/A | Lab test<br>Inter-story drift and deflection must be within serviceability limits for an applied 10-sec load. No gasket disengagement or structural failures |
| ASTM E331 | Static | Largest of 20% DP or 718 Pa (15 psf) | N/A | Lab Test<br>with a rain spray rate of 3.4L/m².min (5.0 U.S. gal/ft².h) for 15 minutes no water infiltration must be observed |

Table 1 continued: Curtainwall window codes and standards

| | | | | |
|---|---|---|---|---|
| ASTM E1105-05(A) | Static | Largest of 20% DP or 718 Pa (15 psf) | N/A | Field Test<br>with a rain spray rate of 3.4L/m².min (5.0 U.S. gal/ft².h) for 15 minutes no water infiltration must be observed |
| ASTM E1105-05(B) | Cyclic Static | Largest of 20% DP or 718 Pa (15 psf) | Minimum of 3 | Field Test<br>with a rain spray rate of 3.4L/m².min (5.0 U.S. gal/ft².h) for 15 minutes no water infiltration must be observed |
| ASTM E547-00 | Cyclic Static | 137 Pa (2.86psf) | Unspecified | Lab Test<br>with a rain spray rate of 3.4L/m².min (5.0 U.S. gal/ft².h) no water infiltration must be observed |
| BS EN 12155 | Static | Depends on rating pressure | N/A | Lab Test<br>with rain spray rate of<br>2l/m².m no water infiltration must be observed |

Table 1 continued: Curtainwall window codes and standards

| | | | | |
|---|---|---|---|---|
| BS EN 13050 | Dynamic | 37.5% of Design Pressure | Unspecified | Lab Test<br>with a rain spray rate of 2l/m².m, no water infiltration must be observed |
| BS EN 13051 | Static | No Loads, Annex B suggests the use of BS EN 12155 loadings if air pressure is required | N/A | Field Test<br>with a rain spray rate of 5l/min per meter, no water infiltration must be observed |
| BS EN 12865 | Pulsating Load | Incremental Steps of 150Pa | As much as needed | Lab Test (Limit of water tightness)<br>with a Run-off rate of 1.2l/(m.min) and a Driving rain rate of 1.5l/(m.min), no water infiltration must be observed |
| AAMA 501.1-05 | Dynamic | 300.0 Pa, 380.0Pa, 480.0 Pa, 580.0 Pa and 720.0Pa. | One 15 min cycle at a time | Lab Test/ Field Test<br>with a rain rate of 3.4L/m². min (5.0 U.S. gal/ft².h) no water infiltration must be observed |

## 2.3 Instrumentation and testing protocol

As explained in Section 2.2, the specimen consisted of two types of windows on the long wall of the building, the polycarbonate side with holes needed to install pressure taps for measuring the differential pressure across the window surface. The external and internal pressure tap layout is shown in Figure 2.11, and Figure 2.12 respectively. On the glass window, accelerometers and strain gauges are installed at critical locations. Figure 2.13, and Figure 2.14 show accelerometer and uni-axial strain gauge (along the long side) locations for closed window testing on the aluminum window frame and bi-axial strain gauge and accelerometers on the glass surface respectively. *Figure 2.17*: Strain gauges on connection hardware, Phase II

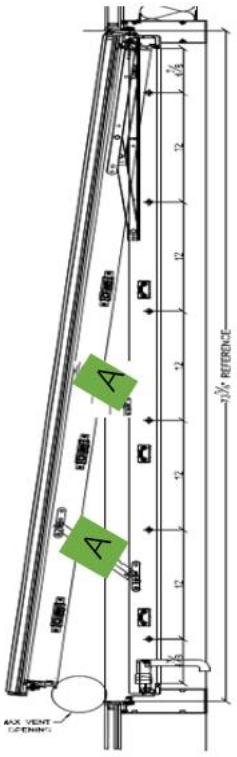


Figure 2.18: Accelerometers on connection hardware, Phase II

Figure 2.15 and Figure 2.16 show accelerometer and tri-axial strain gauge (0-45-90) locations for open window testing. Additional accelerometers and uni-axial strain (along the hardware long axis) gauges on hardware components are illustrated in Figure 2.17 and Figure 2.18. All the accelerometers installed were tri-axial with X direction towards the width, Y towards the height, and Z out-of-plane direction. For rain intrusion tests, custom polycarbonate glass was fabricated and used as a water collection bucket for the window, as in the previous testing performed at WOW (Vutukuru et al., 2020). Figure 2.19 shows the dimensions of the water collection bucket. An assembled rainwater collection system is shown in Chapter 4 of this dissertation.

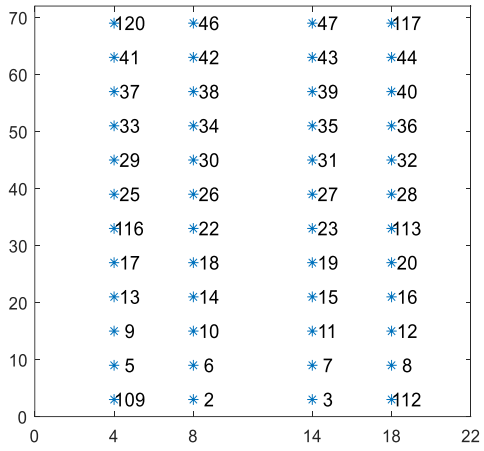


Figure 2.11: External pressure tap layout

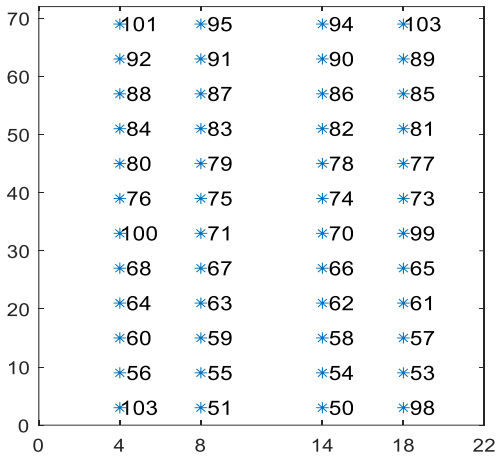


Figure 2.12: Internal pressure tap layout

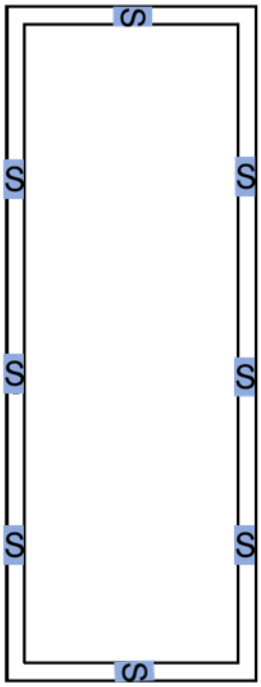


Figure 2.13: Strain gauges on the Window frame, Phase I

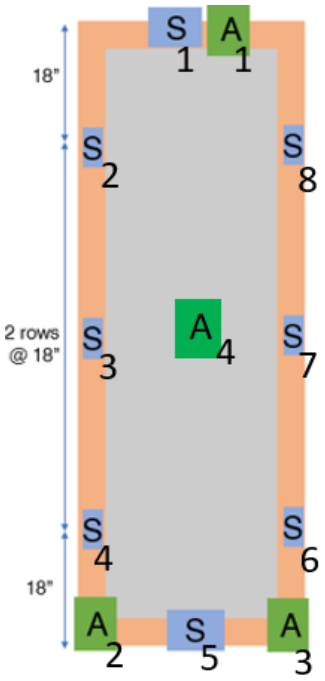


Figure 2.14: Strain gauges and accelerometers on Window glass, Phase II

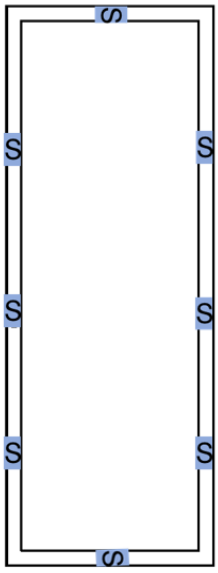


Figure 2.15*:* Strain gauges on the Window frame, Phase II

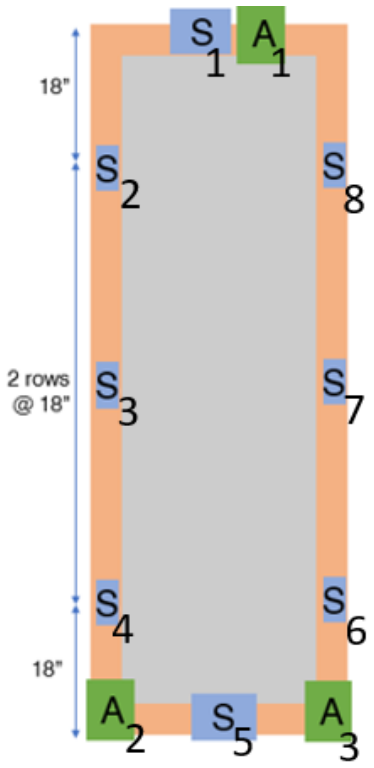


Figure 2.16: Strain gauges and accelerometers on Window glass, Phase II

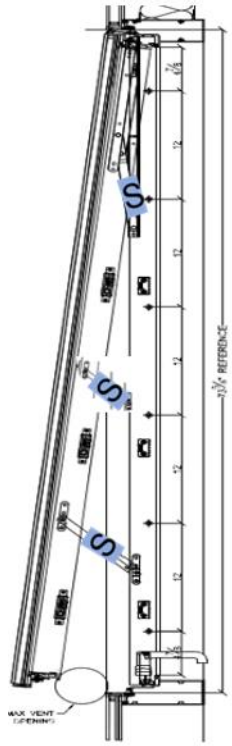


Figure 2.17: Strain gauges on connection hardware, Phase II

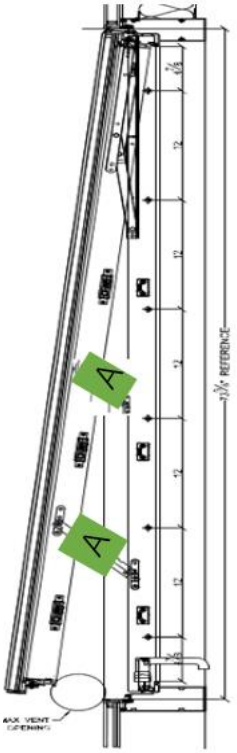

Figure 2.18: Accelerometers on connection hardware, Phase II

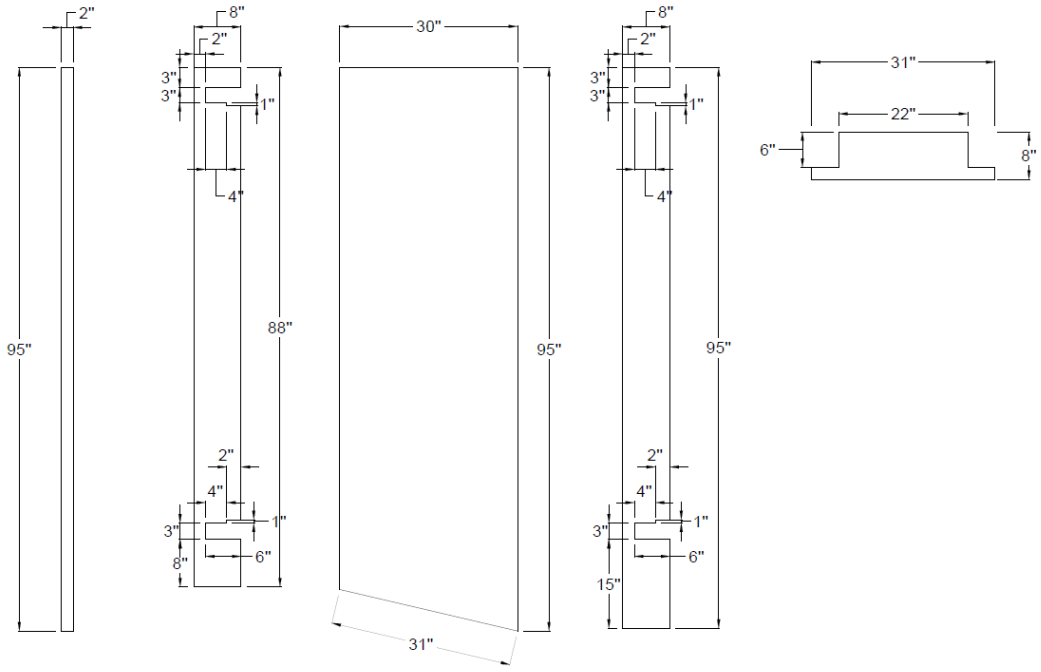


Figure 2.19: Rain collection system with a tap-drain mechanism

The testing was performed in three phases. The first phase consisted of testing the window in a closed condition with wind speeds ranging from 35. 76 m/s (80 mph) to 44.7 m/s (100 mph) with 4.5 m/s (10 mph) increments. Several wind directions starting from windward direction 0 $^0$ (windward direction) to 315 $^0$ are tested with 45 $^0$ increments to study any possible vibrations of operable awning-type window systems. The second phase consisted of testing the window in the open condition to understand the dynamics and possible vibration effects on the window frame. These tests are performed from 22.3 m/s (50 mph) to 31.3 m/s (70 mph) with 4.5 m/s (10 mph) increments. The tested wind directions include finer increments (every $10^0$) for critical angles ($60^0$ to $120^0$ and $240^0$ to $300^0$) and at $45^0$ increments to study the effect of remaining wind directions. The third phase consisted of testing the unitized curtainwall specimen against simulated full-scale

wind-driven rain with hurricane-force winds. All the tests were performed under simulated full-scale open terrain conditions. Table 2 below summarizes the test protocol for all wind speeds tested and Figure 2.20 shows the wind direction specified in the table.

Table 2: Testing protocol

| **Phase** | **Wind Speed m/s** | **Wind Direction (degree)** | **Test Duration (mins.)** |
|---|---|---|---|
| I (window open) | 22.3, 26.8, 31.3 | 0,45,60,70,80,90,100,110,120,135,180,225,240,250, 260, 270,280,290,300,315 | 10 |
| II (window closed) | 35.8,40.23, 44.7 | 0,45,90,135,180, 225, 270, 315 | 10 |
| III (wind driven rain) | 29.1 | 0,15,345 | 15 |
| III (wind-driven rain) | 44.7 | 0,15,345 | 5 |
| III (Wind driven rain) | 58.1 | 0,15,345 | 5 |

Destructive testing was also performed keeping the window open and successively increasing the wind speed by 2.23 m/s (5 mph) for the windward direction to find the failure wind speed for this window.

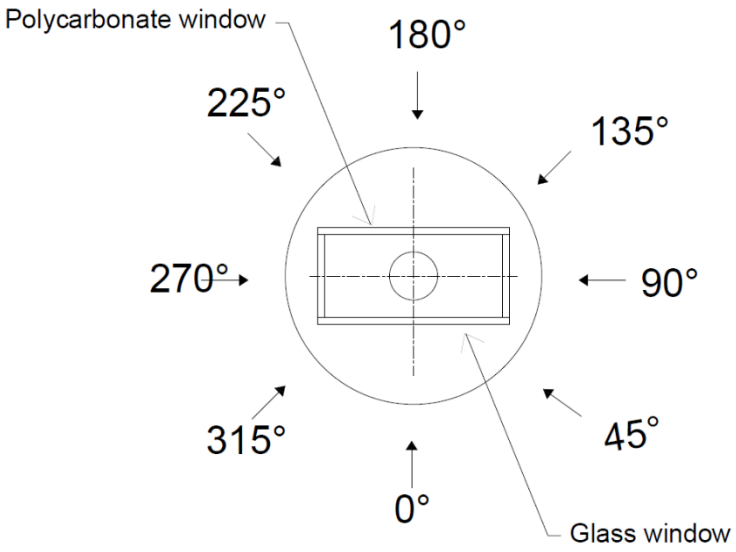


Figure 2.20: Test protocol wind directions

## 2.4 Chapter 2 references


Aluminum Design Manual 2020 | The Aluminum Association [WWW Document], 2020. URL https://www.aluminum.org/aluminum-design-manual-2020-0.

American Architectural Manufacturer's Association, 501.1, Standard Test Method for Water Penetration of Windows, Curtainwalls, and Doors using Dynamic Pressure. AAMA.

American Architectural Manufacturer's Association, 501.4, Recommended Static Test Method for Evaluating Window Wall, Curtain Wall and Storefront Systems Subjected to Seismic and Wind-Induced Inter-Story Drift. AAMA.

American Architectural Manufacturer's Association, 501.5, Procedures recommended for evaluating the effects of thermal movement on large wall sections. Includes standardized approach for thermal cycle testing of joints, anchors, and other components of exterior walls. AAMA.

American Architectural Manufacturer's Association, TIR A9-14, Design Guide for Metal Cladding Fasteners, AAMA.

American Institute of Steel Construction, Steel Construction Manual, 15th Ed.., URL https://www.aisc.org/Steel-Construction-Manual-15th-Ed-Print.

American Society for Testing and Materials, E0283, E06 Committee, Test Method for Determining Rate of Air Leakage Through Exterior Windows, Curtain Walls, and Doors Under Specified Pressure Differences Across the Specimen. ASTM International. https://doi.org/10.1520/E0283_E0283M-19

American Society for Testing and Materials, E0330, E06 Committee. Test Method for Structural Performance of Exterior Windows, Doors, Skylights and Curtain Walls by Uniform Static Air Pressure Difference. ASTM International. https://doi.org/10.1520/E0330_E0330M-14

American Society for Testing and Materials, E0331, E06 Committee. Test Method for Water Penetration of Exterior Windows, Skylights, Doors, and Curtain Walls by Uniform Static Air Pressure Difference. ASTM International. https://doi.org/10.1520/E0331-00R16

American Society for Testing and Materials, E1105, E06 Committee. Test Method for Field Determination of Water Penetration of Installed Exterior Windows, Skylights, Doors, and Curtain Walls, by Uniform or Cyclic Static Air Pressure Difference. ASTM International, https://doi.org /10.1520/E1105-15

British Standards Institution, 12155, 2000. Curtain walling. Watertightness. Laboratory test under static pressure. BS EN 12155. https://shop.bsigroup.com/products/curtain-walling-watertightness-laboratory-test-under-static-pressure?pid=000000000030011664

British Standards Institution, 12865, 2001. Hygrothermal Performance of Building Components and Building Elements. Determination of the Resistance of External Wall Systems to Driving Rain under Pulsating Air Pressure.BS EN 12865. https://shop.bsigroup.com/products/hygrothermal-performance-of-building-components-and-building-elements-determination-of-the-resistance-of-external-wall-systems-to-driving-rain-under-pulsating-air-pressure?pid=000000000030025269.

British Standards Institution, 13050, 2001. Curtain Walling. Watertightness. Laboratory Test under Dynamic Condition of Air Pressure and Water Spray. BS EN 13050. https://shop.bsigroup.com/products/curtain-walling-watertightness-laboratory-test-under-dynamic-condition-of-air-pressure-and-water-spray/preview

British Standards Institution, 13051, 2001. Curtain Walling. Watertightness. Site Test under Dynamic Condition of Air Pressure and Water Spray. BS EN 13051. https://shop.bsigroup.com/products/curtain-walling-watertightness-site-test?pid=000000000030040604

Gan Chowdhury, A., Vutukuru, K.S., Moravej, M., 2018. Full-and Large-Scale Experimentation Using the Wall of Wind to Mitigate Wind Loading and Rain Impacts on Buildings and Infrastructure Systems, in: Proceedings of the 11th Structural Engineering Convention (SEC18). Jadavpur University India.

Gan Chowdhury, A., Zisis, I., Irwin, P., Bitsuamlak, G., Pinelli, J.P., Hajra, B., Moravej, M., 2017. Large-scale experimentation using the 12-fan wall of wind to assess and mitigate hurricane wind and rain impacts on buildings and infrastructure systems. Journal of Structural Engineering (United States) 143. https://doi.org/10.1061/(ASCE)ST.1943-541X.0001785

Vutukuru, K.S., Moravej, M., Elawady, A., Chowdhury, A.G., 2020. Holistic testing to determine quantitative wind-driven rain intrusion for shuttered and impact resistant windows. Journal of Wind Engineering and Industrial Aerodynamics 206, 104359.

Williams, M., Kistler, J., 2014. Utilizing a Modified AAMA 501.1 Dynamic Wind Generation to Simulate Wind-Driven Rain in Windows, Curtain Walls, Architectural Metal Walls, Masonry, EIFS, and Concrete Facades. Building Walls Subject to Water Intrusion and Accumulation: Lessons from the Past and Recommendations for the Future. https://doi.org/10.1520/STP154920130042

# 3. HOLISTIC FULL-SCALE TESTING TO DETERMINE WINDOW SYSTEM VULNERABILITY TO WIND FLUCTUATIONS

The knowledge gap to understand the failure of product-approved window systems due to wind-induced vibration was established in this dissertation. This chapter studies dynamic effects by analyzing the full-scale testing results on operable window systems. A validated analytical model was developed based on the accelerometer results to predict the response of such window systems.

## 3.1 Wind Speed and Pressure results

An open terrain wind speed characteristics were obtained in WOW for the current study and the wind speed characteristics are measured in time-domain using six cobra probes along the building height at the turn table center. The power spectral density comparison at roof height of the tested specimen, and a match with the Von Karman spectrum was obtained for a roughness length, $Z_0$=0.08m. within the open terrain range (refer Figure 3.1). Figure 3.2 show the experimental and ESDU (85020) data match (for $Z_0$ of 0.08m.) obtained for velocity profile and turbulence intensity profile respectively. From Figure 3.1 it can be observed that the low-frequency energy content was missing from the spectrum and this was incorporated into pressure data by using the statistical Partial Turbulence Simulation (PTS) method (explained in Asghari Mooneghi et al. (2016) and Moravej (2018) and into accelerometer data using a transfer function based on the difference observed in the velocity spectrum as explained in Section 3.4.

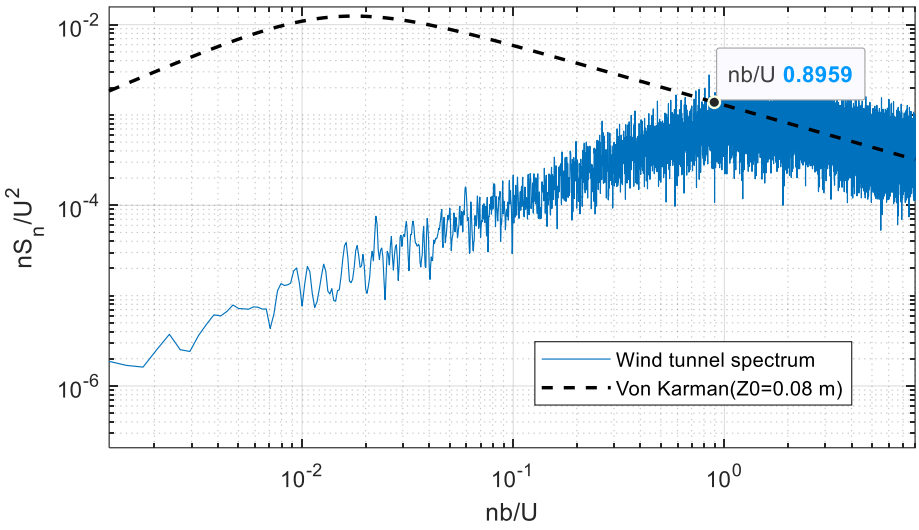


Figure 3.1: Wind gust spectrum

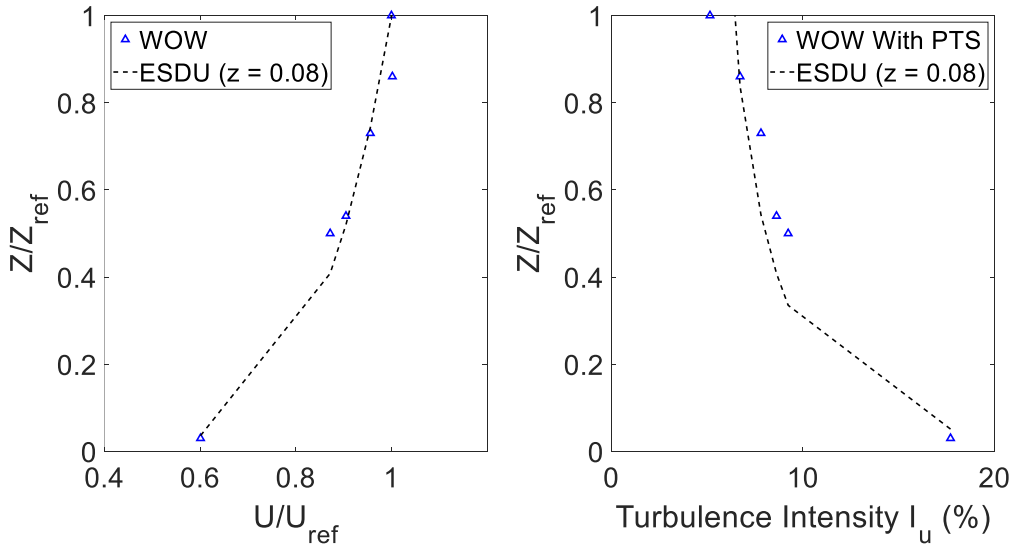


Figure 3.2: Wind Velocity and turbulence intensity profile comparison with ESDU

The pressure was measured by the Scanivalve system using a total tubing length of 61 in. (49 in. on the tubing side and 12 in. on the connector side). The distortions due to the long tubing length were then corrected by a tubing transfer function (explained in

Irwin et al. (1979). PTS method was then applied to the corrected data to incorporate missing low-frequency components. To compare with ASCE 7, pressures are converted into non-dimensional pressure coefficients by using formulas in Equation 1 and Equation 2.

$$Cp_{,mean} = \frac{P_{mean}}{\frac{1}{2}\rho U_{mean}^2} \quad (1)$$

$$Cp_{,peak} = \frac{P_{peak}}{\frac{1}{2}\rho U_{3s}^2} \quad (2)$$

where $U_{mean}$ and $U_{3s}$ are the mean and peak 3s wind speeds at the roof height of the model, is the air density while $P_{mean}$ and $P_{peak}$ are the differential mean and peak pressures (averaged over 3-sec). Figure 3.3, Figure 3.4, and Figure 3.5 show the contour plots of $Cp_{,mean}$ for various wind directions. The pressure differential observed across the window was almost uniform and $45^0$ and $315^0$ show positive $Cp_{,mean}$ values while $135^0$ and $225^0$ show negative $Cp_{,mean}$ values. This could be attributed to the flow separation phenomenon as explained in Section 1.3. For wind directions, refer to Figure 2.20.

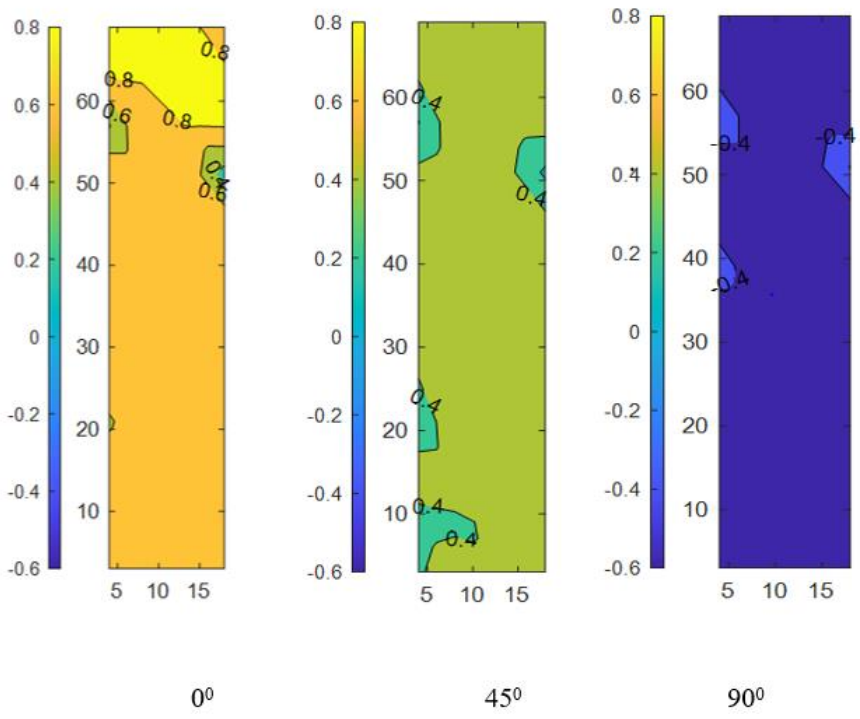


Figure 3.3: Phase I, $Cp_{,mean}$ for first quadrant wind directions

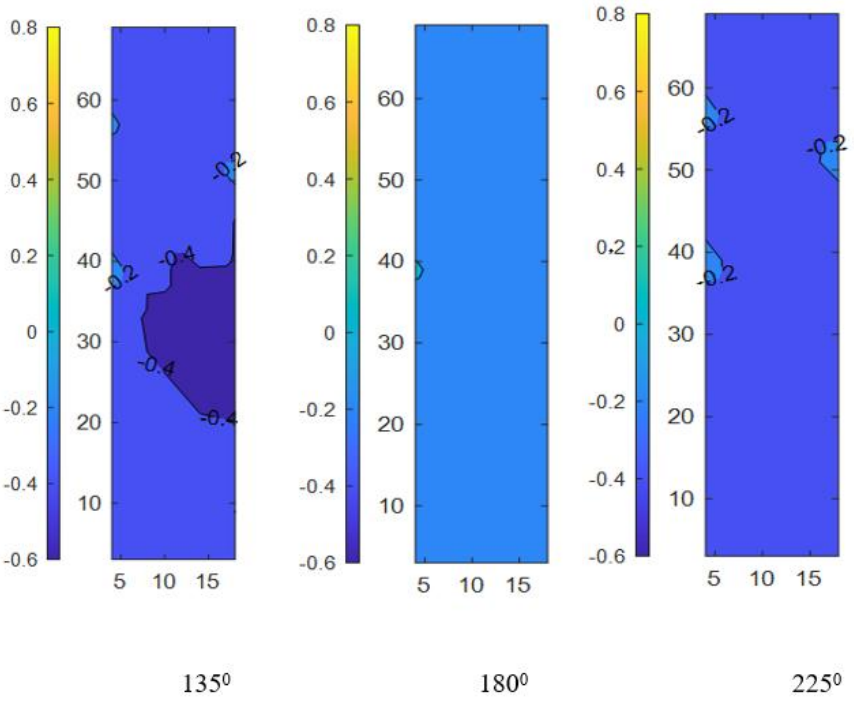


Figure 3.4: Phase I, $Cp_{,mean}$ for second and third quadrant wind directions

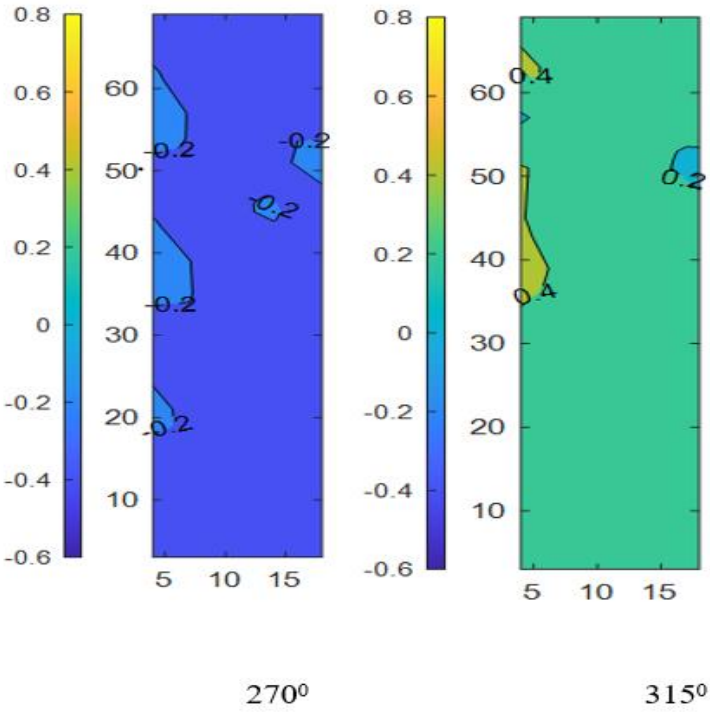


Figure 3.5: Phase I, $Cp_{,mean}$ for fourth quadrant wind directions

These $Cp_{,peaks}$ from the experiments are typically termed as observed peaks whereas typically in wind engineering, actual $Cp_{,peaks}$ are obtained by Best Linear Unbiased Estimators (BLUE) method (explained in Lieblein (1976)). The peaks obtained for phase I (closed window condition) were converted to actual peaks using the BLUE method with a probability of non-exceedance (PNE=0.78) and are plotted as contours shown in Figure 3.6, Figure 3.7, and Figure 3.8.

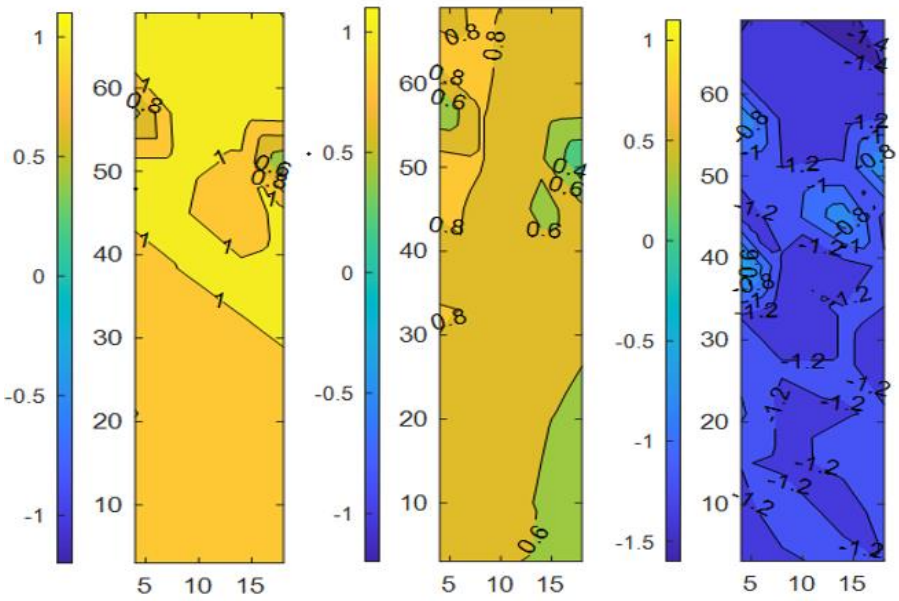


Figure 3.6: Phase I, $Cp_{,peak}$ for first quadrant wind directions

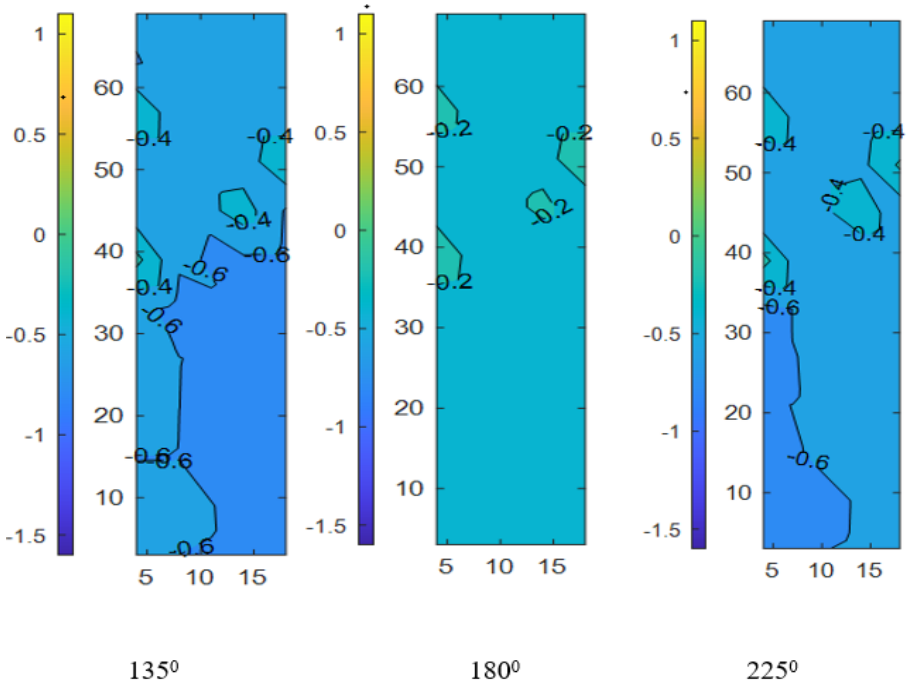


Figure 3.7: Phase I, $Cp_{,peak}$ for second and third quadrant wind directions

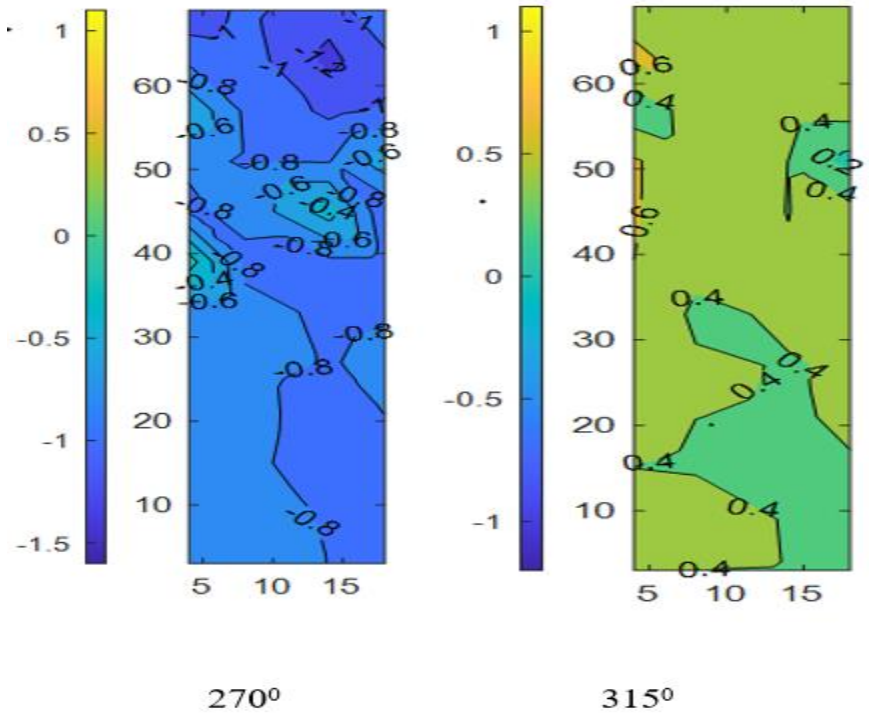


Figure 3.8: Phase I, $Cp_{,peak}$ for fourth quadrant wind directions

For phase I, the worst-case (for $90^0$ wind direction) area averaged $Cp_{,peak}$ was noted as 1.21 which is higher than the ASCE recommended value of 1.08 for closed window design. It is important to note that the worst-case $Cp_{,peak}$ is possibly due to flow separation leading to suction zone pressures on the window.

Similarly, results for the Phase II (open window) condition were presented in Figure 3.9, Figure 3.10, and Figure 3.11. Figure 3.12, Figure 3.13, and Figure 3.14 show the actual $Cp_{,peak}$ contours after tubing transfer function, PTS, and BLUE method. The contours clearly show the suction pressures and hence again show the concept of flow separation for the tested window case.

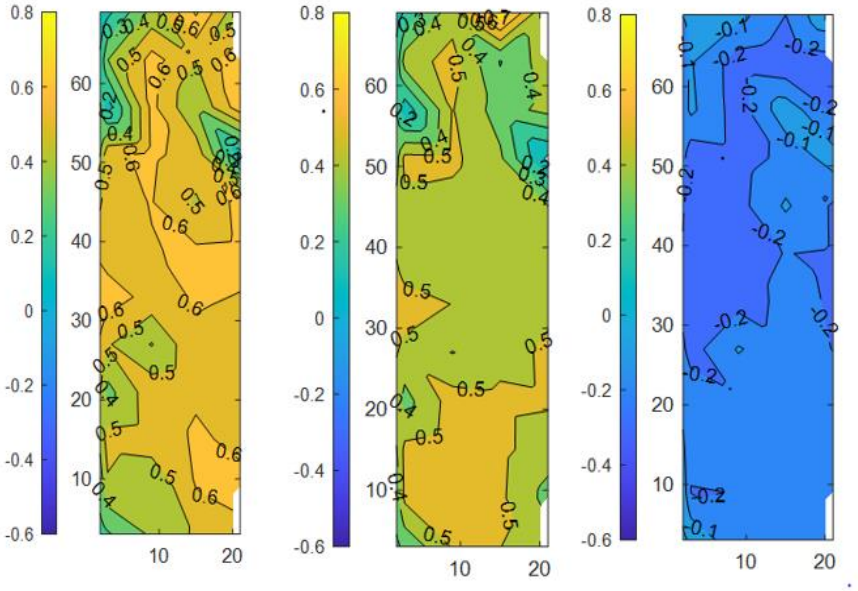


$0^0$ $45^0$ $90^0$

Figure 3.9: Phase II, $Cp_{,mean}$ for first quadrant wind directions

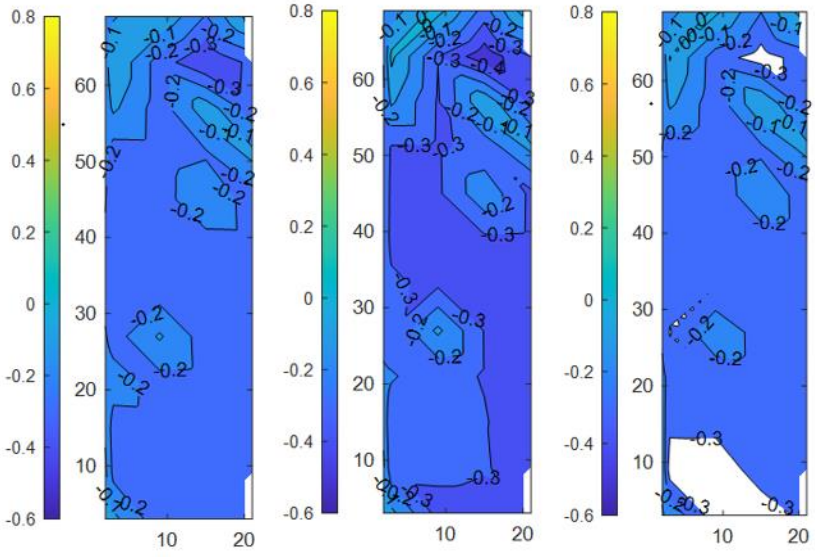


$135^0$ $180^0$ $225^0$

Figure 3.10: Phase II, $Cp_{,mean}$ for second and third quadrants

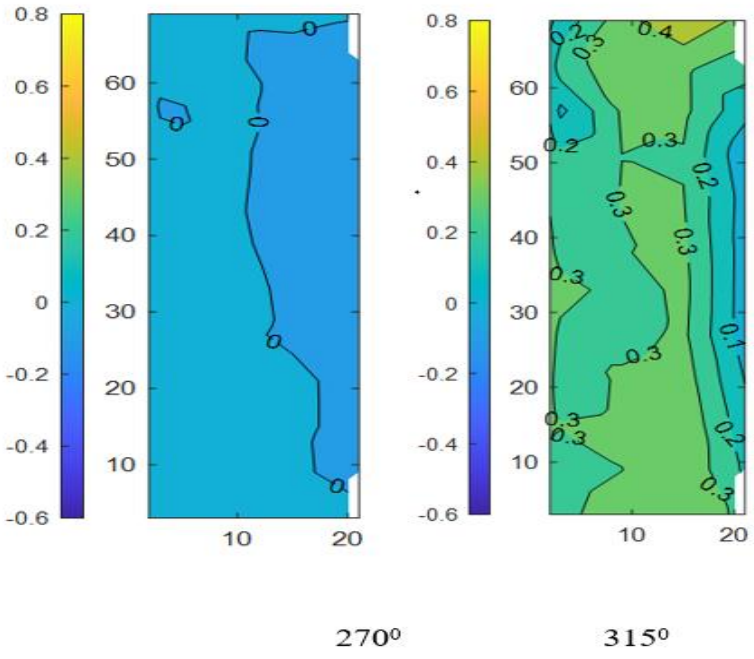


Figure 3.11: Phase II, $Cp_{,mean}$ for fourth quadrant wind directions

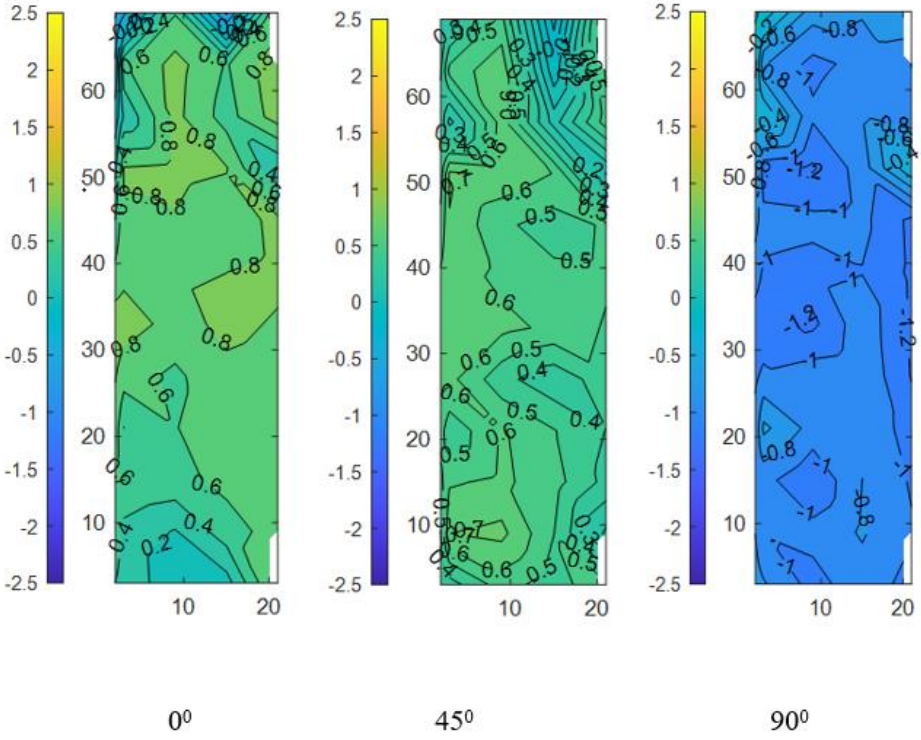


Figure 3.12: Phase II, $Cp_{,peak}$ for first quadrant wind directions

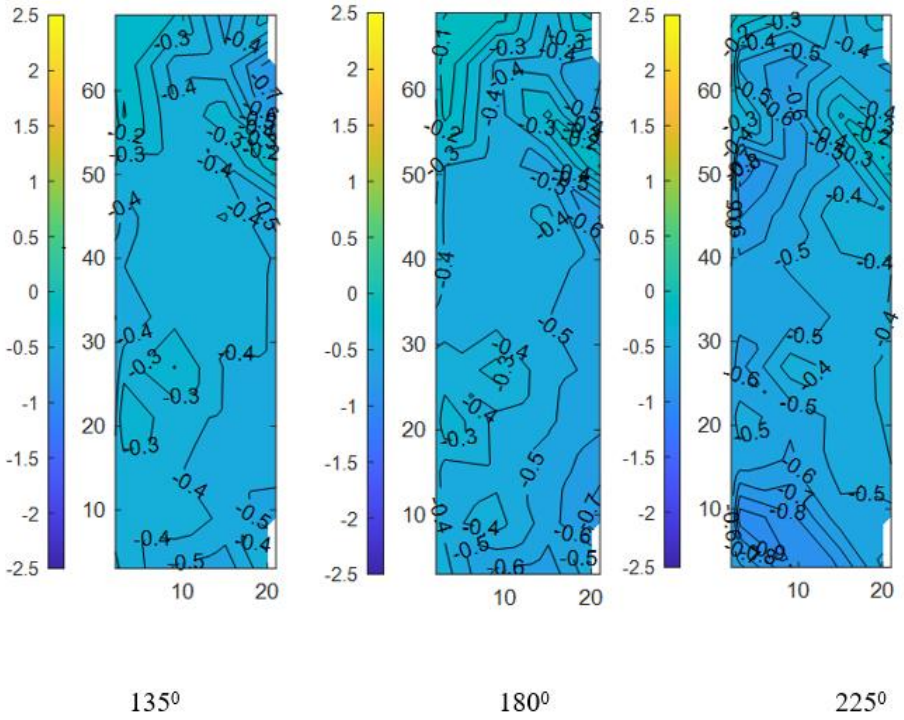


Figure 3.13: Phase II, $Cp_{,peak}$ for second and third quadrant wind directions

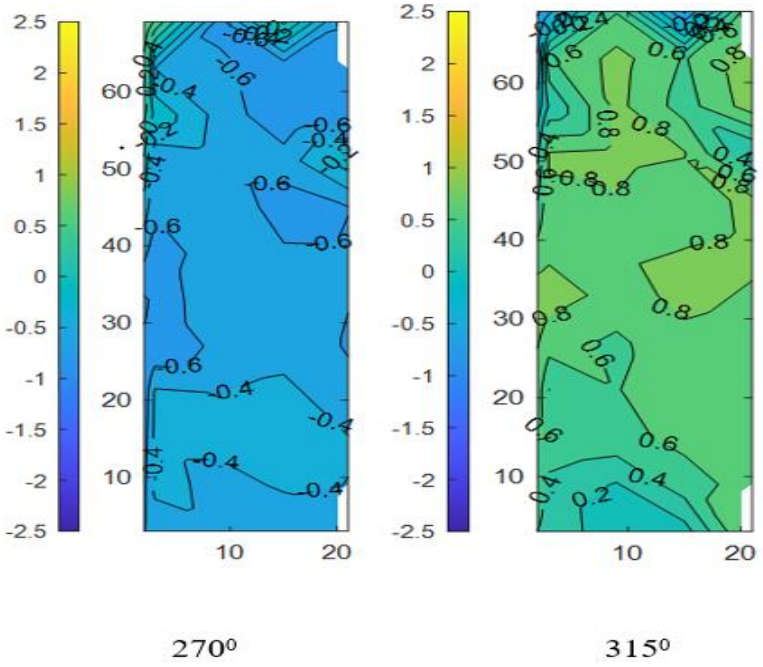


Figure 3.14: Phase II, $Cp_{,peak}$ for fourth quadrant wind directions

Contrary to the closed condition, the value of the worst area averaged $Cp_{,peak}$ was noted as -1.04 and this value is well below the design value of -1.45 for open window condition as per ASCE 7. There was also difference in $90^0$ and $270^0$ pressure results due to geometrical asymmetry. Typically, from design perspective same positive and suction pressures are used, but these contours show that the suction pressures are more critical in comparison to positive pressures for both open and closed conditions. The ASCE 7 design Cp ($GCp-GCp_{,i}$) values suggested for the window are ± 1.45 and ± 1.08 for open and closed window cases respectively and based on the test results it can be concluded that ASCE 7 is conservative from a pressure perspective for open condition, however for closed window case higher $Cp_{,peak}$ values were observed from these tests. The wind pressures obtained from these pressure contours could be multiplied by their corresponding areas to obtain the total wind load on the window system. This load was used to calculate the support loads and to develop vulnerability curves as shown in Section 3.4.

**3.2 Window glass vibration**

The conclusions for phase I testing were primarily based on the glass vibration in closed window condition while for phase II focus was on the supporting hinges (hardware) connecting the window to the frame. This section studied the effects of glass vibration by analyzing accelerometer data while Section 3.4 studied the effect of hardware vulnerability based on accelerometer and strain gauge results.

The hammer impact test was performed without the action of wind to calculate the structural damping of the window system. Methods to find damping from such tests can

be briefly classified into time-domain methods and frequency domain methods. Time-domain methods include Random Decrement Method (discussed in Vandiver et al. (1982), Brincker (1995), Asmussen (1997), and Rodrigues and Brincker (2005), typically used in conjunction with Ibrahim time method (Ibrahim and Mikulcik, 1977) for modal analysis), Logarithmic Decrement Method (explained in Chopra (2017)), Exponential curve fitting (discussed in Perl (1960)) and frequency domain methods include Iterative Least Square method (Goldstein (1989), Chowdhury and Sarkar, (2003)) half-power point method (Olmos and Roesset (2010)), etc. shows the impact test results of the accelerometer for damping estimation. It was assumed that the time domain methods provide accurate damping estimates because of the inherent error in Fourier transform for converting into frequency domain. Figure 3.15 shows a snipped time history of accelerometer showing the positive peaks used for estimation of damping using the exponential fit method for seven cycles. Note that this data is obtained by removing an offset (possible effect of gravity on the accelerometer) and is only shown for illustration purposes. The total data would have a mean of 0 $m/s^2$.

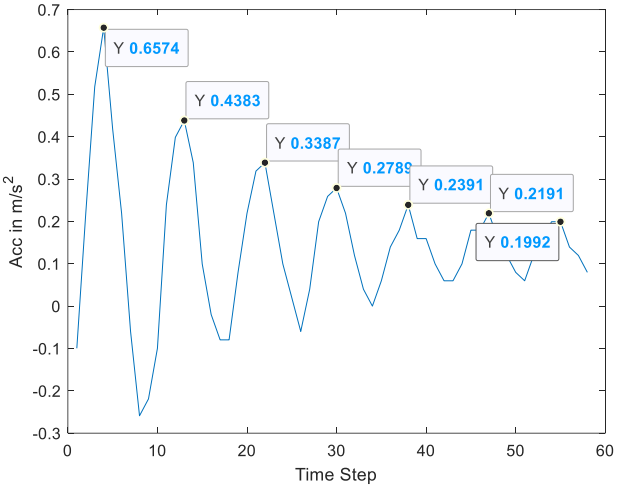


Figure 3.15: Identification of positive peaks for damping estimation

The accelerometer response was converted to the frequency domain using Frequency Domain Decomposition (FDD), and the frequency response function is plotted in Figure 3.16 showing the frequencies that excite first, second and third modes of vibration at 12.5 Hz, 16.25 Hz, and 23.75 Hz respectively. The accelerometer values were converted into displacement values based on Newmark method by double integration, and using boundary conditions for two different accelerometers.

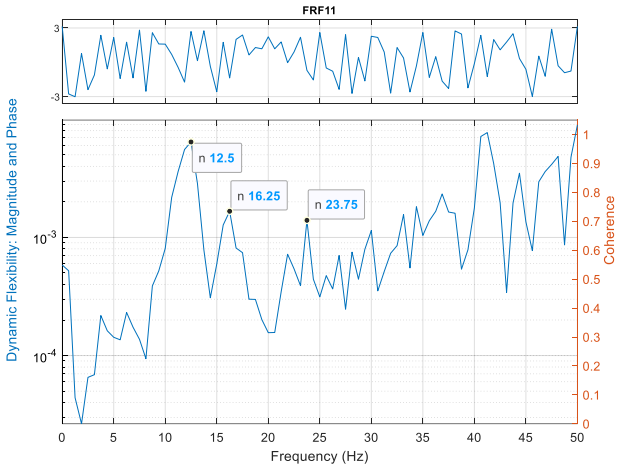


Figure 3.16: Frequency Response Function to obtain natural frequency

The data shown in Figure 3.15 was then filtered off at 25 Hz. using a Chevy Chev type II zero-phase filter in MATLAB to remove noise. Figure 3.17 shows the displacement data after filtering. This resulted in a better exponential fit as shown in Figure 3.18 with $R^2$=0.99. The amplitude decay and the damping were then estimated using this method, the exponential power $\delta_s$, (referred to as decrement in the equation) was obtained as 0.2173, and then damping coefficient $\zeta_s$ is calculated using the formula shown in Equation 3 as 0.0346 (or 3.46%).

$$\zeta_s = \frac{1}{\sqrt{1+\left(\frac{2\pi}{\delta_s}\right)^2}} \tag{3}$$

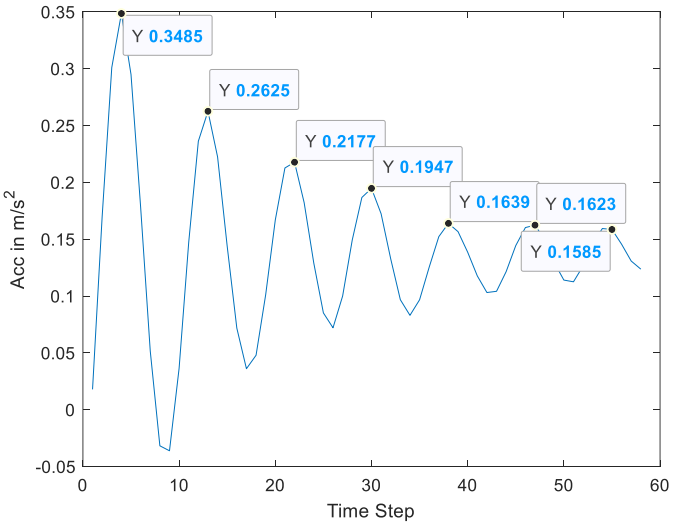


Figure 3.17: Acceleration time-history

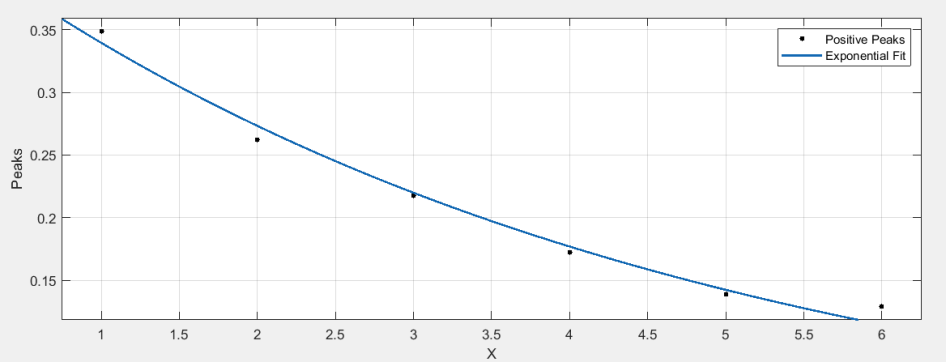


Figure 3.18: Exponential fit of positive peaks

Logarithmic decrement of Aerodynamic damping, $\delta_a$ was then calculated by Eurocode, EN 1991-1-4 formula as shown in Equation 4.

$$\delta_a = \frac{c_f \rho b v_m}{2nm} \tag{4}$$

where $c_f$ is the force coefficient (assumed as pressure coefficient in this study, the value of 0.8 is assumed for closed case based on pressure contours), $\rho$ is the density of air (1.225 kg/m3), b is the width of the structure (0.61m. for operable window), $v_m$ is the mean velocity at window height (30.4 m/s, 34.2 m/s, and 40 m/s for all tested cases at top of the window), n is the natural frequency of mode for which damping is calculated (12.5 Hz) and m is the equivalent mass or mass per unit length of the operable window (156.2 kg/m, calculated based on mechanical properties of the glass). Based on these values, was calculated as 0.0070, 0.0079, and 0.0087, for wind speeds 30.4 m/s, 34.2 m/s and 40 m/s respectively. Equation 5 shows the relation between total decrement, $\delta_{tot}$ and structural and aerodynamic damping in the absence of damping due to special mitigation devices.

$$\delta_{tot} = \delta_s + \delta_a \tag{5}$$

The total decrement was calculated as 0.224, 0.225, and 0.226 for all tested wind speeds, and corresponding total damping is found as 3.57%, 3.59%, and 3.60%.

Figure 3.19 shows an example of the time history of two accelerometers for Phase I and the data was stationary with fluctuating component around a mean acceleration. The RMS values of these accelerometers with respect to wind speed and wind direction were shown in Figure 3.20. Based on the RMS values, it was observed that the windward side ($0^0$) fluctuates less than crosswind ($90^0$ and $270^0$) and oblique angles especially at the center of the window.

The time history values were then converted into the frequency domain and the first two noticeable spikes were observed at 4.3 Hz. and 13.3 Hz. respectively in Figure 3.22. Based on the theory of background and resonance spectrum shown in Figure 3.23, it was concluded that the natural frequency of the first and second mode of the tested specimen was 4.3 Hz and ~13 Hz. in closed window condition. To understand the stable and unstable frequencies in the response spectrum, the system identification method of Complex Mode Indicator Function or CMIF (explained in Brickner et al., 2000) was used. Although such system identification methods were typically used for free vibration results, for the current study it helped to observe stable frequencies for a wind excited response. A stabilization diagram was then plotted based on the FDD method as shown in Figure 3.21 and it was concluded that 4.3 Hz, 13 Hz, and 16 Hz were the first three modes as they showed relatively long stable lines.

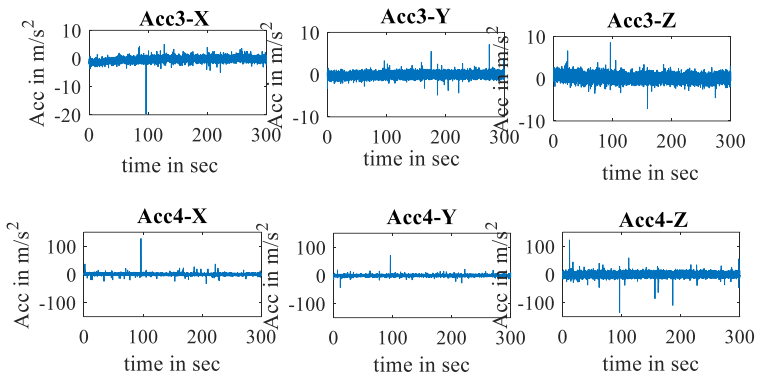


Figure 3.19: Acceleration time-history comparison between corner and center of the glass

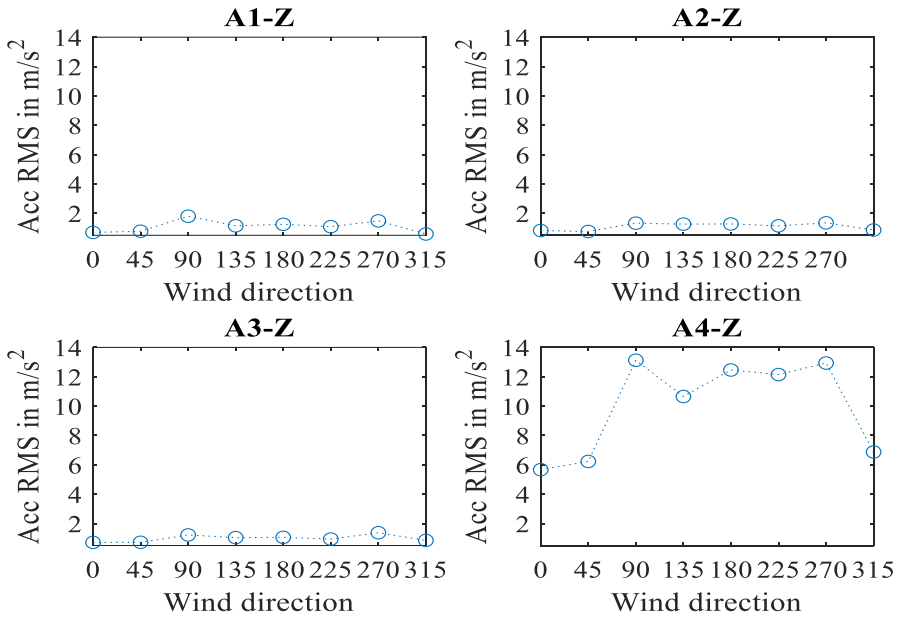


Figure 3.20: Effect of wind direction on RMS

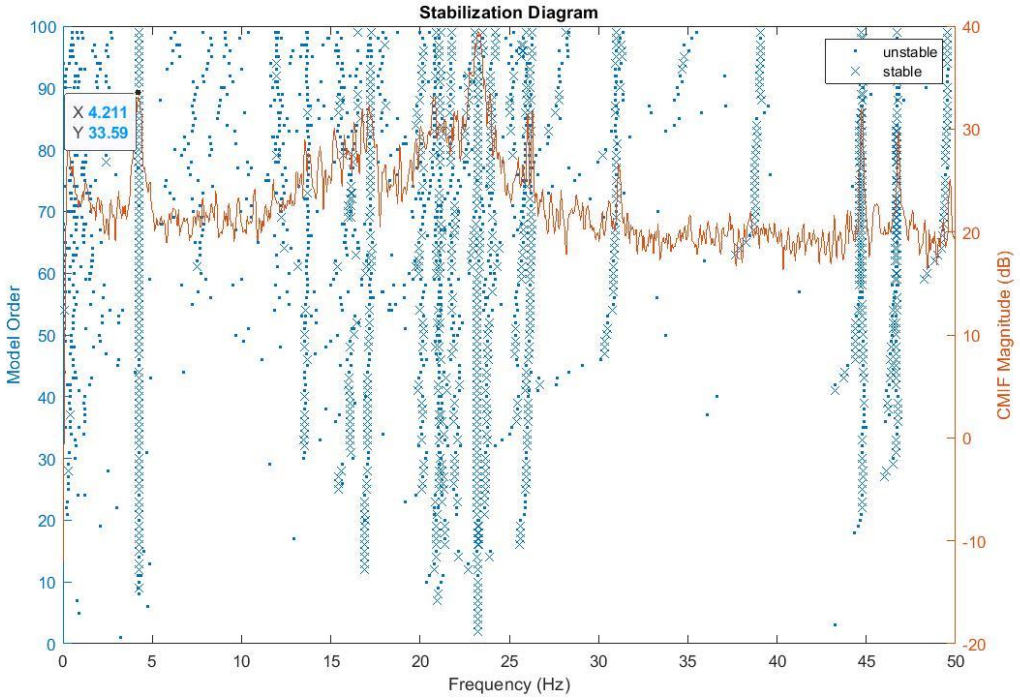


Figure 3.21: Stabilization diagram to obtain stable and unstable frequencies

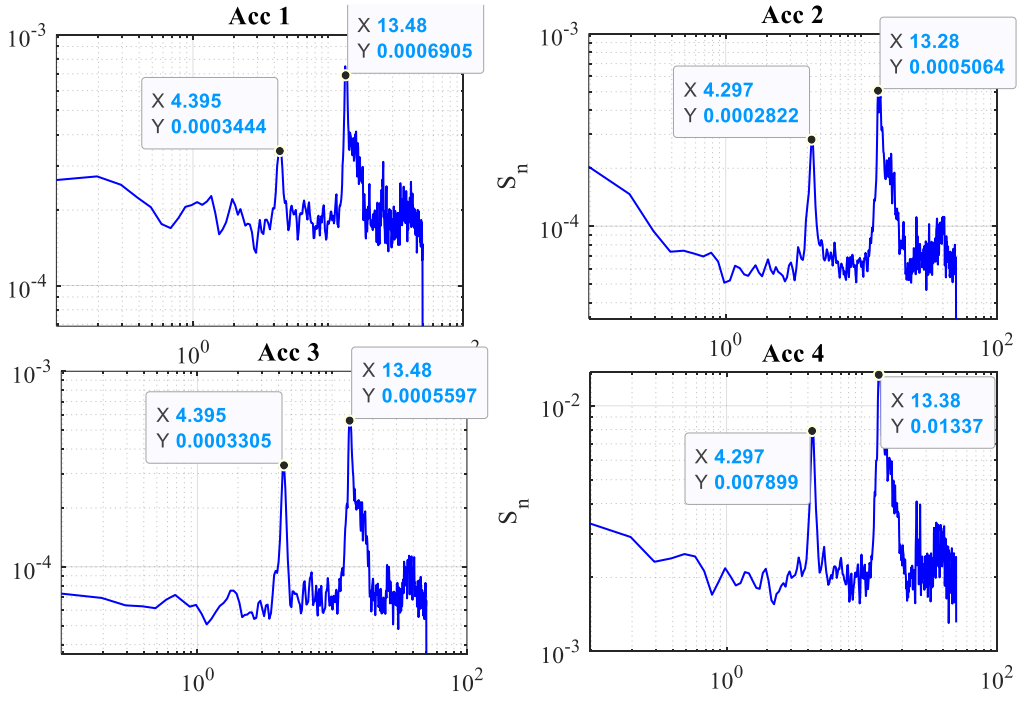


Figure 3.22: Power Spectral Density plots using pwelch

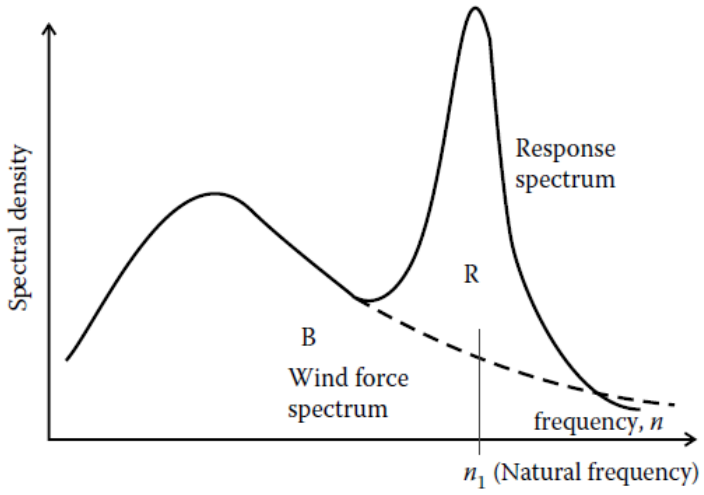


Figure 3.23: Typical background (wind spectrum) and resonant response (due to resonance)

Based on the FEM model developed in MIDAS, it was observed that the 4.2 Hz spike was that of the supporting structure as shown in Figure 3.24 and hence this spike was eliminated, and 12.5 Hz spike was observed to be the natural frequency of the window system, which agrees with the free vibration results.

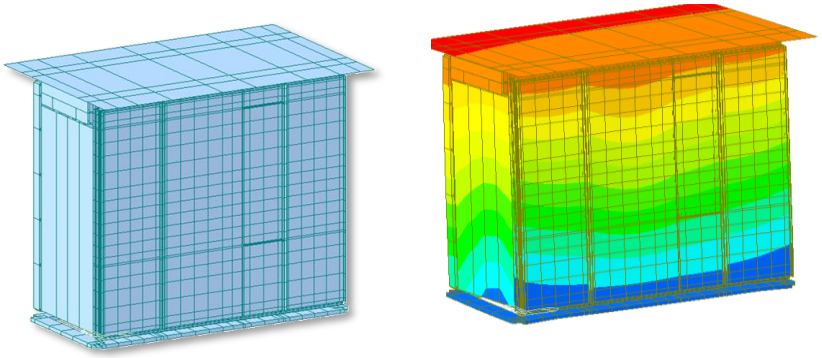

Figure 3.24: Full structure FEM and first mode

Based on the frequency domain analysis, the need to incorporate dynamic effects into the design of glass was apparent. For this purpose, Dynamic Amplification Factors (DAF) could be used to multiply the acceleration values obtained from the quasi-steady

design. The procedure to obtain DAFs for non-synoptic winds is discussed in Elawady et al. (2017) and a similar concept was applied for synoptic winds in this study by filtering the resonant component and converting the background quasi-static response into the time domain.

$$DAF = \frac{Maximum\ Peak\ Response}{Maximum\ Quasi\ static\ Response} \quad (6)$$

Table 3 shows the DAF values obtained for accelerometer 4 (located at the center of the glass window) for all three tested wind speeds and all the wind directions.

Table 3: Acceleration DAF values for window glass

| Wind Speed/Wind Direction | 35.76 m/s | 40.23 m/s | 44.6 m/s |
|---|---|---|---|
| 0 | 1.01 | 1.14 | 1.10 |
| 45 | 1.29 | 1.31 | 1.19 |
| 90 | 1.38 | 1.08 | 1.29 |
| 135 | 1.52 | 1.62 | 1.15 |
| 180 | 1.09 | 1.01 | 1.07 |
| 225 | 1.19 | 1.23 | 1.26 |
| 270 | 1.16 | 1.17 | 1.18 |
| 315 | 1.08 | 1.14 | 1.26 |

Although the highest DAF value obtained was 1.62 for oblique angle, based on typical design assumptions, solving windward side dynamic effects was assumed to provide a conservative design. Assuming a linear relationship between force and acceleration (based on quasi-static assumption and without considering dynamics), these acceleration DAF values were assumed as force DAFs. Hence from a structural design perspective, the DAFs were converted into velocity DAFs by simply taking square root (since the pressure/force is directly proportional to the square of wind velocity) of these

values. Hence for the safe design, it could be assumed that the design velocity values be multiplied by √1.14 or 1.068.

For phase I, and phase II the results from bi-axial strain gauges on the glass were analyzed by plotting time histories, these results would be utilized to validate a finite element model being developed by another team at FIU.

### 3.3 Analytical model and window resistance

Figure 3.25 shows the zoomed-in version (near-natural frequency of 13 Hz.) of the non-dimensional spectrum of three tested velocities and the peak magnitude increased with increasing wind speed, making the window more vulnerable for higher wind speeds. Based on the resonance theory explained in Figure 3.23, the experimental response spectra results could be split into background wind spectrum and resonant spectrum components. Wind engineering researchers (eg. Zhou and Kareem, (2003), Holmes, (2015), Moravej et al., (2015)) explained Aerodynamic Admittance Function (AAF) could be used to convert pressure measurements into load measurements and Mechanical Admittance Function (MAF) could be used to convert load measurements into response measurements in the frequency domain. Figure 3.26 shows typical AAF and MAF, and it can be observed that for low frequencies (before resonance), wind gust spectral density, force spectral density, and response spectral density are constant or AAF value is 1 and MAF value is 1. Therefore, the missing low-frequency range in the wind gust spectral density shown in Figure 3.1 and consequently, missing low frequency in the response spectral density (of accelerometers) could be theoretically matched with the Von-Karman spectrum by a transfer function, $|T(f)|^2$ obtained by dividing obtained spectral density value, $S_{u,RS}(f)$

with the target Von-Karman spectral density value, $S_{u,WS}(f)$ as shown in Equation 7. In addition, the MAF was already captured in the experiments which could be seen from the spikes in Figure 3.22. Based on this theory, an analytical model was developed. First MAF was numerically calculated based on the formula by Moravej et al. (2015) as shown in Equation 8.

$$|T(f)|^2 = \frac{S_{u,RS}(f)}{S_{u,WS}(f)} \tag{7}$$

$$|H(f)|^2 = \frac{1}{\left[1-\left(\frac{f}{f_{01}}\right)^2\right]^2 + 4\zeta^2\left(\frac{f}{f_0}\right)^2} \tag{8}$$

where $f_{01}$=13.3 Hz; Frequency for the first mode and $\zeta$ is the damping ratio assumed to be 3.6% based on free vibration tests. As an extension of this theory, for more than one modal frequencies (eg. n frequencies), total MAF can be calculated as shown in Equation 9.

$$|H(f)|^2 = |H_1(f)|^2 * |H_2(f)|^2 * \ldots\ldots * |H_n(f)|^2 \tag{9}$$

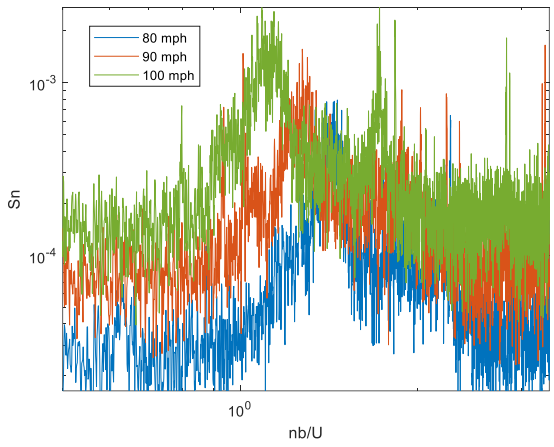


Figure 3.25: Experimental Non-dimensional (only frequency) PSD showing the effect of wind speed

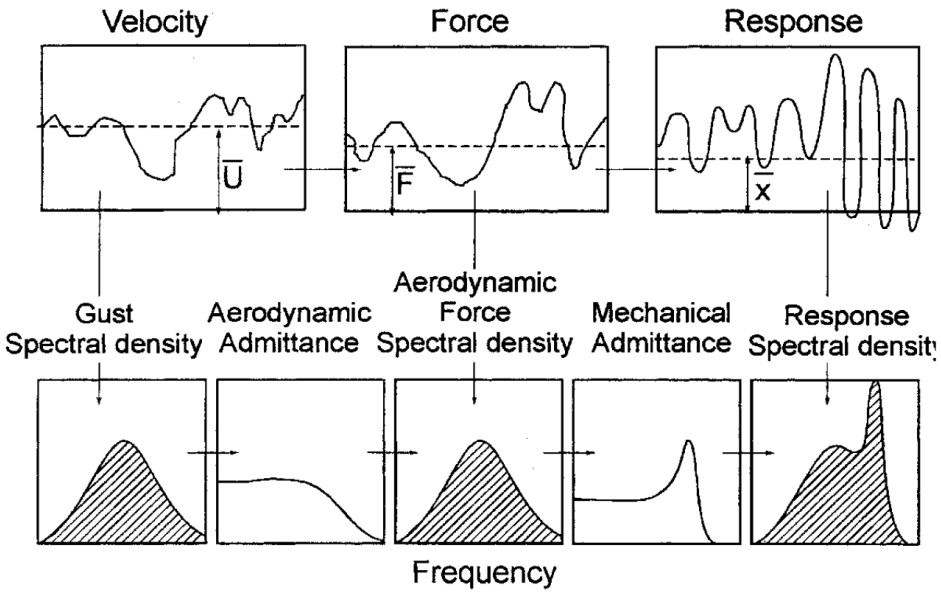


Figure 3.26: Time and frequency domain of typical data (Holmes, 2015)

Hence by using the transfer function shown in Figure 3.27, the missing low-frequency components of the response can be theoretically added to the acceleration spectrum. The MAF value as shown in Figure 3.28 thus calculated was then overlapped over the wind speed spectrum to obtain the response spectrum. The spectrum thus obtained was compared with the non-dimensional spectrum obtained from the experiments to validate the analytical model at the resonance part. Figure 3.29 shows the match between the response spectrum in the resonance zone. An analytical model was then developed based on the theory of background and resonant response. The calculated MAF values are overlapped on the background wind spectrum values (after TF application) and are compared with the PSD of the response spectrum as shown in Figure 3.29.

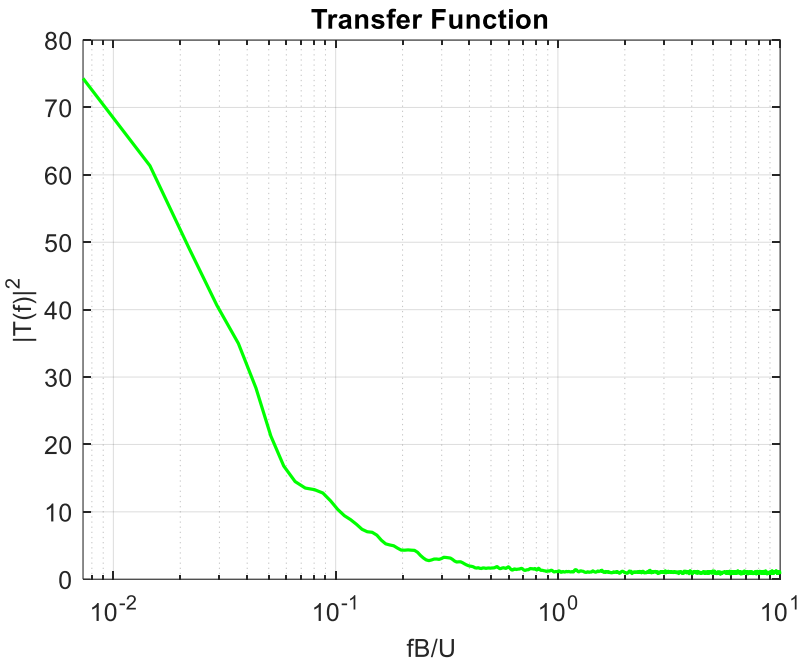


Figure 3.27: Transfer function to account for missing low frequency in response spectrum

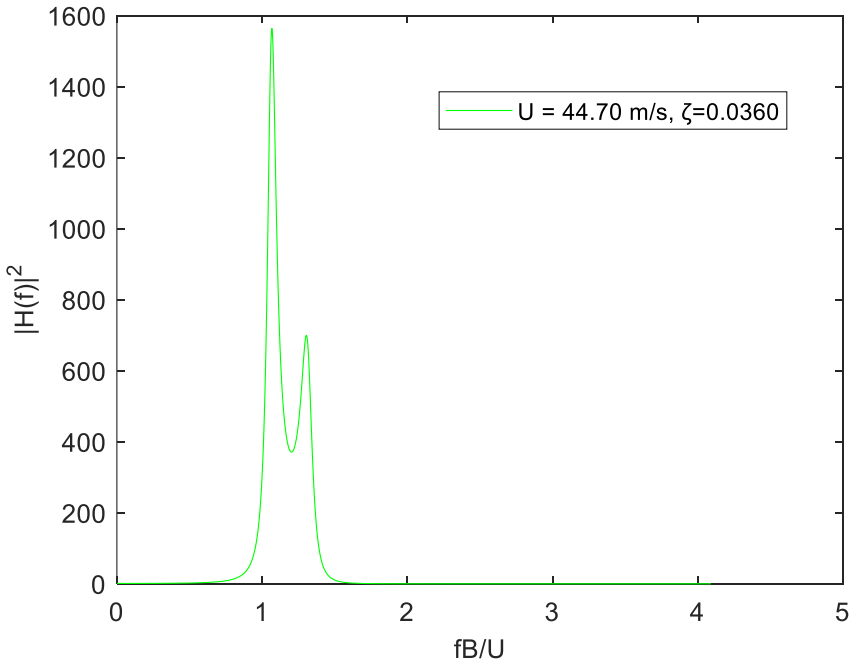


Figure 3.28: MAF showing resonance component for first two modes, 13.3 Hz and 16.1 Hz

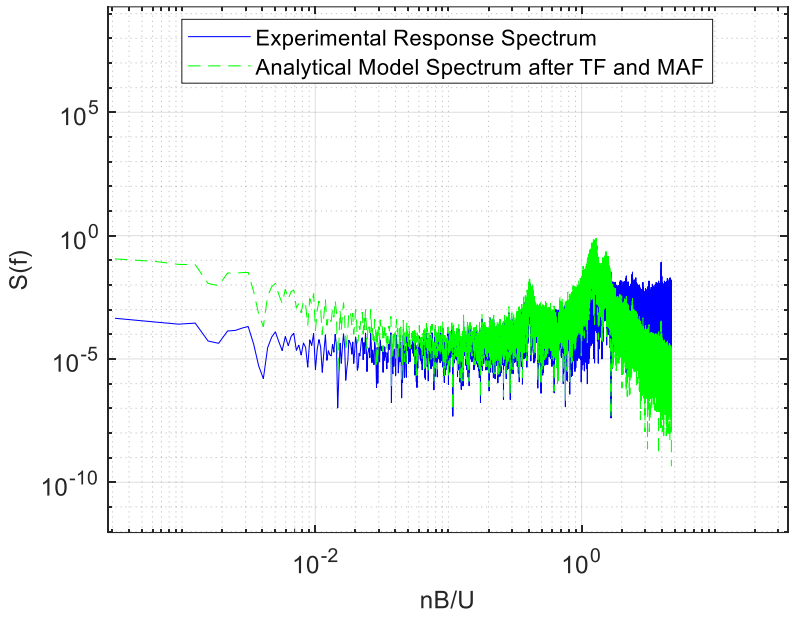


Figure 3.29: Analytical model with compensated low frequency and predicted dynamic response match at 44.7 m/s

The results from the current study were utilized to develop possible code guidelines for such dynamically sensitive components. First, based on the developed analytical model and the well-known fact that area under PSD of response in the frequency domain is equal to the square of standard deviation (variance) of the response in the time domain, gust response factor (shown in Equation 10 to convert mean response to peak response for a random process variable, x) was obtained as shown in Equations 11 to 13.

$$\hat{x} = \bar{x} + g\sigma_x \tag{10}$$

where $\hat{x}$ is the peak response; $\bar{x}$ is the mean/quasi-steady response and $\sigma_x$ is the RMS over the mean of x.

$$\boldsymbol{S}_{Resonance}(\boldsymbol{f}) = \boldsymbol{S}_{Response}(\boldsymbol{f})/\boldsymbol{S}_{aerodynamic}(\boldsymbol{f}) \tag{11}$$

where $\boldsymbol{S}_{Resonance}(\boldsymbol{f})$, $\boldsymbol{S}_{Response}(\boldsymbol{f})$ and $\boldsymbol{S}_{aerodynamic}(\boldsymbol{f})$ are the resonant, total, and wind gust spectra respectively in the frequency domain or

$$\sigma_{Resonance}=\sqrt{\left(\sigma_{Response}\right)^2-\left(\sigma_{background}\right)^2} \quad (12)$$

=1.01 from the PSD of MAF

$\sigma_{Background}$=1.29 from the filtered PSD used for calculation of DAF

$$Response_{peak}=Response_{mean}+\sqrt{(g_B x\sigma_{Background})^2+(g_R x\sigma_{Resonance})^2} \quad (13)$$

$Response_{peak}$-$Response_{mean}$=6.08

$g_R$ was obtained from the above equation, $g_B$=3.4 from ASCE 7-16

So, $6.08^2=(g_B x\sigma_{Background})^2+(g_R x\sigma_{Resonance})^2$

or $g_R$=4.71.

The buffeting force (to obtain the peak response of ) can then be calculated by multiplying the Gust-effect factor(G) provided in ASCE 7-16, 26.11.5 (for dynamically sensitive buildings)

Resonant response factor($g_R$), based on the natural frequency n1 was calculated using ASCE 7-16 as shown in Equation 14

$$g_R=\sqrt{2\ln(3600n1)}+\frac{0.577}{\sqrt{2\ln(3600n1)}} \quad (14)$$

The gust response factor was calculated as 4.767, assuming a natural frquency of 13.3 Hz., vs a calculated value of 4.71 with an error of 1.2%.

### 3.4 Destructive Testing and hardware vulnerability

In addition to vibration and WDR tests, the destructive testing was also performed with WOW throttle ratios at the windward side ($0^0$) starting from 46.5 % (corresponding to 31.3 m/s at roof height) to 100% (67 m/s) with increments of 5%, for 30 sec per wind speed, to observe any structural failure keeping the windows open. The failure occurred at 96.5% (~58.1 m/s) and the window configuration was changed to a closed position pertaining to the yielded hardware hinge (on which accelerometer 4 was located, in phase II) failure. Figure 3.30 shows the failed hardware component of the window. This test signifies the importance of better hardware codes and standards for better structural performance of operable window systems for wind. Current codes do not emphasize the hardware design and there is no fixed procedure to check the hardware design strength and vulnerability. The results from the accelerometers and strains from phase II testing were shown in Figure 3.31, Figure 3.32, and Figure 3.33. These clearly show a dynamic amplification of the hardware component (based on the PSD plot, only accelerometer 4 shows the dynamic effect and this was the yielded hinge during destructive testing).

Figure 3.30: Yielded connection hinge

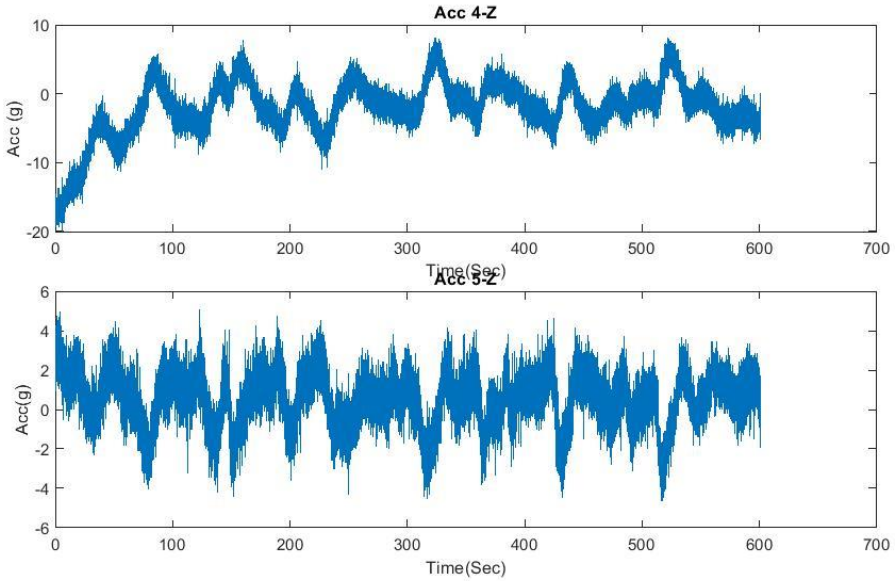


Figure 3.31: Accelerometers on the hardware showing cyclic accelerations

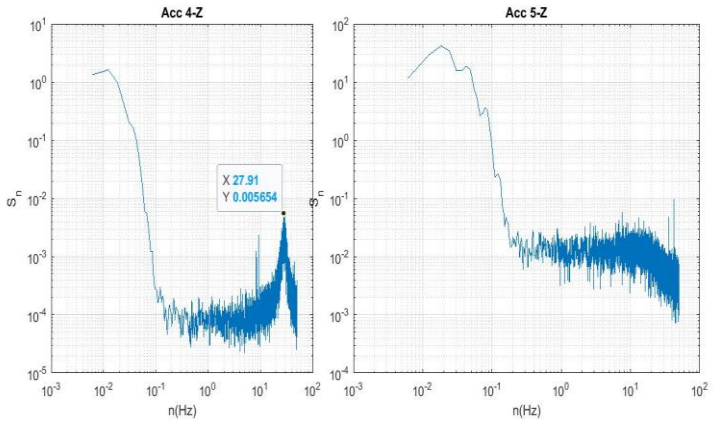


Figure 3.32: PSD of accelerations on the hinges

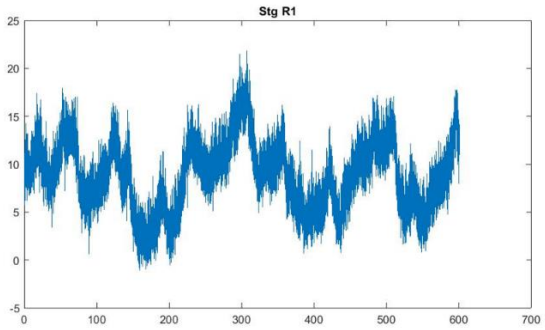


Figure 3.33: Strain on the failed hinge

Based on the performed experiments and from code provisions for resistance of hardware components, a vulnerability framework was developed to obtain the probability of failure for corresponding wind speeds. For this, a review of existing loss models, FPHLM and FEMA Hazus was performed, and it was noted that the existing loss models consider the extreme load values as normal distribution (or bell curve). However, ASCE 7-16 assumes that the peak wind pressure/wind load typically follows Fisher Tippet Distribution Type I (with long left heads and short right tails in probability density functions). Hence, for this study, the realistic load data obtained from wind tunnel was compared to the resistance values from BS EN 12217:2003. Based on Monte Carlo

simulations for 1000 trials, randomized damage distribution is obtained, and from this damage distribution, a mean value was taken for each wind speed to plot the vulnerability curve. It is important to note that this procedure is valid as the comparison of destructive tests was made with the vulnerability curves obtained from WOW pressure data. To expand this to a field comparison, further estimation of peaks is warranted based on the existing literature(for eg. Sadek and Simiu (2002), Peng et al. (2014)) to estimate the peaks for a time duration of interest. The damage function pdf, typical vulnerability curve methodology and the obtained vulnerability curve is shown in Figure 3.34, Figure 3.35, and Figure 3.36 respectively.

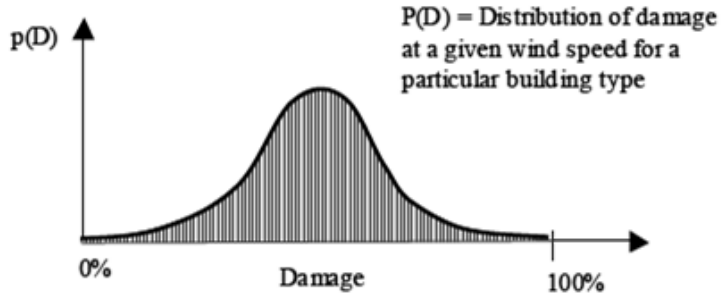


Figure 3.34: Typical pdf example of damage function

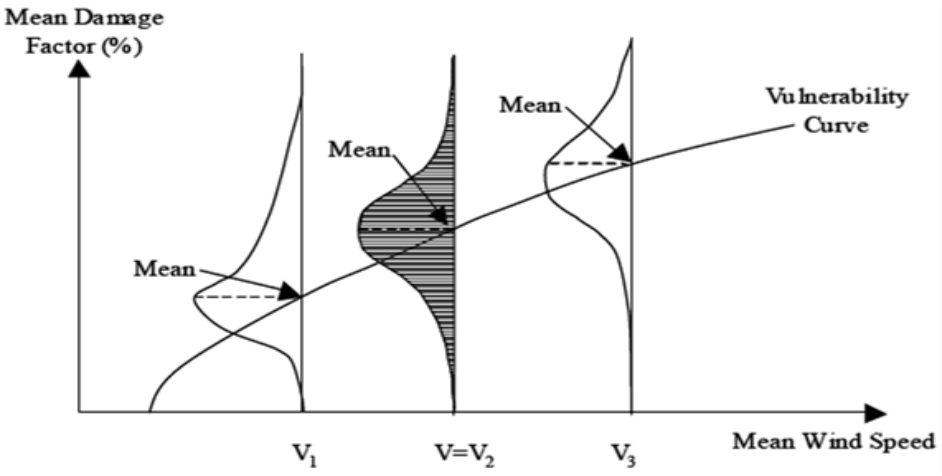


Figure 3.35: Methodology to calculate vulnerability curve encompassing various wind speeds

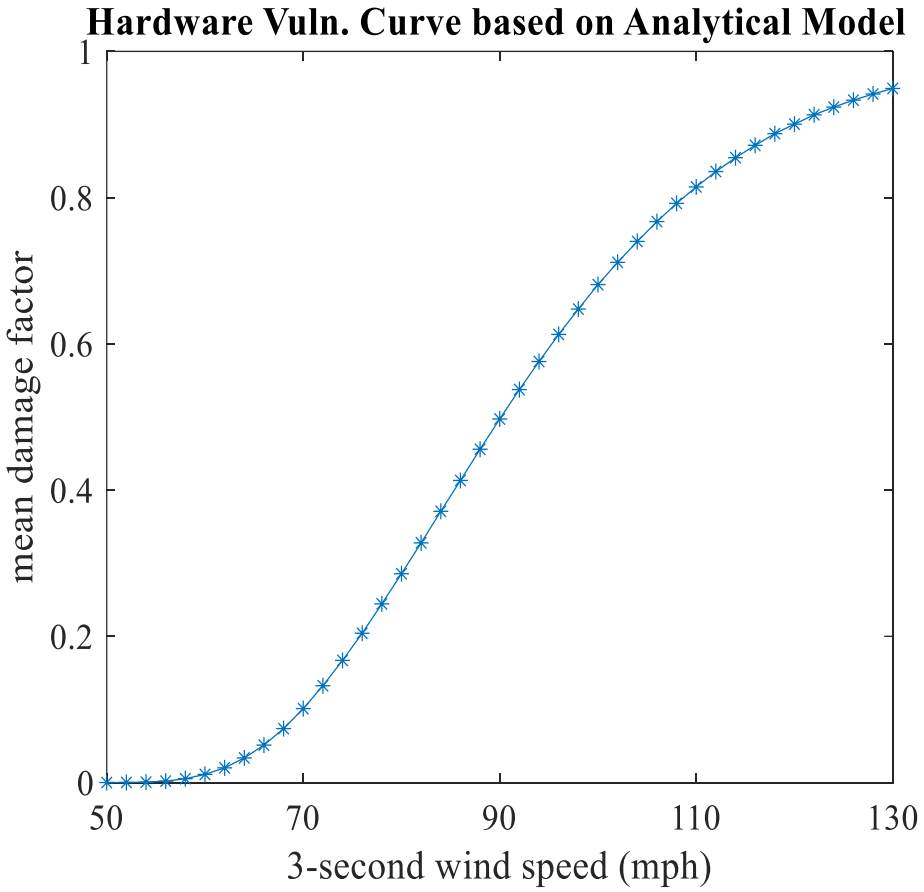


Figure 3.36: Hardware failure probability curve

Based on the vulnerability framework developed, a probability of 95% failure was expected at 130 mph which is close to the failure at 135 mph wind speed based on destructive testing. In addition, fatigue behavior (based on the time history plots) was observed. Hence a fatigue analysis would be needed for cyclic stress calculation (similar to the procedure in EN 1991-1-3) and the load that the hardware component can withstand based on ultimate strength could be obtained from load transfer calculations based on the Cp contour. This calls for future research to design a stronger connection member which could better resist fatigue.

### 3.5 Towards codification and Design suggestions

It is important to note that the structural damping has higher contribution in comparison to aerodynamic damping based on the experimental tests performed for the curtainwall window systems. So, for a typical window, based structural damping can be obtained based on the Finite Element modeling of the curtainwall window and the aerodynamic damping can be assumed to be negligible. From a design perspective, three methods were compared for the appropriate Gust effect factor, $G_f$:

1) Static Approach (current design approach) for rigid structures: $G_f = 0.85$
2) From DAF approach: Based on the basic theory, peak can be calculated as

   $Response_{peak} = Response_{mean} +$

   $\sqrt{Response_{peakBackground}{}^2 + Response_{peakResonance}{}^2}$ and

   $Wind\ tunnel\ G'_f = DAF\left(1 + \frac{\widehat{x_B}}{\bar{x}}\right)$ (Azzi et al. 2021)

   However, it is important to note that for direct ASCE 7 standard comparisons, the conversion of this $G'_f$ full-scale can be converted to $G_f$ 3-sec gust by

$$G_f = \frac{G'_f}{\left(\frac{V_{3-s}}{V_{15-min}}\right)^2}$$

3) Dynamic Approach(suggested approach) for flexible structures:

   In brief, this approach is based on gust resonant factor and incorporating the resonant effects into Gust effect factor. Refer to ASCE 7-16 for all the notations.

$$G_f = 0.925\left(\frac{1 + 1.7I_{\bar{z}}\sqrt{g_Q^2 Q^2 + g_R^2 R^2}}{1 + 1.7g_v I_{\bar{z}}}\right)$$

$$Q = \sqrt{\frac{1}{1 + 0.63\left(\frac{B+h}{L_{\bar{z}}}\right)^{0.63}}}$$

$$g_R = \sqrt{2\ln(3{,}600n_1)} + \frac{0.577}{\sqrt{2\ln(3{,}600n_1)}}$$

$$R_n = \frac{7.47N_1}{(1 + 10.3N_1)^{5/3}} \qquad N_1 = \frac{n_1 L_{\bar{z}}}{\bar{V}_{\bar{z}}}$$

$$R = \sqrt{\frac{1}{\beta} R_n R_h R_B (0.53 + 0.47R_L)}$$

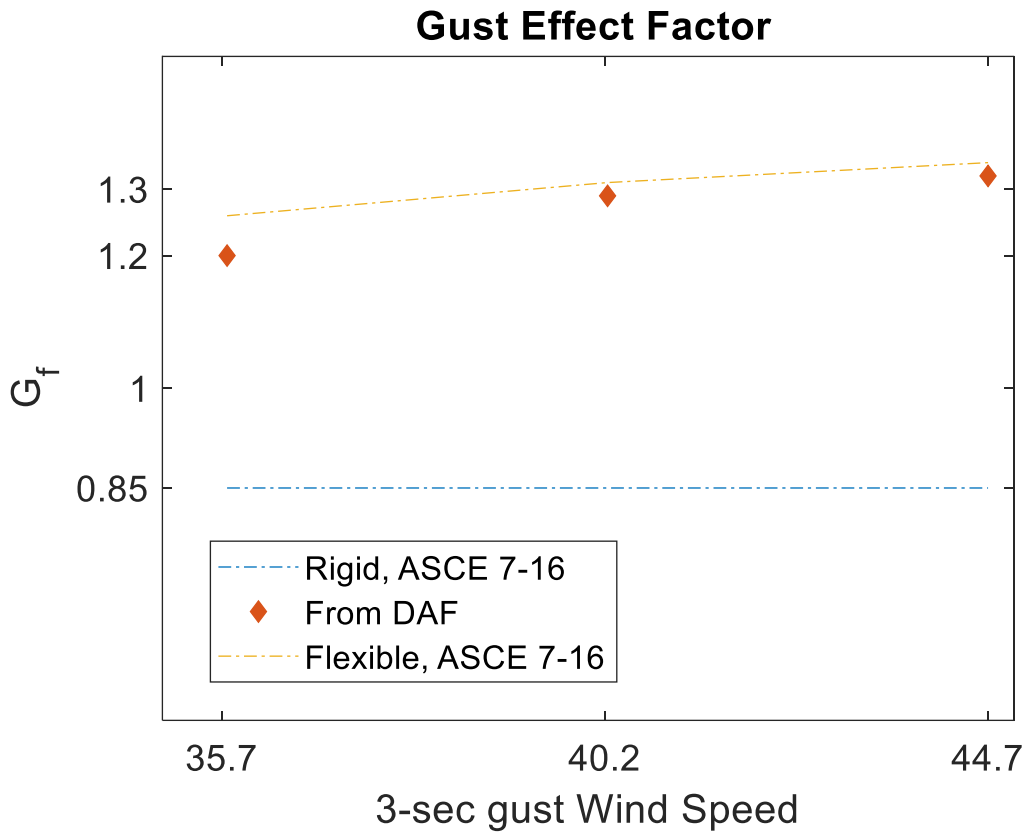


Figure 3.37: Comparison of Gust Effect Factors from various approaches

Based on the comparison shown in Figure 3.37, it is advised that for design of dynamically sensitive components such as curtainwall window systems, a dynamic approach of ASCE 7-16 would yield conservative results. After obtaining the Gust Effect Factor (G) from ASCE 7-16, two different approaches as shown in Figure 3.38 were proposed to incorporate the dynamic effects into a typical curtainwall window design.

**Approach I**

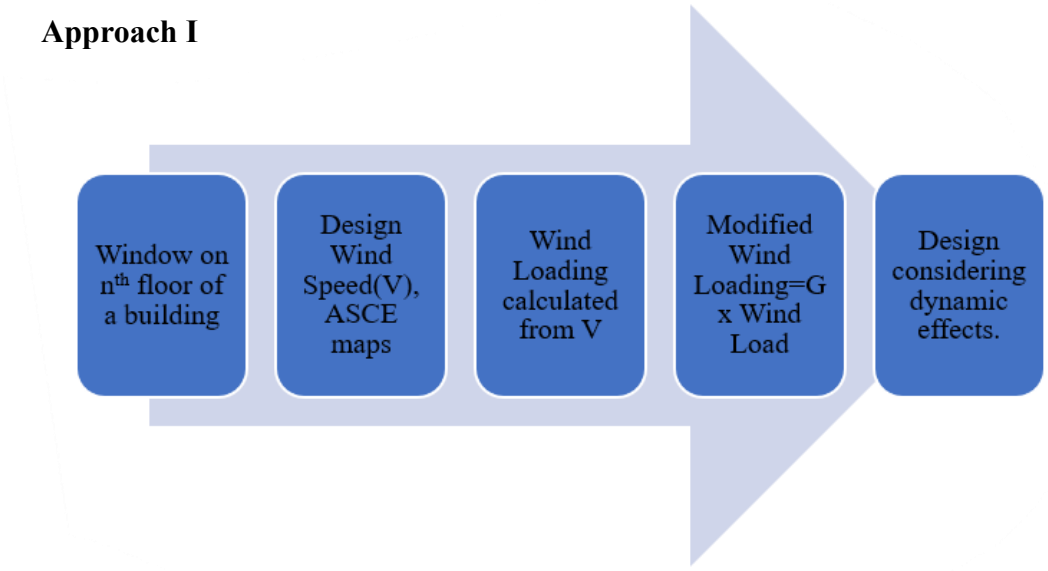


**Approach II**

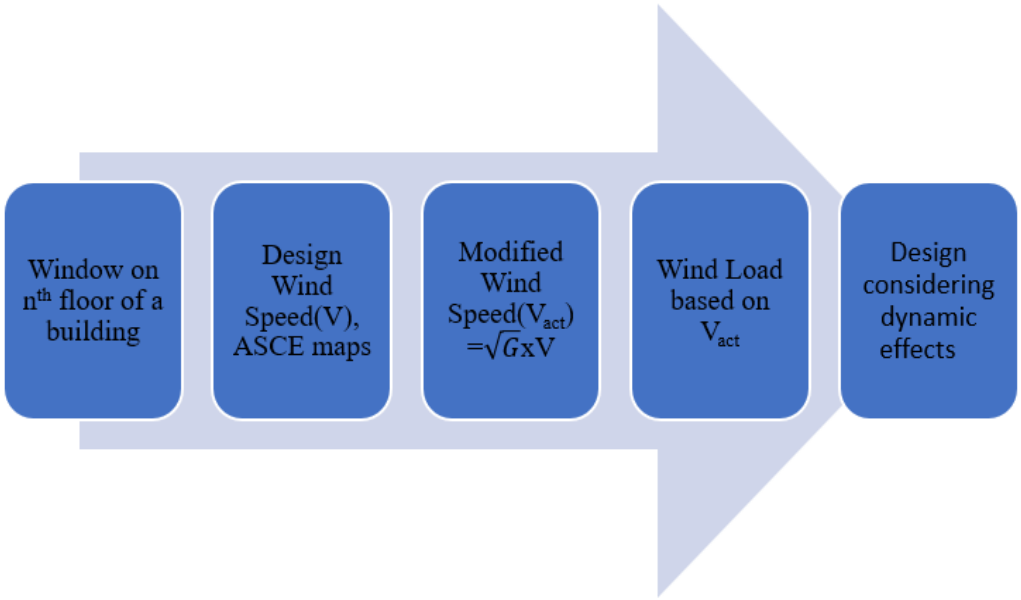


Figure 3.38: Flow chart showing two suggested design approaches for industry

## 3.6 Chapter 3 references


Asghari Mooneghi, M., Irwin, P., Gan Chowdhury, A., 2016. Partial turbulence simulation method for predicting peak wind loads on small structures and building appurtenances. Journal of Wind Engineering and Industrial Aerodynamics 157, 47–62. https://doi.org/10.1016/j.jweia.2016.08.003

Asmussen, J.C., 1997. Modal analysis based on the random decrement technique. Department of Mechanical Engineering, Aalborg University.

Azzi, Z., Elawady, A., Irwin, P., Chowdhury, A. G., & Abi Shdid, C. (2021). Aeroelastic modeling to study the wind-induced response of a self-supported lattice tower. Engineering Structures, 245, 112885.

Brincker, R., 1995. Note about the Random Decrement Technique. Aalborg University.

Chopra, A.K., 2017. Dynamics of Structures, 5th Edition, Pearson publications.

Chowdhury, A.G., Sarkar, P.P., 2003. A new technique for identification of eighteen flutter derivatives using a three-degree-of-freedom section model. Engineering Structures 25, 1763–1772.

Elawady, A., Aboshosha, H., El Damatty, A., Bitsuamlak, G., Hangan, H., & Elatar, A. (2017). Aero-elastic testing of multi-spanned transmission line subjected to downbursts. Journal of Wind Engineering and Industrial Aerodynamics, 169, 194-216.

ESDU 85020: Atmospheric turbulence near ground: data for winds.

Goldstein, H., 1989. Restricted unbiased iterative generalized least-squares estimation. Biometrika 76, 622–623.

Holmes, J.D., 2015. Wind Loading of Structures, 3rd ed. CRC Press, Boca Raton. https://doi.org/10.1201/b18029

Ibrahim, S.R., Mikulcik, E.C., 1977. A method for the direct identification of vibration parameters from the free response. The shock and vibration bulletin 97.

Irwin, H., Cooper, K.R., Girard, R., 1979. Correction of distortion effects caused by tubing systems in measurements of fluctuating pressures. Journal of Wind Engineering and Industrial Aerodynamics 5, 93–107.

Lieblein, J., 1976. Efficient methods of extreme-value methodology. Technical Analysis Div., Institute for Applied Technology, National Bureau: of Standards, report no. NEA-CSNI-R--1976-10.

Moravej, M., 2018. Investigating scale effects on analytical methods of predicting peak wind loads on buildings. Ph.D. dissertation, Florida International University.

Moravej, M., Chowdhury, A.G., Irwin, P., Zisis, I., Bitsuamlak, G., 2015. Dynamic effects of wind loading on photovoltaic systems, in: 14th. International Conference on Wind Engineering (ICWE14), Porto Alegre, Brazil.

Olmos, B.A., Roesset, J.M., 2010. Evaluation of the half-power bandwidth method to estimate damping in systems without real modes. Earthquake engineering & structural dynamics 39, 1671–1686.

Peng, X., Yang, L., Gavanski, E., Gurley, K., & Prevatt, D. (2014). A comparison of methods to estimate peak wind loads on buildings. Journal of wind engineering and industrial aerodynamics, 126, 11-23.

Perl, W., 1960. A method for curve-fitting by exponential functions. The International Journal of Applied Radiation and Isotopes 8, 211–222.

Rodrigues, J., Brincker, P., 2005. Application of the random decrement technique in operational modal analysis. In Proceedings of the 1st International Operational Modal Analysis Conference, April 26-27, 2005, Copenhagen, Denmark (pp. 191-200). Aalborg Universitet.

Sadek, F., & Simiu, E. (2002). Peak non-Gaussian wind effects for database-assisted low-rise building design. Journal of Engineering Mechanics, 128(5), 530-539.

Vandiver, J.K., Dunwoody, A.B., Campbell, R.B., Cook, M.F., 1982. A mathematical basis for the random decrement vibration signature analysis technique. ASME Journal of Mechanical Design, 307-313.

Zhou, Y., Kareem, A., 2003. Aerodynamic Admittance Function of Tall Buildings. Nat Haz modeling laboratory technical report.

# 4. SIMULATION OF FULL-SCALE RAINDROP SIZE DISTRIBUTION AND TESTS TO QUANTIFY WATER INTRUSION INTO THE OPERABLE WINDOW

## 4.1 Rain intrusion into the built environment

Recent hurricane damage surveys (e.g. Pinelli et al. (2018) and Kijewski-Correa et al. (2021)) after Hurricane Irma, Michael, Florence, Harvey, Dorian, Laura, highlighted the importance to study rain intrusion. Recent post-storm damage surveys showed that most losses were due to interior content damage, which was caused mostly by rain intrusion. The wind-driven-rain (WDR) effects on building façades were well recognized in the literature ( e.g. Choi (1999), Straube and Burnett (2000), Blocken and Carmeliet (2004), Salzano et al., (2010), Kubilay et al., (2014), Vutukuru et al. (2020)), and is especially important because potential mold and mildew growth may result in deterioration, serviceability disruptions, and interior content damage. Even during normal weather conditions, condensation deposition affects the performance of the building by affecting the overall Heat, Air, and Moisture (HAM) transfer phenomenon and energy consumption (Blocken et al., 2007).

Aerodynamically, when the wind flows into a rectangular building, flow separation occurs at about two-thirds of the building height, and some air reaches up to the roof, some air flows sideways and around the corner, and the remaining air travels downward and may form a vortex (Wise et al. (1965)). This airflow pattern can be used as a wind-driven rain deposition guide. The rain deposition on a building is mainly dependent on oncoming wind velocity and raindrop size distribution (RSD). The amount of rain deposited on the

wall of a building is almost half of the amount of rain measured in free air (Robinson and Baker (1975)). Typically, due to the deflection of air and rain, the deposition of rain is higher on the top and sides of a building in comparison to the remaining surfaces. The water intrusion into a building can be attributed to pathways, sources, and driving forces (Baheru et al. (2014a), and Vutukuru et al. (2020)) as shown in Figure 4.1.

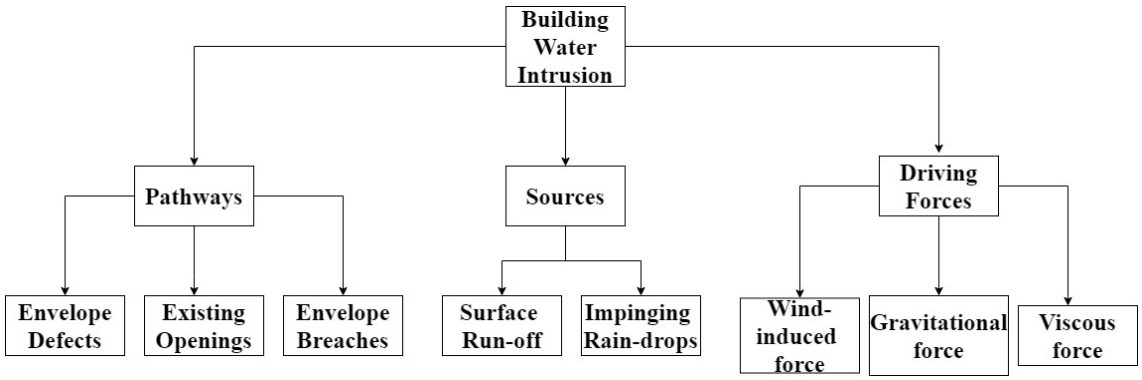


Figure 4.1:Attribute classification for rain intrusion into the building

Damage assessment studies published following the 2004 and 2005 Atlantic hurricane seasons identified several instances where significant losses to building interiors and contents directly resulted from water intrusion through various openings and breaches of the building envelope ((FEMA 490-2005); (FEMA 488-2005)). Following Hurricane Irma in 2017, damage observations in Florida demonstrated that soffit failures were a primary source of WDR-related water intrusion into attic spaces that led to interior damage; these observations prompted FEMA to publish a Recovery Advisory (RA) recommending more stringent soffit design and installation details (FEMA (2018)). Existing risk assessment models include FEMA-HAZUS (discussed in Subramanian et al. (2014)) and the Florida Public Hurricane Loss Model (FPHLM) (discussed in Baheru (2014)). However, the interior damage was treated as a function of the total volume of

water entering a building, which was calculated based on semi-empirical models with assumed WDR parameters and engineering judgment (Baheru (2014)). Due to a lack of quantitative data, there is a possibility of strong uncertainty in the estimated water volume in these semi-empirical methods.

### 4.2 Literature Review and Target RSD parameters

The complex rain intrusion into building phenomenon is governed mainly by the volume of water in the oncoming air and the water deposition on the building surface. The current study focuses on simulating the correct RSD, defined as the concentration N(D) of droplets within a given raindrop diameter (D) range. The rain intrusion phenomenon depends on the oncoming wind and on the RSD, which are in turn mutually dependent, hence the accuracy of the test results both these factors need to be measured accurately.

The rain characteristics during hurricanes and tropical storms were studied by, Merceret (1974), Willis and Tattelman (1989), Tokay et al. (2008), (Lopez (2011). Efforts to characterize RSD date back to Marshall and Palmer (1948), who tried to develop a model depending on the rain rate shown in Equation 1 for raindrops greater than 1.5 mm.

$$N(D) = N_0 e^{-\wedge D} \quad (1)$$

where D is the diameter, N(D)δD is the number of raindrops between D and D+δD, and the power parameter depends on rain rate as shown in Equation 2

$$\wedge = 41RR^{-0.21}\ cm^{-1} \quad (2)$$

RR in $mm^{-1}$ and ∧ was determined to be 0.08 $cm^{-1}$

Best (1950) developed the following empirical formula applicable to monsoon and thunderstorm rain:

$$F(x)= 1 - exp\left(-\left(\frac{x}{a}\right)^{n}\right) \quad (3)$$

where F(x) is the fraction of liquid water in the air, contained in drops with diameter less than x; a, and n are constants for a particular rainfall type, with a general relationship of an=7.1 mm for monsoon type rains (Kelkar (1961)).

Recent RSD characteristics include Verification of the Origins of Rotation in Tornadoes Experiment 2 (VORTEX2) project (discussed in (Rasmussen et al. (1994)) and the Florida Coastal Monitoring Program (FCMP) (discussed in (Lopez (2011)). In addition, during the active 2004 and 2005 hurricane seasons, tropical storm and hurricane characteristics were studied by the National Aeronautics and Space Administrations' Tropical Rainfall Measuring Mission (TRMM) ground validation program at Wallops Station, Wallops Island, VA. The rain characteristics were measured during Hurricanes Alex, Charley, and Gaston, which caused significant winds and heavy rainfall at the station (Lonfat et al., 2004). During these hurricanes, the concentration of mid-size drops was significantly higher, especially between 1mm and 2 mm. Based on this data, Tokay et al., (2008) concluded that a gamma model would accurately determine the RSD. Equation 4 shows the expression for the dimensionless gamma model.

$$\frac{N_D}{N_w} = f(m)\left(\frac{D}{D_{mass}}\right)^{m} \exp\left(-(4+m)\frac{D}{D_{mass}}\right) \quad (4)$$

where is the normalized RSD, D is the raindrop diameter, is the mass-weighted mean diameter, and m is the shape parameter, f(m) has an inbuilt gamma function (Γ) shown in Equation 5.

$$f(m) = \frac{6}{4^4}\frac{(m+4)^{m+4}}{\Gamma(m+4)} \quad (5)$$

The above equation is independent of rain rate and m defines the non-dimensional RSD spectrum. $N_w$ is required for converting the above equation into dimensional form and can be estimated using $D_{mass}$ and W (liquid water content), both of which depend on rain rate. Equation 6 shows the formula for calculating $N_w$. Figure 4.2 shows the step-by-step procedure to obtain dimensional RSD plots starting with the value of target rain rate and horizontal velocity (wind velocity) based on Baheru (2014).

$$N_w = \frac{4^4}{\pi\rho_w}\left(\frac{W}{{D_{masss}}^4}\right) \quad (6)$$

where $W=0.067RR^{0.895}$ and $D_{mass}=0.188RR^2+0.254RR+1.046$ and RR is the rain rate in mm/hr.

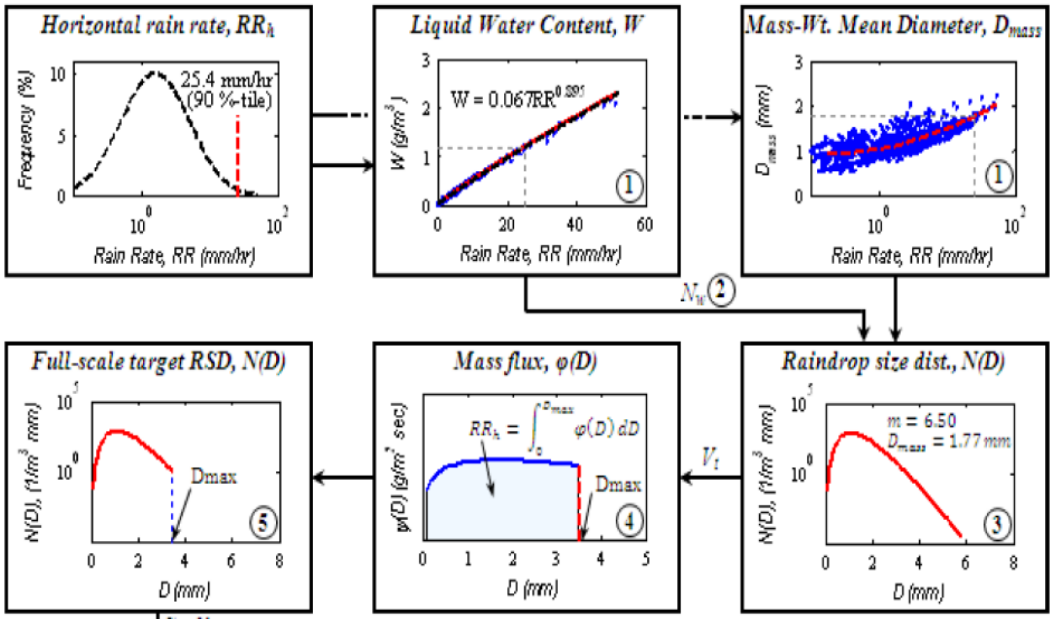


Figure 4.2: Full-scale RSD calculations (Baheru, 2014)

Target gamma models were developed for different rain rates by both Willis and Tattelman (1989) and Tokay et al. (2008) formulas. The target gamma model for this study would be Willis and Tattelman (1989), which is considered to be more reliable. Codes and standards shown in Table 1 typically use a rain rate of 22.3 cm/hr. (8.8 in/hr.) for testing. However this data is typically obtained from rain gauges and based on mean hourly data, and a study by Blocken and Carmeliet (2007) concluded that a time-varying 10-minute data might be more meaningful for structural testing purposes. Based on previous literature, and for Typhoon Mangkhut in China, the 10-min and 1-hr rain intensity data can be correlated as shown in Equation 7. This would give an $RR_{10\text{-min}}$ value of 21.3 in/hr. for a $RR_{1\text{-hr}}$ value of 8.8 in/hr. This is also validated based on previous research by Perica et al. (2018) for a mean recurrence interval of 500 years as shown in Figure 4.3.

$$RR_{10\text{-min}} = 2.481 \times RR_{1\text{-hr}}^{0.9817} \quad (7)$$

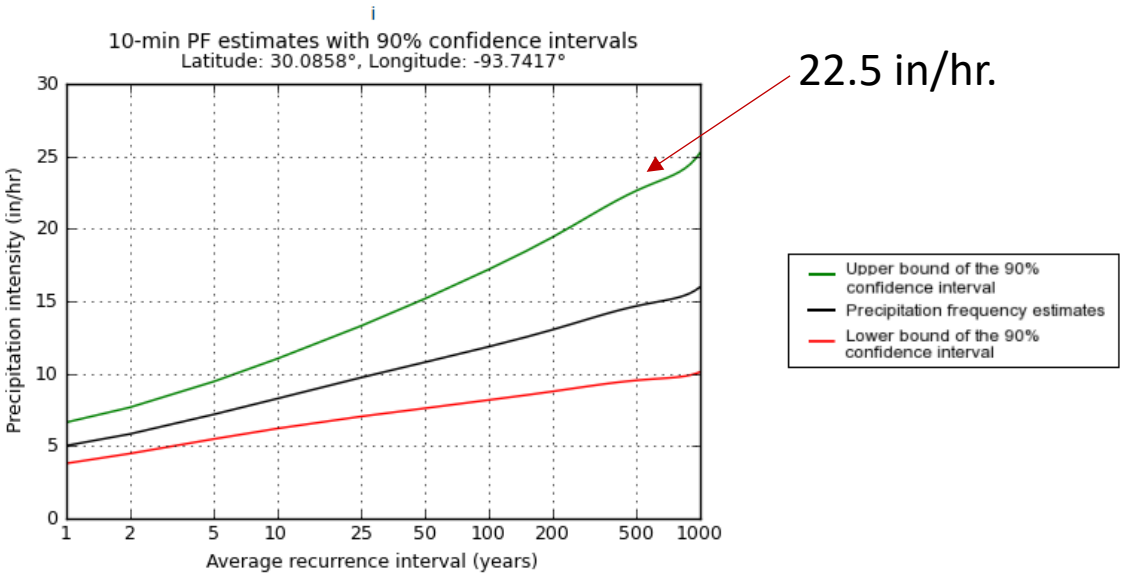


Figure 4.3: Statistical Maximum 10-min rainfall intensity for 500 yr. MRI

Therefore, based on field disdrometer measurements (from various sources such as NOAA, National Weather Service ATLAS project (NOAA ATLAS), National Centers for Environmental Information, Automated Surface Observing Systems (NCEI AWOS), Weather Flow, Texas Tech University Mesonet (NWI, TTU-MESONET)), and engineering judgment, it is hypothesized that a rain rate range of 20.3 cm/hr. (8 in/hr.) to 58.4 cm/hr. (23 in/hr.) should be used as a target for current full-scale simulation

Figure 4.4 shows both the models and their variation concerning rain rate. Although the models match well at lower rain rates, the difference increases with increasing rain rate values.

It was noted that:

(i) The largest drop size value was always higher for Willis and Tattelman (1989) model compared to Tokay et al. (2008) and

(ii) The highest concentration of raindrops typically occurs between 0.9 mm and 1.2 mm raindrop diameter irrespective of rain rates.

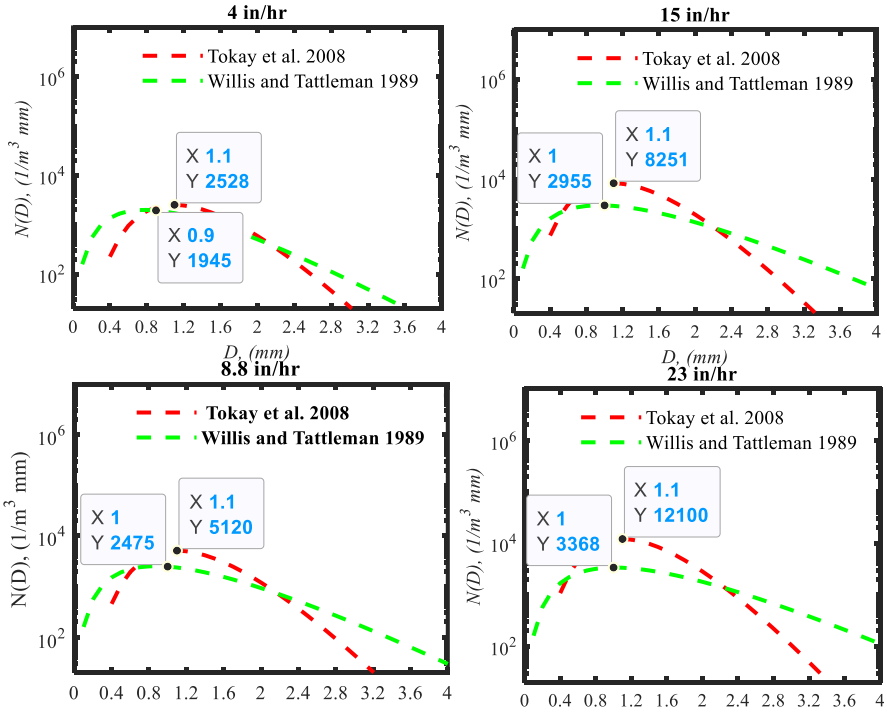


Figure 4.4: Gamma models comparison for different rain rates

To date, several researchers have contributed to the development of important WDR parameters and prediction models. These models can be briefly classified into three categories. i) Experimental/Field measurements, ii) Numerical/CFD, and iii) Empirical. Some rare experimental simulations/field measurements include Straube and Burnett (2000), who developed a semi-empirical model from the data accumulated from more than 1,000 rain events (each of 15-min duration) on a test house at the University of Waterloo. Blocken and Carmeliet (2005) described a novel setup for full-scale WDR measurements conducted on a model building instrumented at the Laboratory of Building Physics, Katholieke Universiteit Leuven, located in Flanders, Belgium. These results became a

preliminary database of WDR deposition values for buildings. Kubilay et al. (2014) presented full-scale WDR measurements collected on the façades of two different cubic structures situated within a 3 × 3 array of 2 m cubes. This experimental setup was in Dübendorf, Switzerland. Many researchers tried to mimic the behavior of water intrusion by modeling wind flow and raindrops using CFD. For example, Choi (1993), Choi (1994), Choi (1999) proposed a method to determine the WDR deposition on building facades through CFD modeling of the wind flow pattern and raindrop trajectories around a building. Straube and Burnett (1998) studied the WDR-induced wetting, water penetration, and drying patterns for common brick veneer wall cladding systems and compared their results against existing test procedures developed by the American Society for Testing and Materials (ASTM) and the American Architectural Manufacturers Association (AAMA). Hangan (1999) developed a CFD model to predict raindrop trajectories and wetting patterns for two building shapes, and he compared the modeling results against experimental datasets obtained from boundary layer wind tunnel (BLWT) testing. Blocken and Carmeliet (2004) compiled a comprehensive summary of WDR literature, examining available information across various disciplines; their paper discussed experimental measurements, semi-empirical modeling methods which combined theoretical calculations with field measurements, and numerical simulations for WDR measurements and predictions with an emphasis on building science applications. Later these CFD models paved the way for the development of semi-empirical models. Abuku et al., (2009), Blocken and Carmeliet (2010), Blocken et al. (2010); Blocken et al. (2011) compared the development and application of three different WDR models: a semi-empirical model developed by the International Standards Organization (ISO, 2009), the

semi-empirical model developed by Straube and Burnett (1998) and Straube and Burnett (2000), and the numerical CFD model first developed by Choi (1993), Choi (1994) and enhanced models by Blocken and Carmeliet (2002) and Blocken and Carmeliet (2007). These authors demonstrated the ability of CFD modeling to produce reliable WDR deposition results but acknowledged the cost and complexity of the CFD modeling as two major limitations to its widespread application; the authors recognized the importance of the semi-empirical methods, despite their limitations, and argued that CFD modeling may enhance the overall accuracy and adoption of the semi-empirical models. Foroushani et al. (2014) conducted CFD modeling to investigate the effect of roof overhangs on WDR deposition. The study found that the overhang's ability to protect the building façade was dependent on its size and on the oncoming wind parameters. Further, the presence of an overhang was able to protect the upper half of the building by reducing WDR deposition by as much as 80%, although the lower half of the building façade was generally unaffected by the presence of the overhang. Measured results were compared against predictions derived from two semi-empirical models, one of which underestimated the WDR and the other overestimated the average WDR. Abdelhady (2021) developed a framework to measure water ingress due to WDR (estimated by RANS-EMM framework) that combines the rain deposition on the building envelope with perforations due to damage caused by hurricane winds (based on a hurricane damage model including dynamic winds and windborne debris impact).

Due to the specific geographical locations of most experimental datasets, the available WDR depositions were not measured under extreme wind and rain conditions

associated with hurricanes. However, recent efforts have been made to characterize WDR parameters, such as raindrop size distribution (RSD) and rain rate, specifically during hurricanes, to better understand these extreme weather conditions. Tokay et al. (2008) reported fundamental rain parameters acquired by disdrometer field measurements during seven tropical cyclones during the 2004-2006 Atlantic hurricane seasons. These findings indicated relatively high concentrations of small and medium-sized raindrops during tropical cyclones, producing high values for the raindrop number concentration, the liquid water content, and the rain rate. Friedrich et al. (2013) reported RSD measurements gathered during Hurricane Ike in 2008 and during convective thunderstorm events in the Great Plains region of the United States during 2010; this research discussed inherent limitations of disdrometer measurements during high wind events and recommended the use of Parsival during high wind measurements to reduce certain measurement errors. Numerical modeling of WDR effects under extreme wind conditions had also been attempted. Van de Lindt and Dao (2009), Dao and van de Lindt (2012), van de Lindt and Dao (2012) combined CFD and finite element (FE) modeling to develop fragility curves for rainwater intrusion through a wood frame roof system applicable to residential construction. These results led to the development of a loss model for both structural and nonstructural damage in wood frame construction due to hurricanes, where the nonstructural losses were primarily attributed to rainwater intrusion.

Although full-scale measurements are necessary for validation of semi-empirical and numerical modeling of WDR effects, one major limitation of full-scale field measurements is the temporal dependence on natural wind and rain events to occur before

useful data may be acquired. One method for overcoming this limitation is the development of large/full-scale testing facilities capable of simulating accurate and repeatable wind and WDR conditions. At the University of Florida (UF), Salzano et al. (2010) conducted an extensive study of water penetration at the window-wall interface using common installation methods for residential wood framing and concrete masonry walls. In this study, the window systems were tested in an air chamber under static air pressure conditions and cyclic air pressure conditions, as well as under dynamic WDR conditions generated by the UF Hurricane Simulator; the pressure and time of leakage were reported, but water intrusion volumes were not measured. Van Straaten et al. (2010) explored the possibility of testing window assemblies under more accurate wind loading patterns when compared to the conventional test protocol of ASTM E331. To accomplish this, a pressure load actuator (PLA) system was installed over a full-scale window assembly. Pressure time histories obtained from BLWT testing were reproduced by the PLA system to simulate realistic time-varying wind loads on the window. At Florida International University (FIU), Bitsuamlak et al. (2009) assessed water intrusion through secondary water barriers on a roof system under simulated hurricane conditions using the six-fan Wall of Wind (WOW) facility. Chowdhury et al. (2011) conducted similar experiments with the 6-fan WOW system to investigate water intrusion volumes through commonly installed roof vent devices. Baheru (2014) reported their efforts to simulate hurricane-level wind and WDR conditions with the 12-fan WOW facility at FIU. Under these simulated conditions, Baheru et al. (2014b) conducted a detailed study of water deposition on the façade of a 1:4 scale residential building model to improve the risk assessment methodology in the FPHLM, and Vutukuru et al. (2020) conducted a study on

residential windows and studied the rain sheltering effect with the presence of shutter systems.

Considering the testing standards, water intrusion in High Velocity Hurricane Zones is only addressed in the TAS 202 standard. The TAS 202 test procedure requires an application of 75% Design Pressure (DP) in the positive and negative directions (windward pressure and suction) for 30 s each, and then this process is repeated at 150% DP for the same 30 s durations. After the window system passes the uniform static pressure testing, water is then applied to the door at a minimum rate of 5 gallons per hour (gph) per square foot, which correlates to a rain rate of approximately 8.8 in/hr. on the test specimen. The TAS protocol requires the rain simulation to occur with a minimum static air pressure of 15% DP applied across the operable window for at least 15 min. It is hypothesized that this procedure does not adequately determine an operable window's ability to resist water intrusion for two reasons: First, the water intrusion requirements are conducted at only 15% DP, a much lower DP than what the window may experience during hurricane-level WDR events under service conditions. Second, while the application of static air pressure is sufficient to determine the strength of the window assembly, it does not replicate the dynamic time-dependent pummeling effect of the wind and rain on the window system that would occur during an actual hurricane. Since the wind-induced inertial force is a primary driving force of water intrusion, the necessary dynamic interaction that may force water to flow through a potential envelope defect is lacking in the standard test protocols. This study tries to fill this knowledge gap by realistic dynamic-wind testing by

simultaneous exposure of operable windows to the wind field of WOW and simulated full-scale rain field.

### 4.3 Full-Scale RSD distribution at WOW

As explained in Sections 4.1 and 4.2, due to the interdependency of rain and wind, it was important to accurately simulate RSD in a wind tunnel that was capable of simulating wind-induced pressures accurately. This section explains the RSD achieved at the WOW experimental facility for different rain rates. The Willis and Tattelman, (1989) gamma model was used to compare the achieved rain field. Various nozzle types were tested by measuring rain characteristics using Precipitation Imaging Probe (PIP) placed at the center of the WOW turntable as shown in Figure 4.5. The results were then analyzed, and the nozzle types and configurations were modified based on the obtained results. More details on the procedure (for a 1:4 scaled RSD model) can be found in Baheru (2014). A similar procedure was utilized for obtaining the right number of nozzles in the current study. Table 4 shows the testing protocol followed for each trial configuration. The tests were performed at three wind speeds and three heights at the turntable center. High speed wind testing was performed at 29.06 m/s (65 mph), 44.7 m/s (100 mph), and 58.12 m/s (130 mph). The heights tested were 0.91 m. (3ft.), 1.83 m. (6ft.), and 2.73 m. (9 ft.) based on the height of the window and window location (1.83 m. being the center of the window on the specimen). A review of commercially available nozzles was performed to check the viability of existing nozzles such as Tee Jet classification shown in Table 5 and the largest available UC nozzles were tested without wind flow (and gravity-driven) using PIP in the staging area of WOW as shown in Figure 4.6 to measure maximum drop size.

Figure 4.5: PIP at 0.91m. (6ft.) height located at turntable center

Table 4: Full-scale WDR testing protocol

| Wind speed(m/s) at 1.83m. | Height(m.) | Wind direction ($^0$) | Test Duration (per angle, min) |
|---|---|---|---|
| 29.06 | 0.91,1.83,2.73 | 0 | 2 |
| 44.70 | 0.91,1.83,2.73 | 0 | 2 |
| 58.12 | 0.91,1.83,2.73 | 0 | 2 |

Table 5: Tee Jet agricultural nozzle configuration

| Category | Symbol | Diameter(mm) |
|---|---|---|
| Extremely fine | XF | 0.05 |
| Very fine | VF | < 0.136 |
| Fine | F | 0.136-0.177 |
| Medium | M | 0.177-0.218 |
| Coarse | C | 0.218-0.349 |
| Very Coarse | VC | 0.349-0.428 |
| Extremely coarse | XC | 0.428-0.622 |
| Ultra-coarse | UC | >0.622 |

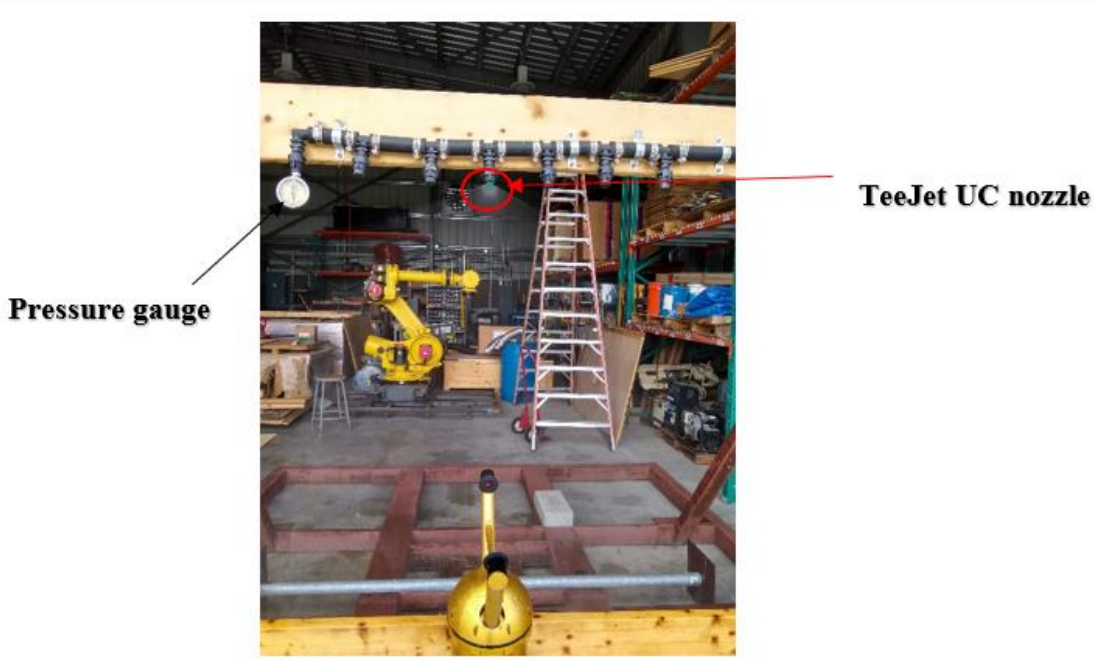


Figure 4.6: Flow free measurements of UC nozzle

However, the expected mean diameter was around 1 mm, and based on the tests performed in flow-free tests, the maximum diameter from PIP measurements was found to be 0.7 mm. and hence these nozzles were discarded. Later the option of 3-D printed nozzles was explored, and similar flow-free tests were performed using different nozzles with an opening diameter starting from 4 mm. and a conical shape to provide dispersion of water along the flow field. Based on these free flow tests and using basic Bernoulli's and continuity equations, the nozzle configuration shown in Figure 4.7 (this nozzle is henceforth referred to as K3-60) was chosen for the tests inside the WOW facility.

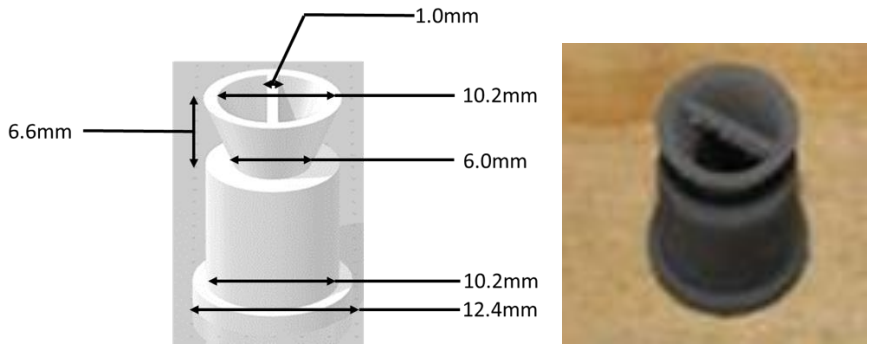


Figure 4.7: Figures showing nozzle dimensions and actual 3-D printed nozzle

The rain rate values were calculated by dividing the flow rate of water ($m^3$/hr) released from the nozzles, with an area of the flow management box (6.1 m x 4.27 m or 26.05 $m^2$) and then converted into in/hr from m/hr. Table 6Table *6* shows the flow rate values computed for the best of tested configurations, Tee Jet nozzles correspond to spray nozzles of type 8008E used in (Baheru et al., 2014a) and Figure 4.8 shows the best configurations out of sixteen tested configurations that are attached to three triangular spires at WOW. These flow rates are within the target range explained in Section 4.2, hence the RSD plots for these configurations are shown in Figure 4.9.

Table 6: Flow rates for the best of tested configurations

| Test No. (refer to Figure 4.8) | Nozzle configuration, per spire | Flow rate(gal/min) | Rain rate, in/hr. (cm/hr.) |
|---|---|---|---|
| 1 | 11 K3-60 | 63 | 22.3 (56.6) |
| 5 | 2 K3-60+9 Tee Jet | 49.5 | 17.5 (44.4) |
| 6 | 1 K3-60+10 Tee Jet | 42.5 | 15 (38.1) |
| 7 | 1 K3-60 | 24.5 | 8.8 (22.4) |
| 8 | 2 K3-60 (East, West) +11 Tee Jet (Center) | 26 | 9.3 (23.6) |

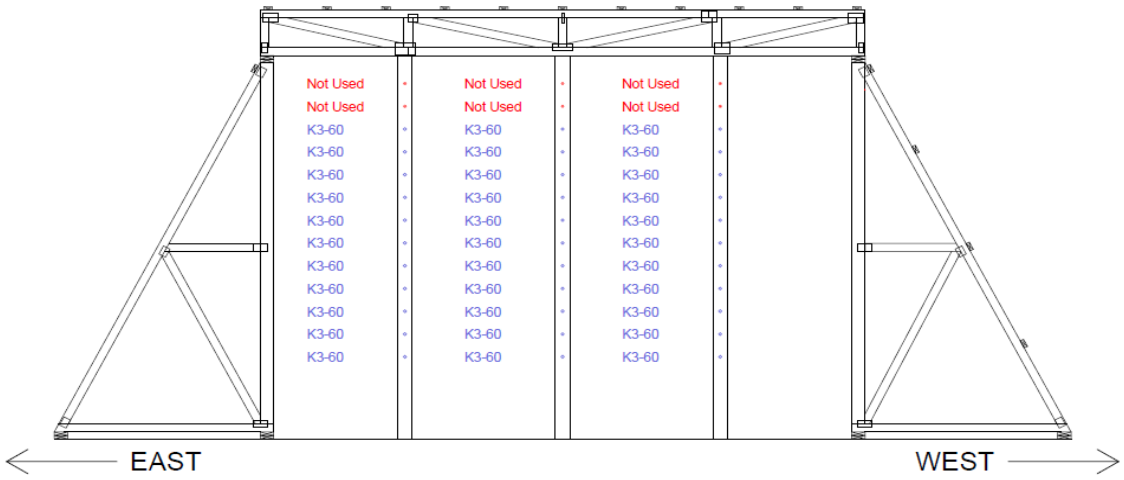


Figure 4.8 (a): Nozzle configuration to achieve Rain rate of 56.6 cm/hr.

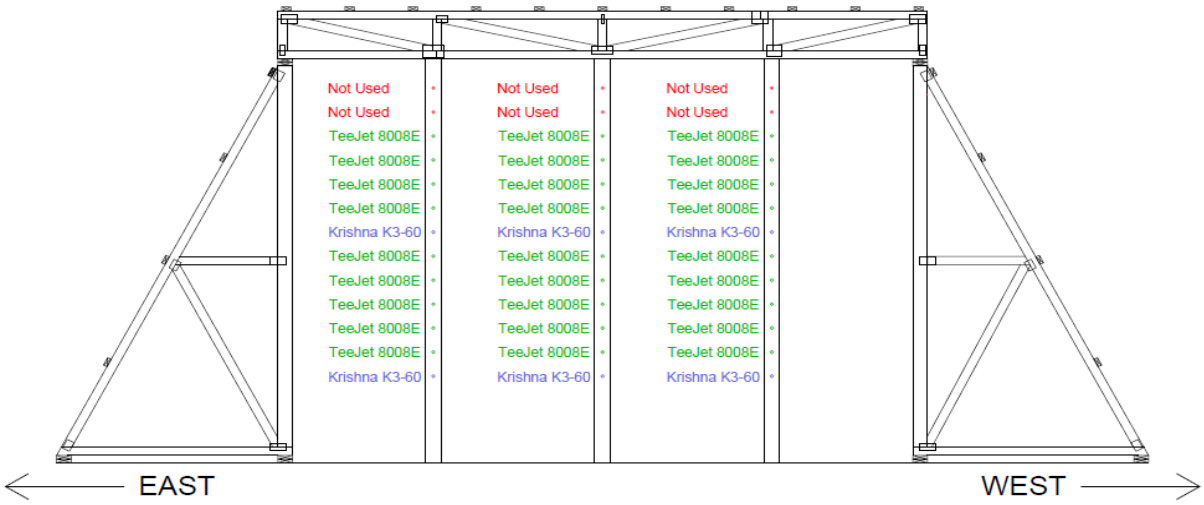


Figure 4.8 (b): Nozzle configuration to achieve Rain rate of 44.4 cm/hr

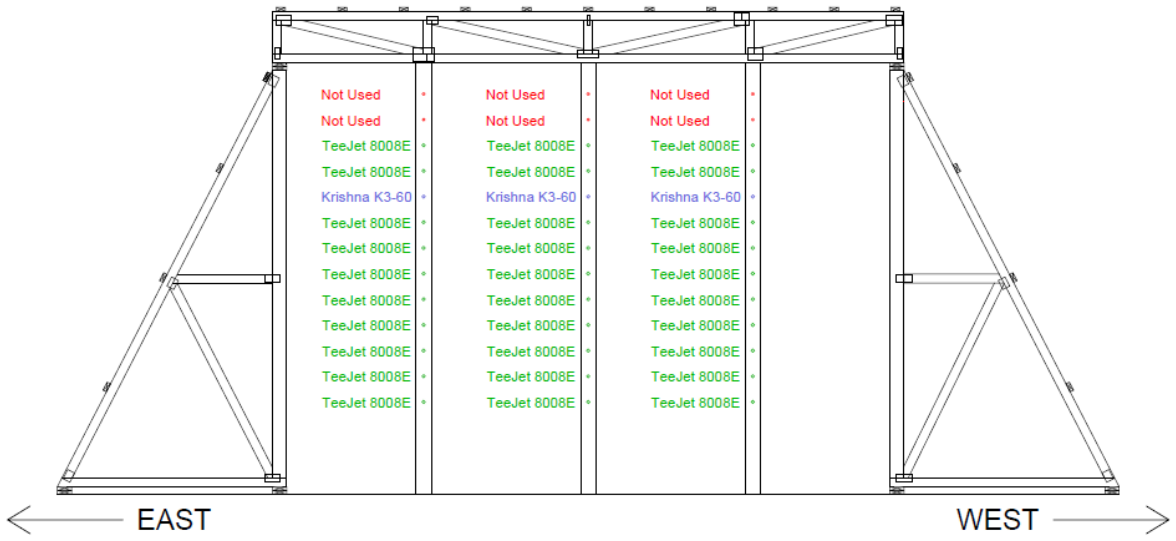


Figure 4.8 (c): Nozzle configuration to achieve Rain rate of 38.1 cm/hr

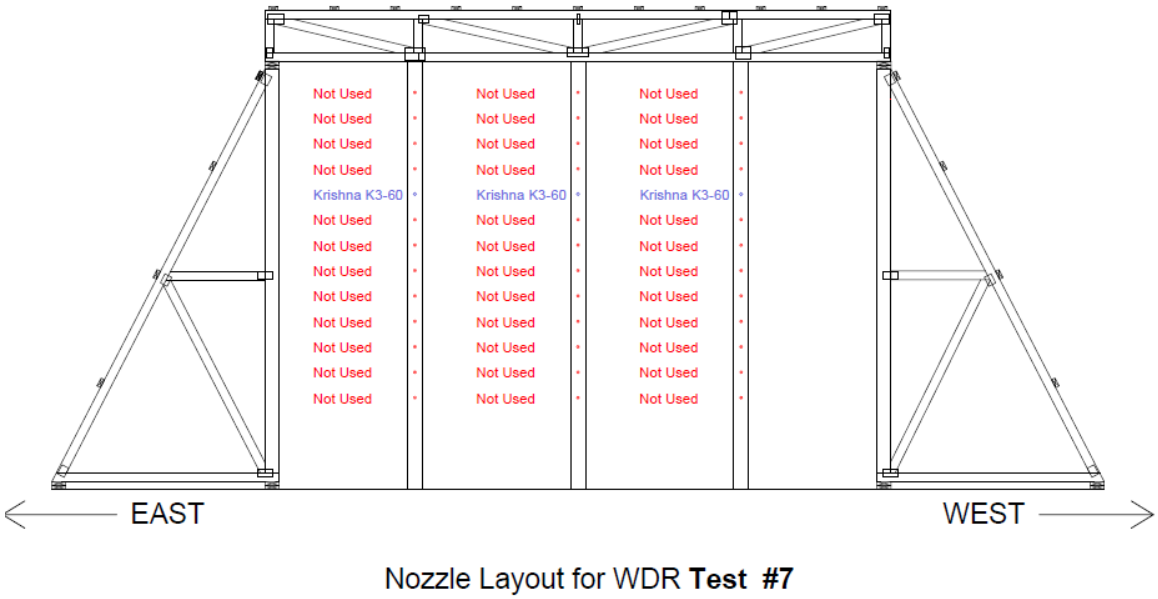


Figure 4.8 (d): Nozzle configuration to achieve Rain rate of 22.4 cm/hr

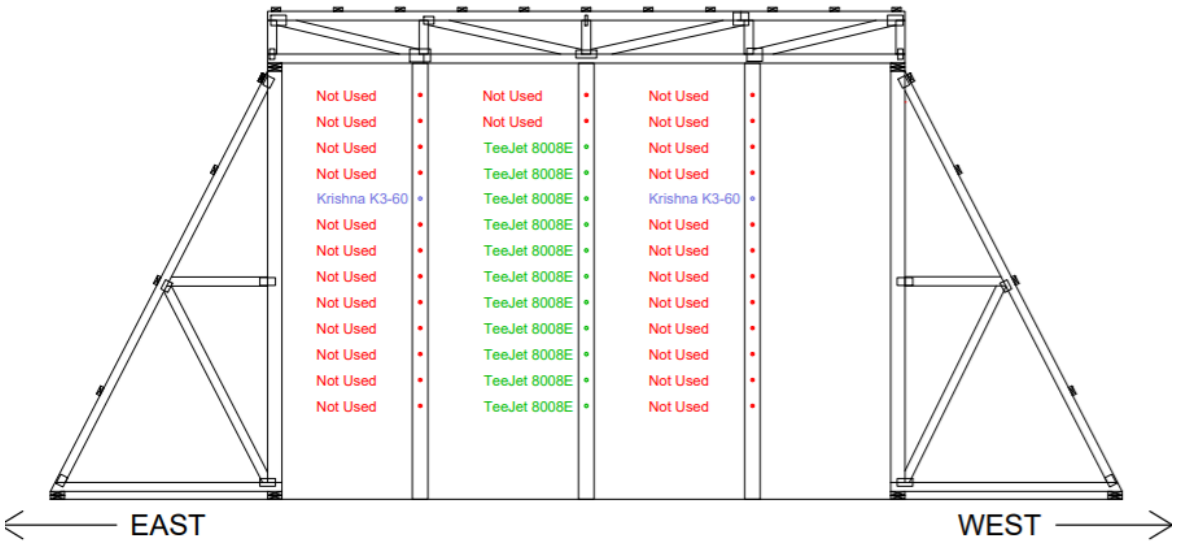


Nozzle layout for WDR **Test #8**

Figure 4.8 (e): Nozzle configuration to achieve Rain rate of 23.6 cm/hr

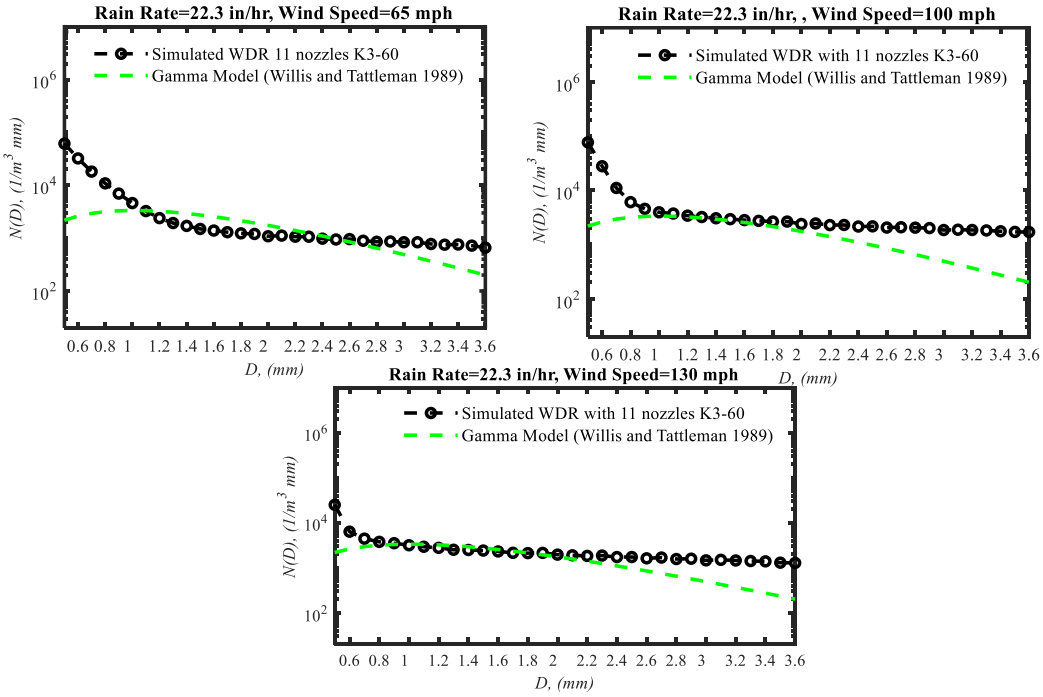


Figure 4.9 (a): RSD comparison at 1.83 m. (6ft.) height, test #1

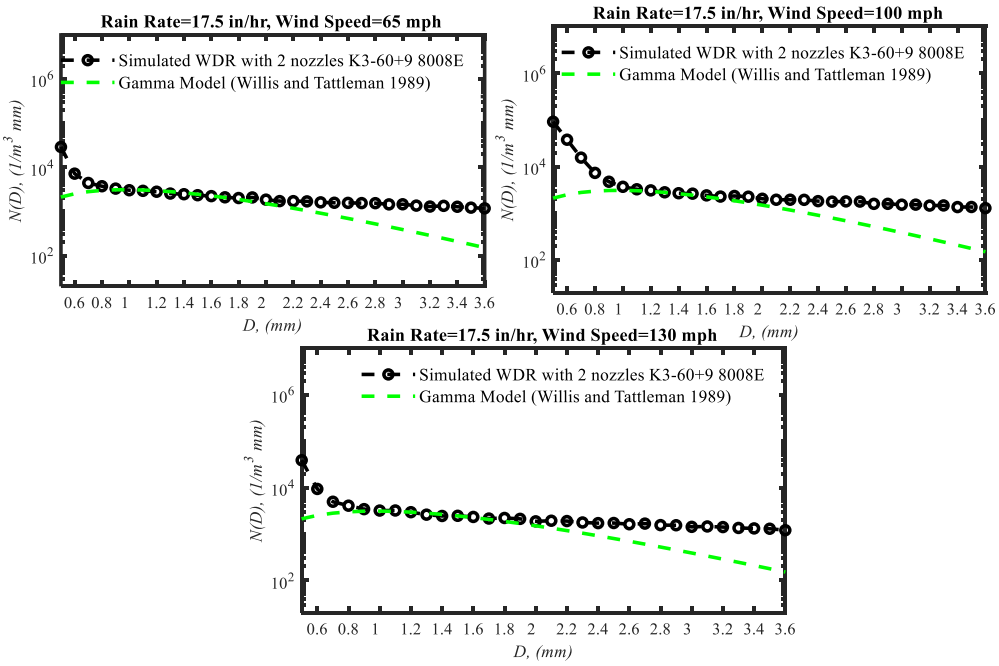


Figure 4.9 (b): RSD comparison at 1.83 m. (6ft.) height, test #5

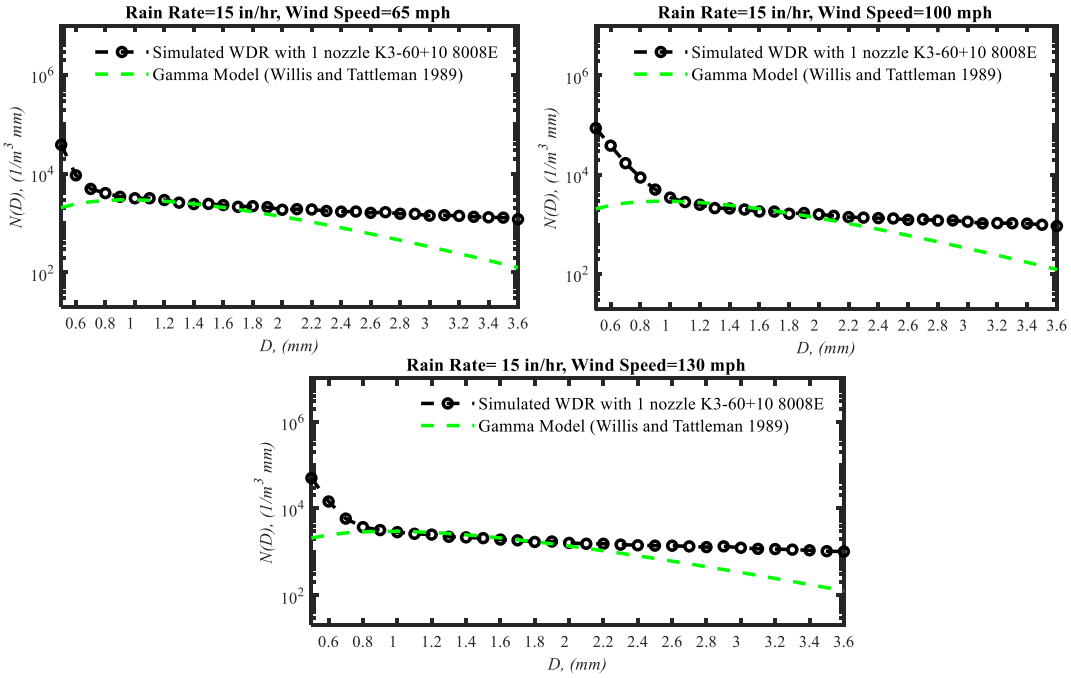


Figure 4.9 (c): RSD comparison at 1.83 m. (6ft.) height, test #6

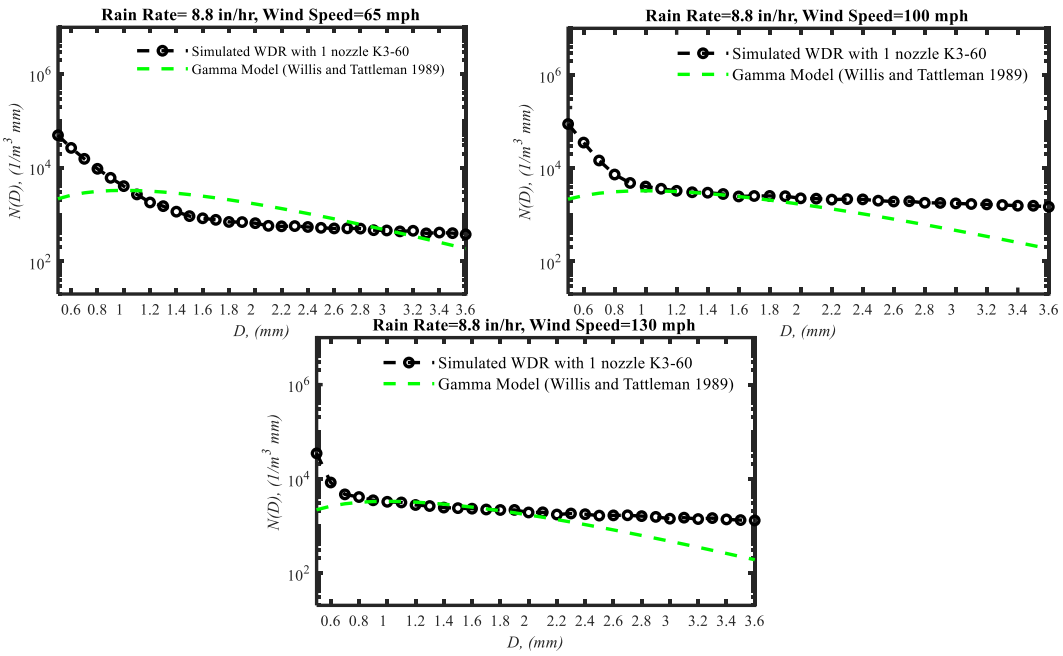


Figure 4.9 (d): RSD comparison at 1.83 m. (6ft.) height, test #7

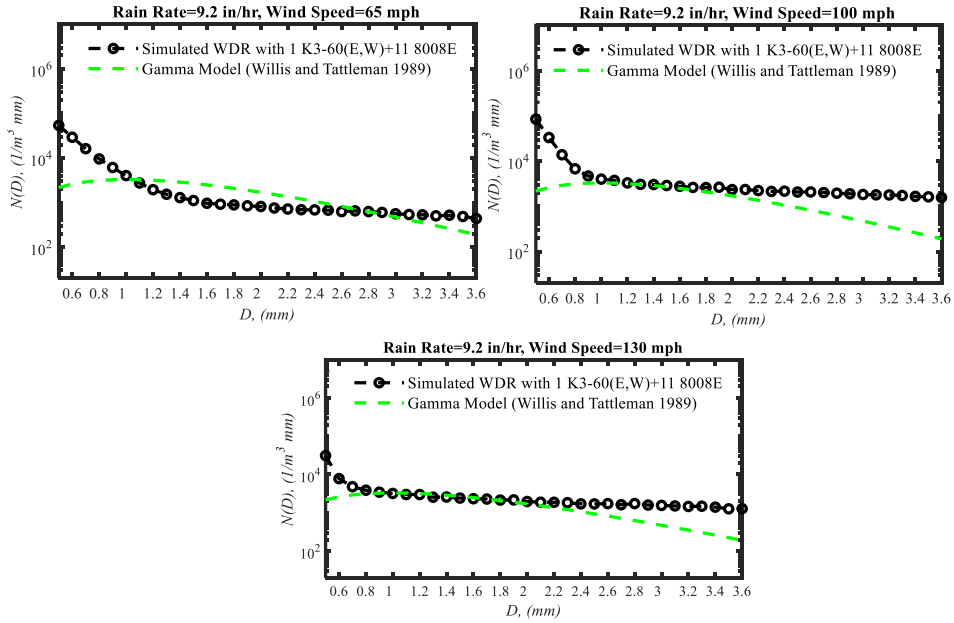


Figure 4.9 (e): RSD comparison at 1.83 m. (6ft.) height, test #8

Some general observations based on the simulation are:

- 3-D printed nozzles performed better than commercially available spray nozzles for full-scale rain simulation.
- Although the smaller and larger diameter raindrops (< 0.6 mm and > 3.2 mm, respectively) do not match closely with the gamma model, it was hypothesized that, for structural testing, accurate simulation of the highest concentration raindrops (typically of about 1mm) would be sufficient, as the larger raindrops typically get deposited at the lower part of the building as explained in Surry et al,1994 and Inculet 2001.
- The effect of the rain rate is more critical than wind velocity for nozzle selection.
- For a better comparison with testing and standards, test #7 achieved a rain rate of 8.8 in/hr. configuration was selected for the current operable window tests.

**4.4 Operable window WDR tests**

According to FEMA-490, 2005, Florida Building Code, buildings compliant with FBC 2001 were least affected by hurricanes. Most of the damage was limited to building envelopes, such as windows, doors, roof coverings, and soffits. The damage to these components led to rain intrusion into the building and caused damage to the contents. One of the major rain intrusion paths were the openings in walls caused by windows and between the window-wall interface. Current window design in North America includes four barriers for water penetration resistance, water-shedding surface, exterior moisture barrier, vapor barrier, and air barrier (Salzano et al. (2010)). Several studies showed the inadequacy of existing static, static-cyclic, and 15% DP codes and standards for water penetration (RDH Building Engineering Ltd. (2002), Lacasse et al., (2003), Salzano et al.,

(2010), Vutukuru et al. (2020)). Hence this section focuses on the results obtained from realistic dynamic testing of a product-approved operable window against simulated full-scale rain.

Typically, two types of collection systems were used in WOW for quantifying the amount of rainwater into the building, water collections buckets/devices (Baheru et al. (2014b), and Vutukuru et al. (2020) and absorbent material (Raji et al. (2020)). However, the presence of the absorbent material during the test changes the aerodynamics of the system, hence might yield inaccurate results. So, the current testing uses a hybrid rain collection device and absorbent material for the quantitative measurement of water seeping through the window. The collection device was used to measure most of the water and absorbent material was used to weigh the remaining small amount of water on the windowsill. To account for the building aerodynamics, absorbent material was used to collect water after the test was performed. Go Pro and High-Definition camera were installed inside the specimen to identify the location of water intrusion through the window and/or window-wall interface. Figure 4.10 shows the water collection system (assembled and installed components shown in Figure 2.19) with a tap to drain the water.

Figure 4.10: Installed plexiglass water collection system

The tests were performed at three wind speeds of 29.06 m/s (65 mph), 44.7 m/s (100 mph), and 58.12 m/s (130 mph) and three wind directions, $15^0$ and $345^0$, and $0^0$ (windward direction) as shown in Table 4.

Baheru et al. (2014b) expressed water intrusion at a given location on the building façade in terms of two nondimensional parameters: the rain admittance factor (RAF) to quantify water intrusion due to direct impinging raindrops, and the surface runoff coefficient (SRC) to quantify water intrusion due to surface runoff rainwater. RAF and SRC are calculated by Equations 7 and 8, respectively:

$$RAF = \frac{RR_{b,\mathrm{DI}}}{RR_v} \tag{7}$$

$$SRC = \frac{RR_{b,\mathrm{SR}}}{RR_v} \tag{8}$$

The term $RR_{b,\,DI}$ represents the rain rate at a given point on the building facade due to direct impinging raindrops, and the term $RR_{b,\,SR}$ represents the rain rate at a given point on the building facade due to the surface runoff rainwater. In both equations, the term

$RR_v$ is the free-stream wind-driven rain rate measured at a given reference height. Values of $RR_{b,\,DI\ and}$ $RR_{b,\,SR}$ are calculated by Equations 9 and 10, respectively:

$$RR_{b,DI} = \frac{V_{o,\mathrm{DI}}}{A_o t} \tag{9}$$

$$RR_{b,SR} = \frac{V_{o,\mathrm{SR}}}{A_{\mathrm{SR}} t} \tag{10}$$

where, $V_{o,\mathrm{DI}}$ is the volume of water that enters an opening due to direct impinging raindrops, $A_{\mathrm{DI}}$ is the area of the opening, $V_{o,\mathrm{SR}}$ is the volume of water that enters an opening due to surface runoff rainwater, and $A_{\mathrm{SR}}$ is the area of the building façade over which surface runoff rainwater may reach a given opening. For both equations, is the duration of the WDR event.

However, for window testing, Vutukuru et al. (2020) expressed the total volume of WDR intrusion through a given opening on a building envelope, $V_{tot}$, as the sum of the water intrusion volume due to direct impinging raindrops, $V_{DI}$, and the water intrusion volume due to surface runoff rainwater, $V_{SR}$, as shown in Equation 11 below:

$$V_{tot} = V_{DI} + V_{SR} \tag{11}$$

Rather than distinguishing the volume of water intrusion attributed to direct impinging raindrops versus the volume of water attributed to surface runoff, the current study focused on finding the total volume of water intrusion, $V_{tot}$ , accumulated from both mechanisms that impact the operable window simultaneously. For this reason, the observed water intrusion was reported as the total rain rate into the building through the

window as a function of the total volume of water intrusion, denoted here by $RR_{b,tot}$. Values of  were calculated according to Equation 12:

$$RR_{b,tot} = \frac{V_{tot}}{A_e t} \tag{12}$$

In Equation 12, the total volume, $V_{tot}$ , has the same meaning as defined in Equation 11, and represents the duration of the WDR event. The term was adopted here to represent the effective area of the window for both direct impinging raindrops and surface runoff.  The effective area was calculated as the area of the operable window (direct impinging raindrop region) plus the area of the wall directly above the window (surface runoff region) as shown in Figure 4.11.

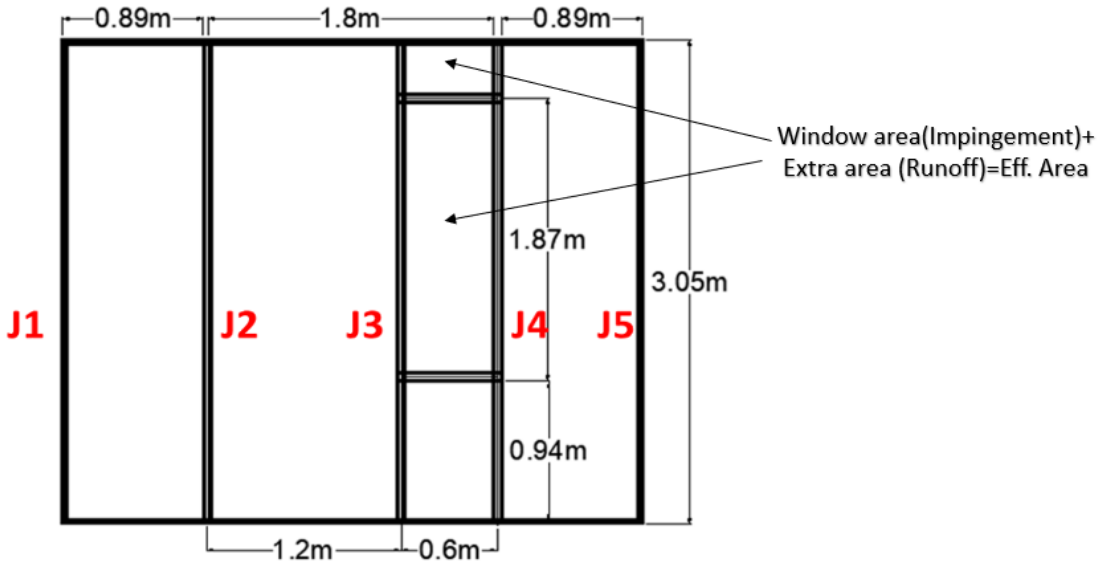


Figure 4.11: Effective Area for Surface Run-off and Direct Impingement

Figure 4.12 shows the calculated values plotted against %DP, calculated based on a design pressure value of 77.9 psf. calculated as per ASCE 7-16. The procedure to convert wind speed into %DP was explained in (Vutukuru et al., 2020). Based on the video recording during the test, it was observed that the primary source of water intrusion was at the window system-wall interface where the vulnerable point exists as shown in Figure 4.13.

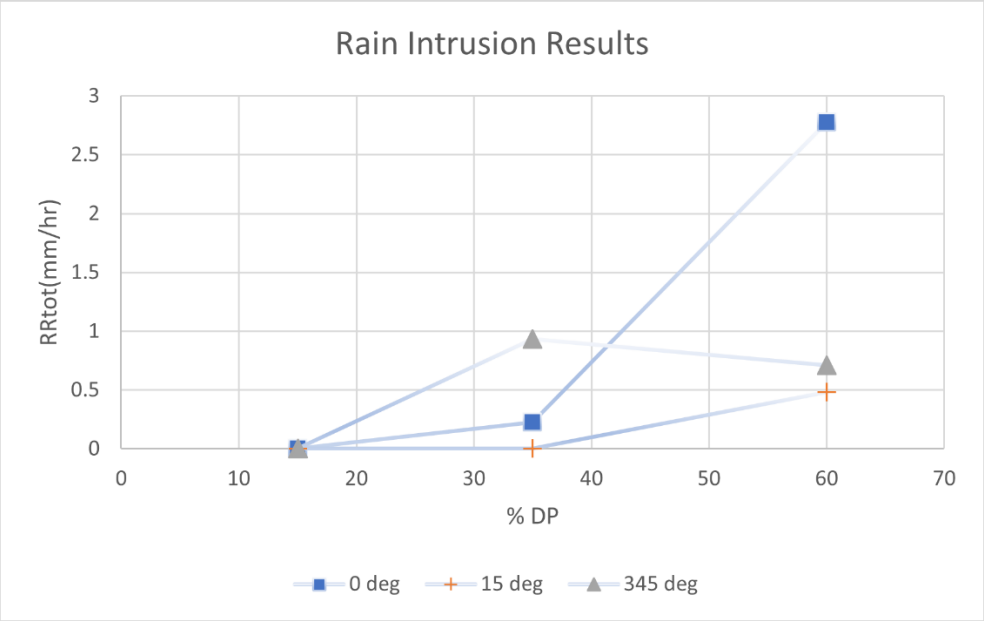


Figure 4.12: Total rain intrusion expressed as rain rate

Figure 4.13: Formation of water bubble and deposition of water on the windowsill at 100 mph

4.5 Chapter 4 references


Abdelhady, A. (2021). Resilience of Residential Wooden Structures against Wind Hazards (Doctoral dissertation), University of Michigan.

Abuku, M., Blocken, B., Roels, S., 2009. Moisture response of building facades to wind-driven rain: field measurements compared with numerical simulations. Journal of Wind Engineering and Industrial Aerodynamics 97, 197–207.

American Society of Civil Engineers. (2016). Minimum Design Loads for Buildings and Other Structures (ASCE/SEI 7-16). American Society of Civil Engineers.

American Architectural Manufacturer's Association, 101, North American Fenestration Standard/Specification (NAFS) for windows, doors, and skylights. AAMA.

Automated Surface/Weather Observing Systems | National Centers for Environmental Information (NCEI)URL https://www.ncei.noaa.gov/products/land-based-station/automatedsurface-weather-observing-systems

Baheru, T., 2014. Development of test-based wind-driven rain intrusion model for hurricane-induced building interior and contents damage.

Baheru, T., Chowdhury, A.G., Bitsuamlak, G., Masters, F.J., Tokay, A., 2014a. Simulation of wind-driven rain associated with tropical storms and hurricanes using the 12-fan Wall of Wind. Building and Environment 76, 18–29.

Baheru, T., Chowdhury, A.G., Pinelli, J.-P., Bitsuamlak, G., 2014b. Distribution of wind-driven rain deposition on low-rise buildings: Direct impinging raindrops versus surface runoff. Journal of Wind Engineering and Industrial Aerodynamics 133, 27–38. https://doi.org/10.1016/j.jweia.2014.06.023

Best, A.C., 1950. The size distribution of raindrops. Quarterly journal of the royal meteorological society 76, 16–36.

Bitsuamlak, G.T., Chowdhury, A.G., Sambare, D., 2009. Application of a full-scale testing facility for assessing wind-driven-rain intrusion. Building and Environment 44, 2430–2441.

Blocken, B., Abuku, M., Nore, K., Briggen, P.M., Schellen, H.L., Thue, J.V., Roels, S., Carmeliet, J., 2011.Intercomparison of wind-driven rain deposition models based on two case studies with full-scale measurements. Journal of Wind Engineering and Industrial Aerodynamics 99, 448–459.

Blocken, B., Carmeliet, J., 2010. Overview of three state-of-the-art wind-driven rain assessment models and comparison based on model theory. Building and Environment 45, 691–703.

Blocken, B., Carmeliet, J., 2007. On the errors associated with the use of hourly data in wind-driven rain calculations on building facades. Atmospheric Environment 41, 2335–2343. https://doi.org/10.1016/j.atmosenv.2006.11.014

Blocken, B., Carmeliet, J., 2005. High-resolution wind-driven rain measurements on a low-rise building experimental data for model development and model validation. Journal of Wind Engineering and Industrial Aerodynamics 93, 905–928.

Blocken, B., Carmeliet, J., 2004. A review of wind-driven rain research in building science. Journal of wind engineering and industrial aerodynamics 92, 1079–1130.

Blocken, B., Carmeliet, J., 2002. Spatial and temporal distribution of driving rain on a low-rise building. Wind and Structures 5, 441–462.

Blocken, B., Dezsö, G., van Beeck, J., Carmeliet, J., 2010. Comparison of calculation models for wind-driven rain deposition on building facades. Atmospheric environment 44, 1714–1725.

Blocken, B., Roels, S., Carmeliet, J., 2007. A combined CFD–HAM approach for wind-driven rain on building facades. Journal of Wind Engineering and Industrial Aerodynamics 95, 585–607. https://doi.org/10.1016/j.jweia.2006.12.001

Choi, E.C., 1999. Wind-driven rain on building faces and the driving-rain index. Journal of Wind Engineering and Industrial Aerodynamics 79, 105–122.

Choi, E.C., 1993. Simulation of wind-driven-rain around a building. Journal of Wind Engineering and Industrial Aerodynamics 46, 721–729.

Choi, E.C.C., 1994. Determination of wind-driven-rain intensity on building faces. Journal of Wind Engineering and Industrial Aerodynamics 51, 55–69.

Choi, E. C. C. 1999, Wind-driven rain on building faces and the driving-rain index. Journal of Wind Engineering and Industrial Aerodynamics, 79(1-2), pp.105-122.

Chowdhury, A.G., Bitsuamlak, G.T., Fu, T.-C., Kawade, P., 2011. Study on roof vents subjected to simulated hurricane effects. Natural Hazards Review 12, 158–165.

Dao, T.N., van de Lindt, J.W., 2012. Loss analysis for wood frame buildings during hurricanes. I: Structure and hazard modeling. Journal of Performance of Constructed Facilities 26, 729–738.

FEMA 488 – 2005. Mitigation Assessment Team Report Hurricane Charley in Florida Observations, Recommendations, and Technical Guidance | Building America Solution Center. URL https://basc.pnnl.gov/library/fema-488-mitigation-assessment-team-report-hurricane-charleyflorida- observations.

FEMA 490-2005. Summary Report on Building Performance-2004 Hurricane Season| Building America Solution Center.

FEMA 2018. Mitigation Assessment Team Report Hurricane Charley in Florida Observations, Recommendations, and Technical Guidance | Building America Solution Center.

Foroushani, S.S.M., Ge, H., Naylor, D., 2014. Effects of roof overhangs on wind-driven rain wetting of a low-rise cubic building: A numerical study. Journal of wind engineering and industrial aerodynamics125, 38–51.

Friedrich, K., Higgins, S., Masters, F.J., Lopez, C.R., 2013. Articulating and stationary PARSIVEL disdrometer measurements in conditions with strong winds and heavy rainfall. Journal of Atmospheric and Oceanic Technology 30, 2063–2080.

Hangan, H., 1999. Wind-driven rain studies. A C-FD-E approach. Journal of Wind Engineering and Industrial Aerodynamics 81, 323–331.

International Code Council, Inc. (2017). Testing Application Standard (TAS) 202-94 Criteria for Testing Impact and Nonimpact Resistant Building Envelope Components Using Uniform Static Air Pressure. 2017 Florida Building Code—Test Protocols for High Velocity Hurricane Zone, 978-1-60983-688-7.

Inculet, DR. (2001). The Design of Cladding against Wind Driven Rain (Doctoral dissertation), University of Western Ontario, Canada.

ISO, E., 2009. Hygrothermal performance of buildings–calculation and presentation of climatic data–Part 3: calculation of a driving rain index for vertical surfaces from hourly wind and rain data. BS EN ISO 15927–3.

Kelkar, V.N., 1961. Size Distribution of Raindrops. Nature 192, 252–252. https://doi.org/10.1038/192252a0

Kijewski-Correa, T.L., Roueche, D.B., Mosalam, K.M., Prevatt, D.O., Robertson, I.N., 2021. StEER: A Community-centered Approach to Assessing the Performance of the Built Environment after Natural Hazard Events. Frontiers in Built Environment 7.

Kubilay, A., Derome, D., Blocken, B., Carmeliet, J., 2014. High-resolution field measurements of wind driven rain on an array of low-rise cubic buildings. Building and environment 78, 1–13.

Lacasse, M.A., O'Connor, T., Nunes, S., Beaulieu, P., 2003. Report from Task 6 of MEWS project: Experimental assessment of water penetration and entry into wood-frame wall specimens-final report.

Research Rep. No. IRC-RR-133, 2003. Institute for Research in Construction, National Research Council Canada, ⟨ http://irc. nrc-cnrc. gc. ca/fulltext/rrl33/⟩.

Robinson, G., Baker, M.C., 1975. Wind driven rain and buildings. Conseil national de recherches du Canada.

Lonfat, M., Marks Jr, F.D., Chen, S.S., 2004. Precipitation distribution in tropical cyclones using the Tropical Rainfall Measuring Mission (TRMM) Microwave Imager: A global perspective. Monthly Weather Review 132, 1645–1660.

Lopez, C.R., 2011. Measurement, analysis, and simulation of wind driven rain. University of Florida.

Marshall, J. S., & Palmer, W. M. (1948). The Distribution of Raindrops with Size. J. Meteorol, 5(165166), 1520-0469.

Merceret, F.J., 1974. On the size distribution of raindrops in Hurricane Ginger. Monthly Weather Review 102, 714–716.

Pinelli, J.-P., Roueche, D., Kijewski-Correa, T., Plaz, F., Prevatt, D., Zisis, I., Elawady, A., Haan, F., Pei, S., Gurley, K., 2018. Overview of damage observed in regional construction during the passage of Hurricane Irma over the State of Florida, in: Forensic Engineering 2018: Forging Forensic Frontiers.

Raji, F., Zisis, I., Pinelli, J.P., 2020. Experimental Investigation of Wind-Driven Rain Propagation in a Building Interior. Journal of Structural Engineering 146, 04020114. https://doi.org/10.1061/(ASCE)ST.1943-541X.0002670

Rasmussen, E.N., Straka, J.M., Davies-Jones, R., Doswell III, C.A., Carr, F.H., Eilts, M.D., MacGorman, D.R., 1994. Verification of the origins of rotation in tornadoes experiment: VORTEX. Bulletin of the American Meteorological Society 75, 995–1006.

Salzano, C. T., Masters, F. J., & Katsaros, J. D. (2010). Water penetration resistance of residential window installation options for hurricane-prone areas. Building and Environment, 45(6), 1373-1388.

Straube, J.F., Burnett, E.F., 1998. Driving rain and masonry veneer, in: Water Leakage through Building Facades. ASTM International.

Straube, J.F., Burnett, E.F.P., 2000. Simplified prediction of driving rain on buildings, in: Proceedings of the International Building Physics Conference. Eindhoven University of Technology Eindhoven, the Netherlands, pp. 375–382.

Subramanian, D., Salazar, J., Duenas-Osorio, L., Stein, R., 2014. Building and validating geographically refined hurricane wind risk models for residential structures. Natural Hazards Review 15, 04014002.

Tokay, A., Bashor, P.G., Habib, E., Kasparis, T., 2008. Raindrop size distribution measurements in tropical cyclones. Monthly Weather Review 136, 1669–1685.

van de Lindt, J.W., Dao, T.N., 2009. Performance-based wind engineering for wood-frame buildings. Journal of Structural Engineering 135, 169–177.

van de Lindt, J.W., Nguyen Dao, T., 2012. Loss analysis for wood frame buildings during hurricanes. II: Loss estimation. Journal of performance of constructed facilities 26, 739–747.

Van Straaten, R.A., Kopp, G.A., Straube, J.F., 2010. Testing water penetration resistance of window systems exposed to “realistic” dynamic air pressures, in: Proceedings of International Conference of Building Envelope Systems and Technology (ICBEST), Vancouver.

Vutukuru, K.S., Moravej, M., Elawady, A., Chowdhury, A.G., 2020. Holistic testing to determine quantitative wind-driven rain intrusion for shuttered and impact resistant windows. Journal of Wind Engineering and Industrial Aerodynamics 206, 104359.

WeatherFlow Tempest Weather System and Professional Services. WeatherFlow. URL https://weatherflow.com.

West Texas Mesonet | National Wind Institute | TTU. URL https://www.depts.ttu.edu/nwi/research/facilities/wtm/.

Willis, P.T., Tattelman, P., 1989. Drop-size distributions associated with intense rainfall. Journal of Applied Meteorology and Climatology 28, 3–15.

Wise, A.F.E., Sexton, D.E., Lillywhite, M.S.T., 1965. Studies of air flow round buildings. Building research station watford (England).

# 5. CONCLUSIONS AND FUTURE WORK

## 5.1 Conclusions

This dissertation, through full-scale experimental testing, explains the vulnerability of operable window systems to dynamic-wind flow fluctuations. The knowledge gap in the existing test protocols and standards concerning structural dynamics due to wind-induced vibration and wind-driven rain was identified. To study the behavior of operable window systems, a full-scale experimental study (with sensors) was performed at the WOW facility, by subjecting the specimen to realistic extreme wind speeds. The dynamic amplification in the open condition of the window was primarily observed in the hardware component connecting the window frame and it yielded during destructive testing. Also, during high wind speed testing, a dynamic amplification was observed on the glass itself. DAF values were provided in this dissertation for incorporation into the existing static design to incorporate the flow fluctuation effects and an analytical model was developed based on the theory of Mechanical Admittance to include a resonant component contribution to the response.

The product-approved window was also subjected to the simulated, realistic full-scale wind-driven rain with simultaneous high wind speeds to quantify the amount of water entering through the window. These results were utilized to understand the inadequacy of tests and standards for product approval of windows. The dissertation identified the critical component and its failure mode due to the wind-induced vibration in open and closed conditions, which was not considered in the static classical experiments and design codes.

The following conclusions summarize the main findings of this study:

- The natural frequencies and total damping range (structural and aerodynamic) of the window are 12.5 Hz and 3.5 to 3.6% respectively.
- From a pressure perspective, codes seem to be conservative based on the Cp values obtained at WOW.
- ASCE 7-16's criteria of less than 1Hz for dynamic design consideration of flexible structures does not apply to building components such as windows, curtainwalls, etc., and dynamic Amplification was seen due to the frequency match between oncoming wind and windows natural frequency.
- An analytical model was developed and validated based on the frequency domain analysis using Mechanical Admittance Function. This model could be used to predict failure at higher wind speeds.
- An approach to calculate Gust Effect Factor was proposed based on ASCE 7-16 dynamically sensitive structure approach and a decent match between experimental and proposed method was obtained.
- A reasonable full-scale rain size distribution for structural testing purposes was achieved by a combination of 3-D printed and agricultural spray nozzle configurations. Several successful trial results were shown for different rain rates, and the window was tested with the configuration having a rain rate of 8.8 in/hr. as per standards.

- Full-scale WDR tests on the operable window show the inadequacy of 15% design pressure criteria for rain intrusion and the window-wall interface was found out as the most vulnerable hotspot for the start of the water bubble formation.
- Windowsill proved to be a savior for water tightness by stopping the majority of the water from entering the building, although, for longer durations of testing, water still entered the building.
- For the open window case, although a higher wind speed (~130 mph) was resisted by the window, the failure was attributed to hardware hinge (connecting the window to the frame) yielding. This failure was observed in many high-rise buildings' windows failures/during extreme events.

**5.2 Recommendations for future study**

Efficient hardware to resist the fatigue from wind-induced vibration needs to be designed and re-tested to achieve a resilient window design. Future testing with Particle Image Velocimetry (PIV) is recommended to better understand the water deposition and complex wind-water interaction on the window surface. Full structure FE model with stabilization diagram would help to better understand the stable and unstable frequencies. A parametric study by FEM for higher wind speeds, (than experimentally tested) is suggested to be compared with the results obtained from the analytical model. Correlation study between wind speed and rain rate using Copula function for joint probability distribution based on field measurements of wind speed and rainfall data during hurricanes for multi-variate dependent structures is recommended for future study. For example, in

case of a gumbel fit, variate can be expressed as $-\ln\left[((-\ln(u))^{\propto} + (-\ln(R))^{\propto}\right]^{1/\propto}$, where u and R correspond to wind speed and rain rate respectively.

# VITA

KRISHNA SAI VUTUKURU

| | |
|---|---|
| 2012-2016 | B. Tech (Bachelor of Technology)., Civil Engineering, Indian Institute of Technology, BHU, Varanasi India |
| 2016-2017 | M.Tech (Master of Technology)., Structural Engineering, Indian Institute of Technology, BHU, Varanasi India |
| 2020 | M.S (Master of Science)., Civil Engineering, Florida International University, Florida |
| 2017-2021 | Ph.D. (Doctor of Philosophy), Civil Engineering Florida International University, Florida |

PUBLICATIONS

Azzi, Z., Habte, F., *Vutukuru, K. S.***,** Chowdhury, A. G., and Moravej, M., "Effects of Roof Geometric Details on Aerodynamic Performance of Standing Seam Metal Roofs", Engineering Structures, Elsevier, Vol. 225, December 2020.

*Vutukuru, K. S.*, Moravej, M., Elawady, A., and Chowdhury, A.G., "Holistic Testing to Determine Quantitative Wind Driven Rain Intrusion for Shuttered and Impact Resistant Windows", Journal of Wind Engineering and Industrial Aerodynamics, Elsevier, Vol. 206, November 2020.

Feng, C., Chowdhury, A. G., Elawady, A., Chen, D., Azzi, Z., and *Vutukuru, K.S.*, "Experimental Assessment of Wind Loads on Roof to Wall Connections for Residential Buildings", Wind Engineering and Science, Frontiers in Built Environment, February 2020.

Mittal, R.K., and *Vutukuru, K.S.*, "Analysis and Retrofitting of Arch Bridges- A Review," International Journal of Bridge Engineering (IJBE), Vol. 5, No. 2, (2017), pp. 113-138.

Mittal, R.K., *Vutukuru, K.S.***,** and Maiti, P.R., "Effect of Mass of Moving Load on Dynamic Response of a Simply Supported Railway Bridge," i-manager's Journal on Structural Engineering, Vol. 5, No. 4, December2016-February 2017.

Alawode, K., *Vutukuru, K. S.*, Elawady, A., Lee, S.J., Chowdhury, A.G., and Lori, G., "Wind Induced Vibration and Wind-Driven Rain Performance of a Full-Scale Single Skin Facade Unit with Vertical Protrusions", ASCE Journal of Architectural Engineering (submitted).

Alawode, K., *Vutukuru, K. S.*, Elawady, A., and Chowdhury, A.G., "A state of the art review of wind loading on the roof to wall connections" (submitted).

Alawode, K., *Vutukuru, K.S.*, Elawady, A., Lee, S.J., Chowdhury A.G., and Lori, G., "Dynamic Properties and Weather Tightness of Double Skin Curtain walls", Proceedings of Structures Congress, Atlanta, Georgia, 2022. (conference paper)

*Vutukuru, K. S.*, Alawode, K., Bakhtiari, A., Elawady, A., Lee, S.J., Gan Chowdhury A.G., and Lori, G., "Full Scale Testing to Determine Wind Induced Vibrations on Curtain wall Systems", Proceedings of 11th Structural Engineering and Construction Conference, July 2021, Cairo, Egypt. (conference paper)

Alawode, K., *Vutukuru, K.S.*, Elawady, A., Chowdhury A.G., and Lori, G., "Full Scale Wind Testing to Determine the Role of Vertical Protrusions on Curtainwall Performance", Proceedings of 6th American Association of Wind Engineering (6 AAWE) Workshop (online), May 2021, Clemson University, Clemson, SC, USA. (conference paper)

Verma, V., *Vutukuru, K. S.*, Bian, L., Rojali, A., Ozecik, D., and Leon, A., "Reliability and Robustness Evaluation of a Remotely Operated Siphon System during Hurricanes", Proceedings of World Environment and Water Resources Congress, May 2020, Henderson, Nevada. (conference paper)

*Vutukuru, K.S.*, Moravej, M and Chowdhury, A. G., "Wind-Driven Rain Intrusion reduction for Shuttered Windows", Proceedings of the 15th International Conference on Wind Engineering Beijing, China, September 1-6, 2019. (conference paper)

Mejia, A., Viot, A., *Vutukuru, K.S.*, Elawady, A., and Chowdhury, A. G., "Experimental Testing and Numerical Analysis to validate a Full-Scale Downburst Simulator at the FIU Wall of Wind", Proceedings of the 5th American Association for Wind Engineering Workshop (5AAWE), Miami, Florida, August 2018. (conference paper)

Chowdhury, A. G., *Vutukuru, K. S.*, and Moravej, M., "Full and Large-Scale Experimentation Using the Wall of Wind to Mitigate Wind Loading and Rain Impacts on Buildings and Infrastructure Systems." Proceedings of Structural Engineering Convention, Jadavpur University, India, December 2018. (conference paper)

*Vutukuru, K.S.*, Hembram, B., and Mandal, S., "Response of Buildings with Different Plan Shapes Subjected to Static Wind Load," Proceedings of 8th National Conference on Wind Engineering, IIT-BHU, Varanasi, December 2016. (conference paper)

Mejia, A., *Vutukuru, K.S.*, Elawady, A., Chowdhury A.G., and Irwin, P., "Downburst Simulations at the NHERI Wall of Wind Experimental Facility," the 15$^{th}$ International Conference on Wind Engineering, Beijing, China, September 2019. (conference poster)